Microstructure and Mechanical Property of Heavily Deformed Al-Sc Alloy Having Different Starting Microstructures

2011

Ehsan Borhani

Department of Materials Science and Engineering

Graduate School of Engineering,

Group of Physical Property of Materials
Laboratory of Structure and Property of Materials

Kyoto University, Japan

Microstructure and Mechanical Property of Heavily Deformed Al-Sc Alloy Having Different Starting Microstructures

Ehsan Borhani

PhD. Thesis

Table of Contents

Chapter 1

Chapter 2

Chapter 3

Chapter 4

Chapter 5

Chapter 1

Background and Purpose

1.1. Purpose of the study

The purpose of the present study is to clarify the changes in microstructure, texture and mechanical property of an Al-Sc binary alloy during severe plastic deformation and subsequent annealing processes. Grain refinement of metallic materials has been an important subject in research and development of metals and alloys, but the minimum mean grain size that can be achieved in bulky metallic materials has been around 10 μm. On the other hand, development of severe plastic deformation (SPD) processes [1] that can apply a quite large plastic strain (above 4~5 in logarithmic equivalent strain) has made it possible to fabricate ultrafine grained (UFG) bulky metallic materials of which mean grain size is much smaller than 1 μm [2-5]. Based on this technological progress, fundamental studies on UFG materials have been energetically carried out since early 1990's, and a number of new and sometimes surprising findings about interesting structures and properties of UFG metals have been acquired [2-7].

The previous studies on UFG materials fabricated by SPD, however, have mostly used pure metals. The interaction between UFG structures and phase transformation including precipitation would be an interesting and unknown subject in this field. When the materials have pre-existing precipitates before the SPD process, it would affect the evolution of UFG structures and the change in mechanical properties during the process. They can be compared with the microstructures and mechanical properties of the materials without precipitates. For this purpose, several starting microstructures for the identical aluminum alloy, i.e., the specimens involving pre-existing precipitates with different particle sizes and the as-solution-treated specimens, are prepared and then provided to a SPD process in this study. The Al-Sc alloy, of which characteristics are described in the following section, is selected as the material studied in this thesis. Al-Sc alloys are known to give nanometer sized Al_3Sc precipitates in its matrix [8]. The Al_3Sc precipitates are very stable at high temperature, so that they strongly inhibit grain coarsening of the matrix. In the present study, the microstructure evolution during SPD of the Al-0.2wt%Sc alloy having three different starting microstructures is firstly investigated, together with the change in mechanical properties and texture evolution. Then the SPD processed Al-Sc alloy is subjected to the heat treatment that can act as annealing process involving recovery, recrystallization and grain growth and also as aging process resulting in precipitation. The fundamentals of the interaction between precipitates and restoration processes (recovery, recrystallization and grain growth) will be summarized in the later section in this chapter.

As a SPD process, accumulative roll bonding (ARB) is used in this study. The ARB process is a SPD process developed by Saito *et al.* [5] in 1998, and is the only SPD process that can be applied to continuous production of bulky sheet materials. The fundamentals of the ARB process will be also shown in the following section in this chapter. The study on ARB of Al-Sc alloy having the different starting microstructures described above has not yet been done before. The results of this study are expected to give new findings in the field of UFG metallic materials fabricated by SPD processes, and to throw light on a future direction of alloy design in such new class materials.

1.2. Al-Sc alloy

Al-Sc alloys have recently aroused lots of interest because of their various advantages. The alloys have superior corrosion resistance and weld-ability, and they are strong, light weight and very stable in grain structures at elevated temperatures. Furthermore Al-Sc alloys can be used for superplastic forming operations [9-10]. However, the price of Al-Sc alloys is still too high for most commercial applications, so that industrial use of this alloy is limited to a few aerospace applications and sport equipments, e.g. baseball bats [11]. In 1971, Willey [12] patented the first Al-Sc alloy. He found that adding scandium to aluminum alloys significantly improved their mechanical properties (**Fig. 1.1**). As shown in papers by Lathabai *et al*. [13] and Watanabe *et al*. [14], scandium, when added to aluminum, reduces hot cracking during welding and gives large increase in strength. Sc is also a powerful dispersoid strengthener, grain refiner and recrystallisation inhibitor in Al. It is also reported that compared with other grain refining elements used in aluminum alloys, Sc has the maximum solubility as shown in **Table 1**.

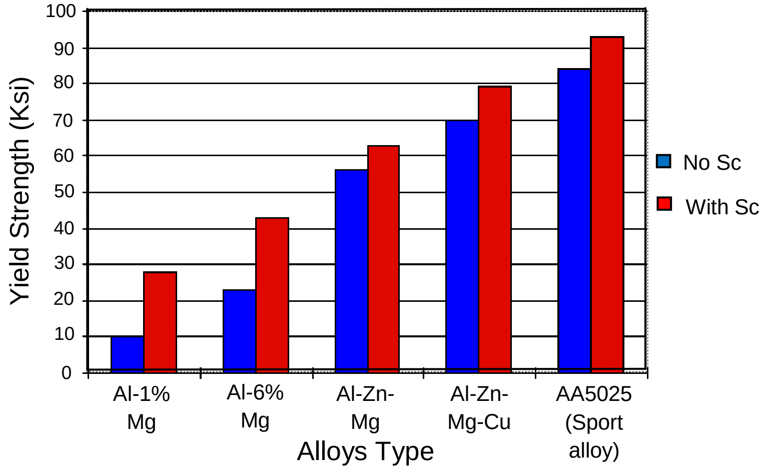

Fig. 1.1. Increase of strength by adding Sc to Al alloys [15].

Table 1.1. Solubility of Sc and other elements in Al [15].

Alloying elements	Solubility (weight %)	Solubility (atomic %)
Sc	0.38	0.33
Ti	0.18	0.05
Zr	0.15	0.08
Mn	0.3	0.15
Cr	0.25	0.13
V	0.1	0.05

The first assessed version of the Al-Sc phase diagram was presented by Gschneidner and Calderwood [16]. More recently, on the basis of new experimental data by Kononenko *et al.* [17] and thermodynamic considerations, Okamoto [18] proposed a new version of the phase diagram of Al-Sc. The latest complete Al-Sc phase diagram by Okamoto [18] is shown in **Fig. 1.2**. In this system four intermetallic compounds exist: Al_3Sc, Al_2Sc, AlSc and $AlSc_2$, all having narrow single phase ranges. It is established that Al_3Sc is formed by the eutectic reaction, L↔ α (Al) + Al_3Sc at 660 °C. As can be seen in the aluminum rich end of the phase diagram shown in **Fig. 1.3**, the maximum solubility of scandium in aluminum is approximately 0.38 wt.% [17-20].

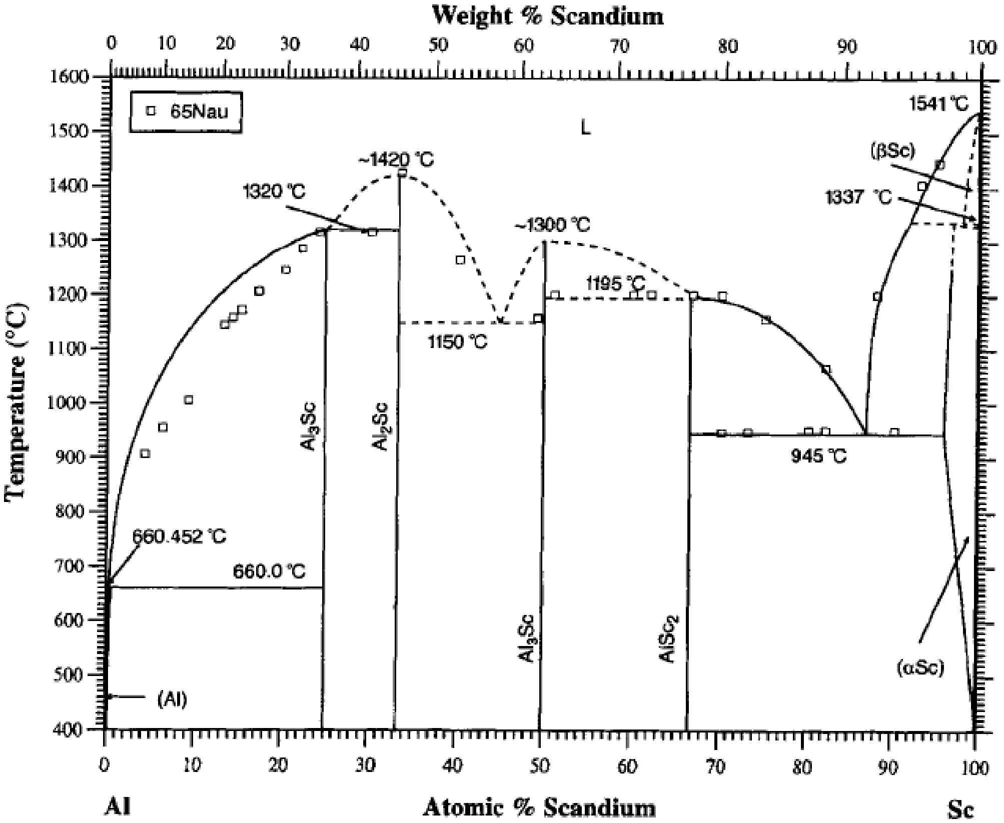

Fig. 1.2. Al-Sc phase diagram [18].

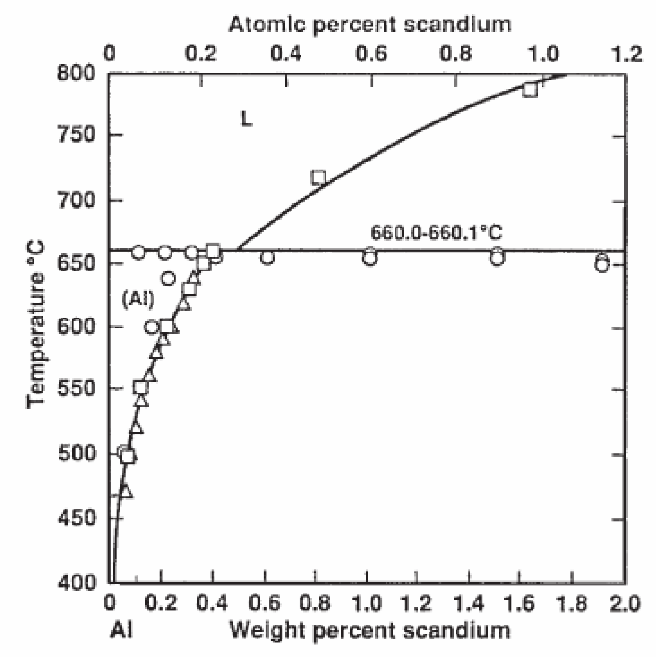

Fig. 1.3 Aluminum-rich end of the Al-Sc phase diagram [18, 21-22].

Al_3Sc can also precipitate from a supersaturated solid solution. Till now there is no evidence that any metastable phases form before precipitation of Al_3Sc. Thus it is assumed that the equilibrium phase nucleates directly from the supersaturated solid solution [23-29]. Al_3Sc has the $L1_2$-type ordered face-centered cubic structure. The atomic arrangement of the Al_3Sc phase is shown in **Fig. 1.4**. The lattice parameter of the Al_3Sc phase, 0.410 nm [30], matches very closely to that of the aluminum matrix, 0.405 nm.

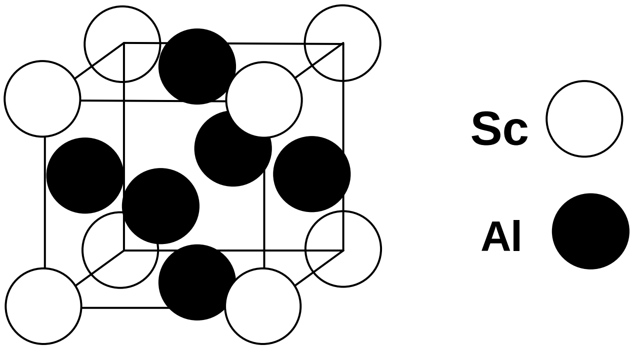

Fig. 1.4. Atomic arrangement of Al_3Sc phase [11].

The Al_3Sc particles have the high resistance for coarsening which keep them finely dispersed even at high temperatures. The thermally stable Al_3Sc particles accordingly have a strong effect of inhibiting grain growth of the matrix through pinning migrating grain boundaries, so that they increase recrystallization temperature and improve microstructure stability of the alloy [31-32].

1.3. Ultrafine-grained (UFG) or nano-structured material

In recent decades, a new class of metallic materials having mean grain size much smaller than 1 μm has been developed [2-7]. This kind of materials is so-called ultrafine-grained (UFG) or nano-structured materials. The UFG materials are realized by severe plastic deformation (SPD) processes that can apply huge plastic strains to the materials [1]. **Figure 1.5** illustrates the volume fraction of grain boundary as a function of mean grain size. Here the thickness of the grain boundary region is assumed to be 1 nm. The volume fraction of grain boundaries in the coarse-grained material with mean grain size larger than 10 µm is expected to be almost 0%. This indicates that most of the conventional metallic materials are "rare of grain boundaries". In contrast, the volume fraction of grain boundaries greatly increases when the grain size becomes smaller than 1 µm (ultrafine).

From another point of view, it is well known that mechanical properties of materials can be improved by grain refinement. So far, however, the minimum grain size of bulky conventional metallic materials that could be achieved is about 10 μm. It is, therefore, expected that UFG materials or nano-structured materials exhibit superior mechanical properties. Valiev [33] pointed out that some UFG or nano-structured materials can manage both high strength and large ductility, though high strength and large ductility are in trade-off relationship in conventional materials. The UFG or nano-structured materials also exhibit peculiar properties that have never been seen in conventional metallic materials having coarse-grained structures. Tsuji *et al.* [34] reported that yield-drop phenomena with Lüders band deformation appeared during tensile test in pure Al when the grain size is smaller than 2 μm. Huang *et al.* [35] reported a peculiar phenomenon of bulk nano-structured Al and Fe, that is, "hardening by annealing and softening by deformation". In general, metallic materials are hardened by deformation and are softened by annealing. Nano-structured Al and Fe fabricated by SPD process, however, can exhibit completely opposite behaviors, i.e., hardened by annealing and softened by deformation. The unique properties of the UFG materials prompted material scientists to study them in more detail, in both fundamental and application issues, under the demands for lightweight or high strength materials [36- 38].

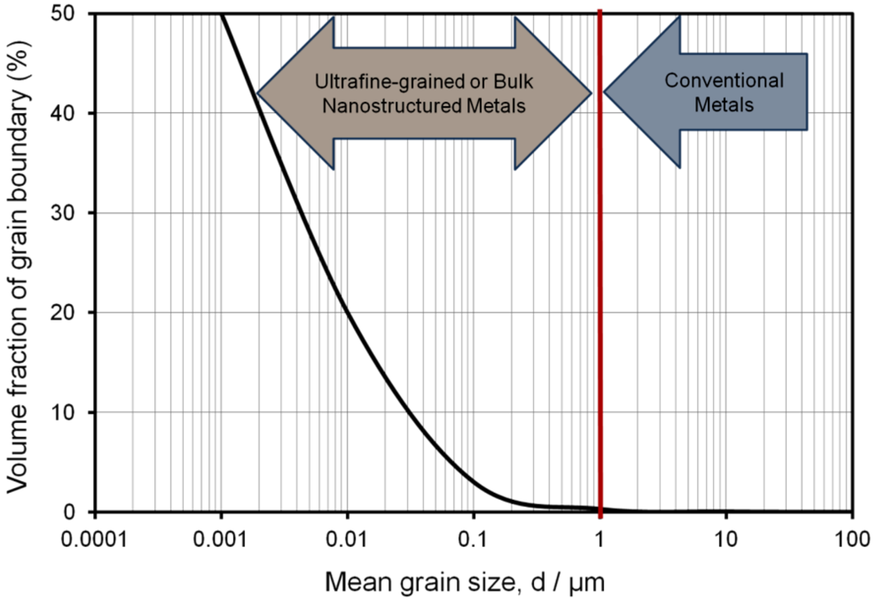

Fig. 1.5. The volume fraction of grain boundary as a function of mean grain size [36].

1.4. Accumulative roll bonding (ARB) process

SPD can fabricate bulk UFG metals having grain sizes much smaller than 1 μm. Several techniques of SPD have been developed to fabricate UFG materials, such as torsion under high pressure (HPT) [39-40], accumulative roll bonding (ARB) [41-44], and equal-channel angular pressing (ECAP) [45-47]. Among these techniques, the ARB process is used to fabricate UFG materials in the present study. The ARB process has some unique features. Firstly, unlike the ECAP and HPT processes which require special forming machines with large capacity and special dies, the ARB process can be performed by a conventional rolling mill. Secondly, in comparison to the other methods, the productivity of the ARB process is relatively high. The ARB is still the only SPD process that can be applied to continuous production of bulky sheet materials.

The ARB process was invented by Saito *et al.* [5] in 1998. The principle of the ARB is schematically shown in **Fig. 1.6.** The ARB process is a SPD process using rolling deformation. Rolling is the most advantageous metal working process for continuous production of plates, sheets and bars. However, the total reduction applied to the materials is substantially limited in conventional rolling because of the decrease in the thickness of the materials with increasing the reduction. In the ARB process, 50% rolled sheet is cut into two, stacked to be the initial dimension after degreasing and wire brushing the contact surfaces, and then rolled again. In order to obtain one-body solid materials, the rolling in the ARB process is not only a deformation process but also a bonding process (roll-bonding). To achieve good bonding, the roll-bonding process is sometimes carried out at elevated temperatures below recrystallization temperature of the material. The ARB process can apply significant amount of plastic strain into the materials, because the above mentioned procedures can be repeated limitlessly. The von Mises equivalent strain (ε_{eq}) after n cycles of the ARB can be expressed as:

$$\varepsilon_{eq} = -\frac{2n}{\sqrt{3}} \ln \frac{t}{t_0} = -\frac{2n}{\sqrt{3}} \ln(1-r) \tag{1.1}$$

where t_0, t, and r are initial thickness of the stacked sheets, the thickness after roll-bonding, and the reduction in thickness per cycle, respectively [41-42].

Sheets of various kinds of metallic materials, such as Al, Cu alloys and steels, have been processed by ARB process to develop UFG structures [42-44]. The most characteristic feature of the UFGs in the ARB processed materials is the elongated morphology. The microstructure reveals the lamellar boundary structure in heavily deformed materials elongating along the rolling direction (RD). The elongated UFG are the grains surrounded by high angle grain boundaries (HAGBs) having dislocation substructures inside the grains. The formation process of the UFGs during ARB (SPD) is characterized by ultrafine grain subdivision [48], recovery inside the UFGs, and short range grain boundary migration [1].

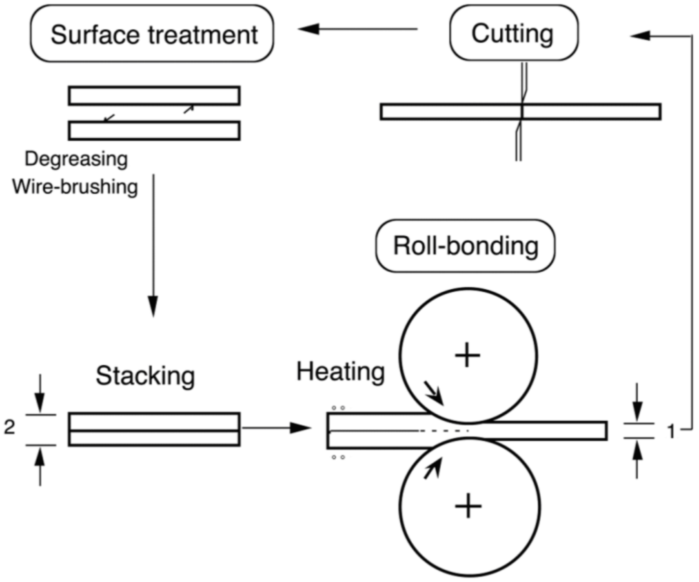

Fig. 1.6. Schematic illustration showing the principle of the ARB process [7].

1.5. Effect of precipitation on microstructure evolution during plastic deformation and subsequent annealing

It is well-accepted now that the UFG structures develop in single-phase alloys deformed to high strain levels by SPD processes. However, the presence of second-phase particles could potentially have a significant effect on formation of UFG structures during SPD process. For example, it is expected that precipitates can increase the rate of dislocation generation and large local misorientation gradients. This can lead to an increased rate in the formation of HAGBs, so that ultrafine grains may be obtained at considerably lower strain than in precipitates-free alloys. At the same time, the second-phase particles can be effective in dislocation pinning [49-53]. Therefore, the finer structure is expected in materials containing pre-existing precipitates compared to those in precipitates-free materials.

In the subsequent annealing of the deformed materials at elevated temperatures, the ultrafine structures fabricated by SPD are extremely unstable. Therefore, it is expected that the grain size is drastically increases due to migration of grain boundaries and then the benefits obtained by microstructural refinement are removed. The stability of the UFG structures can be achieved using second-phase particles that can impede grain coarsening during annealing by the process of grain boundary pinning (Zener pinning) [54-55] and keep the fine microstructures up to high temperatures. The recrystallization and grain coarsening are retarded in the materials containing second-phase particles compared to those in particles-free materials. The effect of the particles (or precipitates) on grain boundary is schematically shown in **Fig. 1.7.** The changes in microstructure, texture and mechanical properties of the ARB processed Al-Sc alloy during annealing are also studied in the present thesis.

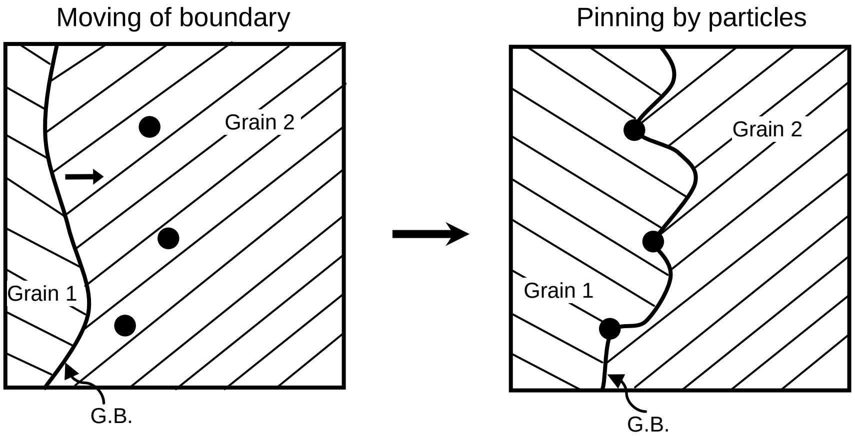

Fig. 1.7. Schematic illustration showing pinning effect of pre-existing precipitates on grain boundary migration.

1.5. Structure of this thesis

This thesis studies the effect of pre-existing precipitates on microstructures, mechanical properties and texture evolution in an Al-Sc alloy during ARB process and subsequent annealing. The thesis consists of 6 chapters.

Chapter 1 presents the purpose of this study and some fundamental background. The actual experimental results of the thesis are shown in Chapters 2-5.

Chapter 2 investigates the effect of small and large pre-existing precipitates on microstructural evolution of Al-0.2wt.%Sc alloy during the ARB process. The microstructure evolution in the solution-treated Al-0.2Sc alloy without Al_3Sc is also studied.

Chapter 3 demonstrates the mechanical properties of the Al-0.2Sc alloy having different starting microstructures during ARB and discusses the strengthening mechanisms based on the microstructural parameters obtained in Chapter 2.

Chapter 4 contains annealing behaviors of solution treated or pre-aged specimens which are deformed by the ARB process. The effect of pre-existing precipitates on annealing behavior is investigated.

Chapter 5 explains the texture evolution in the solution treated or pre-aged specimens of the Al-0.2Sc alloy during SPD by ARB and also during subsequent annealing. The effect of pre-existing precipitates on texture evolution is particularly discussed.

Conclusion of all chapters is summarized in **Chapter 6**.

References

[1] N. Tsuji, Y. Saito, Y. Minamino, Advanced Engineering Materials 5 (2003) 5.
[2] J. Richert, M. Richert, Aluminium 62 (1986) 604.
[3] R. Z. Valiev, N. A. Krasilnikov, N. K. Tsenev, Materials Science and Engineering A 137 (1991) 35.
[4] Z. Horita, D.J. Smith, M. Furukawa, N. Nemoto, R.Z. Valiev, T.G. Langdon, Materials Research 11 (1996) 1880.
[5] Y. Saito, N. Tsuji, H. Utsunomiya, T. Sakai, R. G. Hong, Scripta Materialia 39 (1998) 1221.
[6] N. Nemoto, Z. Horita, M. Furukawa, T.G. Langdon, Metall Materials 4 (1998) 1181.
[7] Y. Saito, N. Tsuji, H. Utsunomiya, T. Sakai, Acta Materialia 47 (1999) 579.
[8] B. K. Min, H.W. Kim, S.B. Kang, Materials Processing Technology 162–163 (2005) 355.
[9] S. Dobatkin, E. Bastarache, G. Sakai, T. Fujita, Z. Horita, T. Langdon, Materials Science and Engineering A 408 (2005) 141.
[10] F. Musin, R. Kaibyshev, Y. Motohashi, G. Itoh, Scripta Materialia 50 (2004) 511.
[11] J. Røyset and N. Ryum, International Materials Reviews 50 (1) (2005).
[12] L. A. Willey, Aluminum Scandium Alloy, USA patent no. 3619181.
[13] S. Lathabai, P. G. Lloyd, Acta Materialia 50 (2002) 4275.
[14] C. Watanabe, T. Kondo, and R. Monzen, Metallurgical and Materials Transactions A 35 (2004) 3003.
[15] Applications of Scandium in Al-Sc Alloys, http://www.scandium.org/Sc-Al.html.
[16] J. R. Gschneidner, F. W. Calderwood, Bull of Alloy Phase Diagrams 10 (1989) 34.
[17] V. I. Kononenko, S. V. Golubev, Izv Akad Nauk SSSR Metalls (1990) 197, translated in Russian Metals (1990) 193.
[18] H. Okamoto, J. Phase Equilibrium 12 (1991) 612.
[19] O. P. Naumkin, V.T. Terekhova and E.M. Savitskii, Russian Metals 4 (1965) 128.
[20] H. Ho Jo, S. Fujikawa, Materials Science and Engineering A 171 (1993) 151.
[21] M. E. Drits, E. S. Kadaner, T. V. Dobatkina and N. I. Turkina, Russian Metals 4 (1973) 152.
[22] S. Fujikawa, M. Sugaya, H. Takei and K. Hirano, J. Less-Common Metals 63 (1979) 87.
[23] R.W. Hyland, Metallurgical and Materials Transactions A 23 (1992) 1947.
[24] C. L. Roher, M. D. Asta, S. M. Foiles and R. W. Hyland, Material Research Society Symposium Proceedings 398 (1996) 477.
[25] C. Tan, Z. Zheng and B. Wang, Proceedings of 3rd International conference on 'Al alloys' 1 (1992) 290.
[26] M. J. Jones and F. J. Humphreys, Acta Materialia 51 (2003) 2149.
[27] M. Nakayama, A. Furuta and Y. Miura, Material Transactions, Japan Institute of Metals 38 (1997) 852.
[28] G.M. Novotny and A.J. Ardell, Materials Science and Engineering A 318 (2001) 144.
[29] J.D. Robson, M.J. Jones and P.B. Prangnell, Acta Materialia 51 (2003) 1453.
[30] Y. Harada, D. C. Dunand, Scripta Materialia 48 (2003) 219.
[31] E. A. Marquis and D. N. Seidman, Acta Materialia 49 (2001) 1909.
[32] G. M. Novotny, A. J. Ardell, Materials Science and Engineering A 318 (2001) 144.
[33] R. Z. Valiev, Nature Materials 3 (2004) 511.
[34] N. Tsuji, Y. Ito, Y. Saito, Y. Minamino, Scripta Materialia 47 (2002) 893.
[35] X. Huang, N. Hansen, N. Tsuji, Science 312 (2006) 249.
[36] J. S. Lee, J. S. Chun, Materials Science 16 (1981) 1557.

[37] J. Z. Lu *et al.*, Acta Materialia 58 (2010) 5354.
[38] X. Huang, N. Kamikawa, N. Hansen, Materials Science and Engineering A 483 (2008) 102.
[39] R. Z. Valiev, R. K. Islamgaliev and I.V. Alexandrov, Progress Materials Science 45 (2000) 103.
[40] R. Z. Valiev, R. S. Mishra, J. Grosa, A.k. Mukherjee, Scripta Materialia 34 (1995) 1443.
[41] Y. Saito, H. Utsunomiya, N. Tsuji and T. Sakai, Acta Materialia 47 (1999) 579.
[42] Sung H. Whang, Nanostructured Metals and Alloys, Woodhead Publishing Limited, 2011.
[43] S. H. Lee, Y. Saito, T. Sakai and H. Utsunomiya, Materials Science and Engineering A, 325 (2002) 228.
[44] J.A. del Valle, M. T. Pérez-Prado, O. A. Ruano, Materials Science and Engineering A, 410-411 (2005) 353.
[45] V. M. Segal, Materials Science and Engineering A 271 (1999) 322.
[46] Y. Iwahashi, Z. Horita, M. Nemoto and T.G. Langdon, Acta Materialia, 46 (1998) 3317.
[47] M. Furukawa, Y. Iwahashi, Z. Horita, M. Nemoto, N. K. Tsenev, R.Z. Valiev, T. G. Longdon, Acta Materialia, 45 (1997) 4751.
[48] N. Hansen, J. Materials Science and Technology 17 (2001) 409.
[49] F. J. Humphreys, M. G. Ardakani, Acta Metallurgica 42 (1994) 749.
[50] F. J. Humphrey, Acta Metallurgical 27 (1979) 1801.
[51] H. Jazeri, F. J. Humphreys, In: G. Gottstein, D. Molodov, Editors. 5th International Conference on Recrystallization and Related Annealing Phenomena, Belgium: Achen (2001) 549.
[52] P. J. Apps, J. R. Bowen, P. B. Prangnell, In: M. Zehetbauer, R. Z. Valiev, Editors. Nanomaterials by Severe Plastic Deformation-NANSPD2, Vienna Austria (2002) 138.
[53] P. J. Apps, J. R. Bowen, P. B. Prangnell, Acta Materialia 51 (2003) 2811.
[54] M. Drury, J. L. Urai, Tectonophysics, 112 (1990) 235.
[55] P.R. Rios, F. Siciliano, H. R. Zschommler Sandim, R. L. Plaut, A. F. Padilha, Materials Research 8 (2005).

Chapter 2

Microstructural Evolution during ARB Process of Al-0.2wt%Sc Alloy Having Different Starting Microstructures

Abstract

Effect of pre-existing precipitates on microstructure evolution during severe plastic deformation was studied. An Al-0.2wt.%Sc alloy was firstly solution-treated (ST) at 630°C and then aged at 300°C or 400°C for having different sizes of Al_3Sc precipitates. The mean diameter of Al_3Sc precipitates was 3.62 nm and 50 nm for 300°C and 400°C aging, respectively. In the as-aged specimens, Al_3Sc had coherency with the Al matrix. Three kinds of specimens, that were solution-treated (ST), aged at 300°C and aged at 400°C, were then heavily deformed by the accumulative roll bonding (ARB) process up to 10-cycle (corresponding to an equivalent strain of 8.0) at room temperature. After 10 cycles of the ARB process, the specimens showed a lamellar boundary structure having the mean lamellar interval of 0.37 μm, 0.24 μm and 0.27 μm in the ST, 300°C aged and 400°C aged specimens, respectively. Additionally, the fraction of high angle grain boundaries (HAGBs) and the average misorientation of the boundaries in the aged-specimens were both higher than those in the ST specimen ARB processed to the same strain, which indicated that grain refinement during the ARB process was accelerated by the pre-existing precipitates. The reasons for the acceleration in microstructural evolution are considered to be the introduction of shear bands, the enhancement of dislocation multiplication and accumulation rate, and the inhibition of grain boundary migration by the precipitates in the pre-aged specimens.

Keywords: accumulative roll bonding (ARB) process, Al_3Sc precipitate, grain refinement

2.1. Introduction

Severe plastic deformation (SPD) techniques are now widely applied for the production of ultrafine-grained (UFG) microstructures in bulk metals having mean grain size smaller than 1 μm [1, 2]. These techniques have the advantage to produce fully dense materials without introduction of any contamination. Among the various SPD processes, accumulative roll bonding (ARB) is appropriate to manufacture UFG sheets, which are the most widely used shape of materials in industry. The ARB allows us to accumulate very large plastic strains into materials without changing the dimensions of the materials by repeating the processes of cutting the rolled sheet, stacking them to be the initial thickness and roll-bonding the stacked sheets again, as was explained in Chapter 1 [3]. In the present investigation, the ARB process was carried out on an Al-0.2wt.%Sc alloy having different starting microstructures, in order to examine the microstructural change of the alloy during the process.

Al-Sc alloys have recently received much interest because of their various advantages. Since fine Al_3Sc precipitates in Al-Sc alloys are thermally stable, grain growth of the matrix grains is greatly inhibited and fine grained structures can be maintained [4-8]. On the other hand, the presence of the second phase particles could potentially have a significant effect on microstructure evolution during SPD processes. For example, it is well known that second-phase particles can increase the rate of dislocation accumulation, and develop local deformation zones containing large local misorientation [9-11]. This can lead to an increased rate in generation of high angle grain boundaries (HAGBs) during plastic deformation [12-14]. However, most of previous researches on the influence of fine particles have been done in low strain deformations, and their effect on the grain refinement through grain subdivision [14, 15] by newly generated HAGBs during severe plastic deformation has not been well documented. In this study, pre-aged

Al-Sc specimens having two different sizes of precipitates, as well as the solution treated specimen, are prepared and then heavily deformed by the ARB process. The microstructure evolution in the pre-aged specimens is compared with that in the solution treated and ARB processed specimen in order to clarify the effect of pre-existing precipitates.

2.2. Experimental procedure

A binary Al-0.2 wt. % Sc alloy was prepared as sheets with thickness of 2 mm, width of 60 mm and length of 200 mm. The chemical composition of the Al-0.2%Sc alloy sheet is given in **Table 2.1**.

Table 2.1 Chemical composition of the Al-0.2 %Sc alloy studied. (wt. %)

Si	Fe	Cu	Mn	Mg	Cr	Zn	Ti	Sc
0.016	0.025	0.004	0.001	0.001	0.003	0.001	0.002	0.183

The sheets were firstly solution treated (ST) at 903K (630°C) for 86.4 ks and then immediately water-quenched. The average grain size of the matrix in the ST- sheets was 500 μm. Some ST- sheets were aged at 573 K (300°C) or 673 K (400°C) for 10 ks, in order to have two different sizes of Al_3Sc precipitates. The aging conditions were selected according to previous reports [15, 16]. Hereafter, those specimens are denoted as Aged- sheets. These ST-sheet and Aged- sheets were used as the starting materials for the ARB process. The starting sheets with the thickness of 2 mm were firstly cold-rolled by 50% reduction in thickness with lubrication. This procedure is considered as the first ARB cycle. A two-high rolling mill with 310mm diameter rolls was used for rolling at room temperature with lubrication at a rolling speed of 2.0 m min^{-1}. The same conditions were used for roll-bonding in the subsequent ARB process. In the subsequent ARB process, the 50% cold-rolled sheets with 1 mm thickness were cut into two with the half length in the rolling direction (RD), and then the contact surfaces of the sheets were degreased by acetone and wire-brushed by a stainless steel wire-brush. Two pieces of the sheets were stacked to be 2 mm thick in total and then roll-bonded by 50 % reduction in thickness by one pass. The roll-bonded sheets were immediately cooled in water. The same procedures were repeated up to 10 cycles including the first 50% cold-rolling, which corresponded to the total reduction in thickness of 99.9 % and the total equivalent strain of 8.0. Hereafter, the ST- and Aged-sheets ARB processed are denoted as ST-ARB, and Aged-ARB specimens, respectively. The starting material and the samples ARB processed by *N* cycles are expressed as ARB 0c and ARB *N*c specimens, respectively.

The microstructures on sections normal to the transverse direction (TD) of the sheets were characterized by electron backscattering diffraction (EBSD) in a scanning electron microscope with a field emission type gun (FE-SEM; Philips XL30) operated at 15 kV, and a transmission electron microscope (TEM; Hitachi H-800, Philips CM200 FEG, JEOL JEM2010) operated at 200 kV. The specimens for EBSD observation were mechanically polished and then electro-polished in a solution of 30% HNO_3 and 70% CH_3OH. Thin foil specimens for the TEM observation were prepared by mechanical polishing firstly down to a thickness of approximately 70 μm, and then electro-polishing in the same solution as that for the EBSD specimens.

2.3. Results

2.3.1. Starting microstructures

A bright field TEM image of the (a) ST- specimen, and dark field TEM images of the (b) 300°C Aged- specimen and (c) 400°C Aged-specimen before the ARB process are shown in **Fig. 2.1**. The TEM images of (b) and (c) were obtained from (100) plane diffraction of Al_3Sc. No precipitate is observed in the ST- specimen as shown in Fig. 2.1 (a). On the other hand, there are many fine spherical precipitates with mean particle diameter of 3.62 nm in the specimen aged at 300°C (Fig. 2.1 (b)). The corresponding diffraction pattern indicates that fine Al_3Sc precipitates have the identical orientation as the Al matrix, so that they have a certain orientation relationship with the matrix. On the other hand, in the specimen aged at 400°C, the coarse and cauliflower shaped precipitates with mean particle diameter of about 50 nm are observed in Fig. 2.1 (c). The corresponding diffraction pattern shows that the coarse Al_3Sc precipitates also have the identical orientation as the Al matrix. The results indicate that the Al_3Sc precipitate, especially finer ones, are considered to be coherent to the Al matrix, as the lattice constants of Al_3Sc and Al are very close to each other as was mentioned in Chapter 1. The size distribution of the precipitates in the aged specimens is plotted in **Fig. 2.2**. The size distribution of precipitates in the 300°C aged specimen is rather homogeneous than that in the 400°C aged specimen.

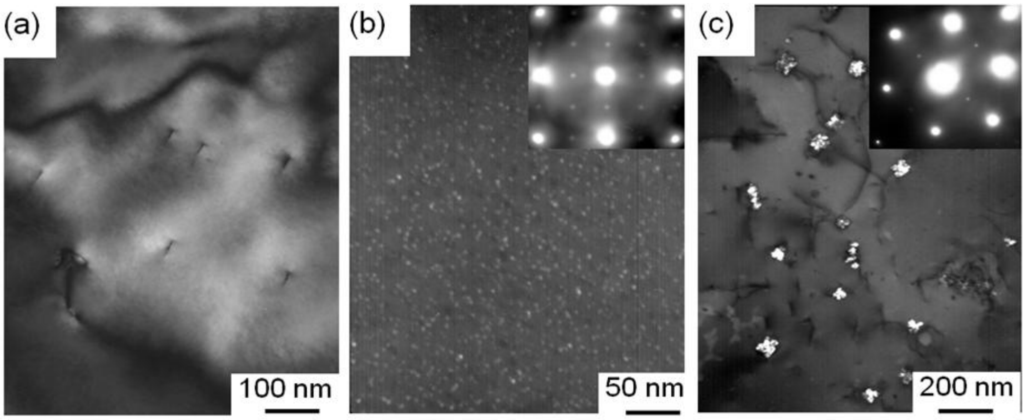

Fig. 2.1. Bright field TEM micrograph of (a) ST specimen, and dark field TEM images of (b) 300°C aged specimen and (c) 400°C aged specimen. (b) and (c) obtained from (100) diffraction of Al_3Sc.

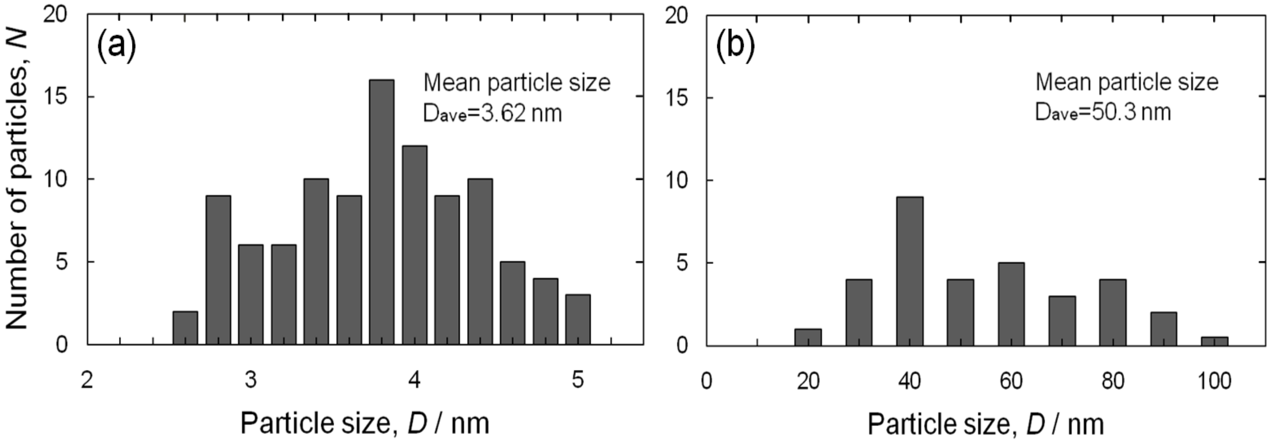

Fig. 2.2. Size distribution of the Al_3Sc particles in the (a) 300°C aged specimen and (b) 400°C aged specimen.

2.3.2. Microstructure evolution in matrix during ARB process

Figure 2.3 shows an optical micrograph of the ST specimen before the ARB process, containing coarse original grains with mean grain size of about 500 μm. The aged specimens also have similar grain size of the matrix. Grain boundary maps obtained from EBSD analysis of the ST-, 300°C Aged- and 400°C Aged-specimens after various cycles (strains) of the ARB process are shown in **Fig. 2.4**. The low-angle grain boundaries (LAGBs) with misorientation (θ) between 2° and 15° are drawn in red lines, while high-angle grain boundaries (HAGBs) with misorientation above 15° are drawn in green lines. Boundaries having misorientation smaller than 2° were omitted in order to remove the inaccuracy due to limited angular resolution in the EBSD measurment.

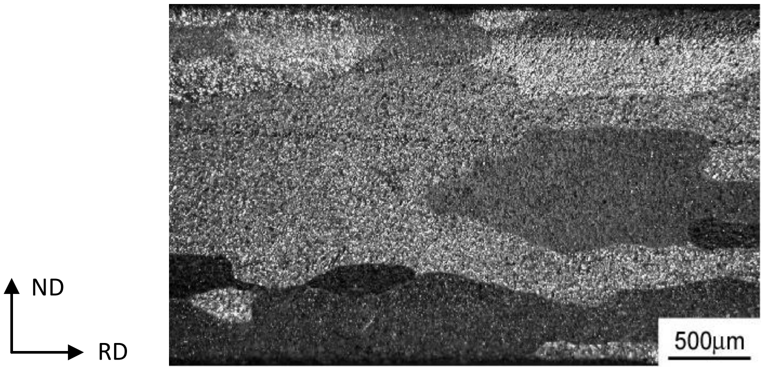

Fig. 2.3. Optical micrograph of the ST- specimen containing coarse matrix grains.

After the 1-cycle and 3-cycle ARB process, corresponding to equivalent strain $\varepsilon = 0.8$ and 2.4, respectively, the microstructures of the matrix are not uniform and consist of two kinds of grain sizes, i.e., fine grains and very coarse and elongated grains corresponding to the initial grains. The fine grains are surrounded by HAGBs while the coarse grains include LAGBs. It seems that the number of the fine grains surrounded by HAGBs and the amount of LAGBs are both larger in the 300°C Aged-ARB specimen than those in the other specimens. It is found that the 300°C Aged-ARB specimen shows large number of LAGBs aligned to specific orientations to RD, i.e., several LAGBs have a slope of approximately 45° against RD, which correspond to local shear bands shown later.

After the ARB process up to medium cycles (5 and 7 cycles corresponding to $\varepsilon = 4.0$ and 5.6, respectively), the microstructures are still inhomogeneous. Some regions include relatively high density of LAGBs while the other regions show elongated UFG structures with high density of HAGBs. It is found that the fraction of HAGBs in the 300°C Aged-ARB specimen is the largest among the specimens.

In the 10-cycle ARB processed specimens ($\varepsilon=8.0$), microstructures are homogeneous compared with the specimens ARB processed below 7-cycle. The specimens show lamellar boundary structures elongated to RD. In the two kinds of aged specimens having precipitates, the distribution of HAGBs is relatively homogeneous, and the most of grains are surrounded by HAGBs. It is found that the HAGB spacing in the 300°C Aged-ARB specimen is smaller than that in the 400°C Aged-ARB specimen. On the other hand, some coarse regions without HAGBs are retained in the ST-ARB specimen processed by 10-cycle ARB. The HAGB spacing in the ST-ARB specimen is larger than those in the Aged-ARB specimens.

From the results of the EBSD measurements, it is concluded that grain refinement by SPD is accelerated by pre-existing precipitates. This acceleration is presumably attributed to the inhibition of dislocation motion by the precipitates. In addition, the smaller precipitates seem more effective for grain-refinement.

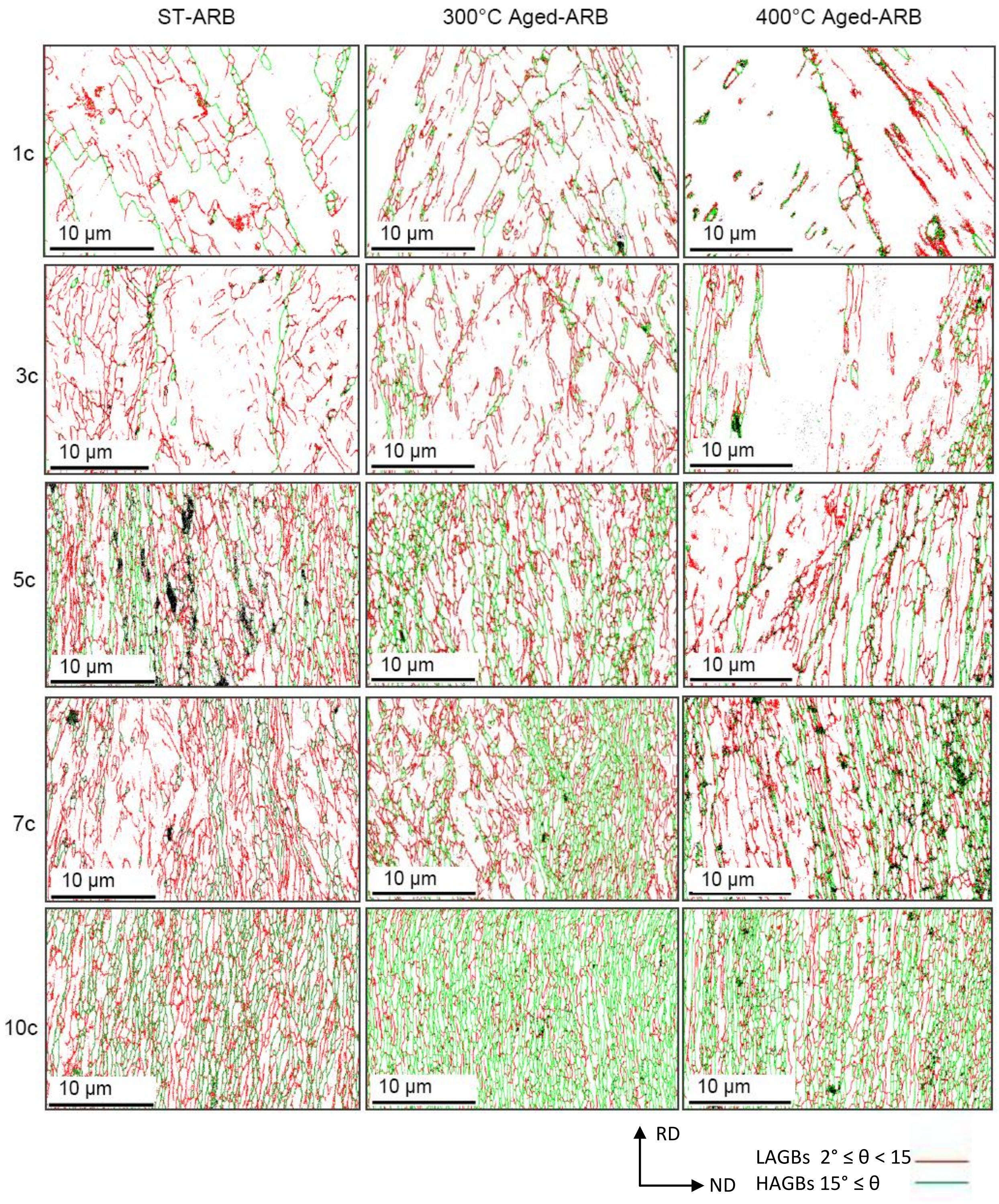

Fig. 2.4. Grain boundary maps obtained from EBSD measurement for the ST- and Aged- specimens ARB processed by various cycles at room temperature.

2.3.3. Quantification of microstructure evolution

The misorientation distribution obtained from the EBSD measurements of the ARB processed specimens are given in **Fig. 2.5** as fraction-misorientation histograms. The misorientation between neighboring measured points in the EBSD mapping data was calculated by software (OIM analysis version 5.6).

After 1 and 3 cycles, the shape of histograms is similar between all specimens, and the fraction of boundaries with misorientation smaller than 5° is very high. It reflects that dislocations or LAGBs were introduced during ARB process. In the specimens ARB-processed above 5 cycles, the fraction of small misorientation decreases gradually with increasing the number of ARB cycles while the fraction of HAGBs increases. After 10-cycle ARB process, the fraction of LAGBs in the ST-ARB and 300°C Aged-ARB specimens decreases to less than 10%. In these specimens, the fraction of misorientation ranging from 45° to 50° is the highest, indicating that the misorientation distribution is close to random [15, 16]. On the other hand, the fraction of the LAGBs in the 400°C Aged-ARB specimen remains more than 10% after 10-cycle ARB process.

Change in the grain size, d_t , as a function of the number of ARB cycle is given in **Fig. 2.6 (a)**. The d_t is evaluated as the mean spacing of HAGBs along ND by linear intercept method in the EBSD boundary maps. From the figure, it is found that the d_t decreases with increasing the number of ARB cycles. After 1-cycle of ARB processing, the d_t of the 300°C Aged-ARB, 400°C Aged-ARB and ST-ARB specimens are 0.9μm, 2.3μm and 2.1μm, respectively, though the initial grain size was several hundred micrometers. The d_t of the specimens decreases down to approximately 0.4 μm with increasing ARB cycle up to 5-cycle. Afterwards, the d_t decreases slightly with increasing the number of ARB cycles.

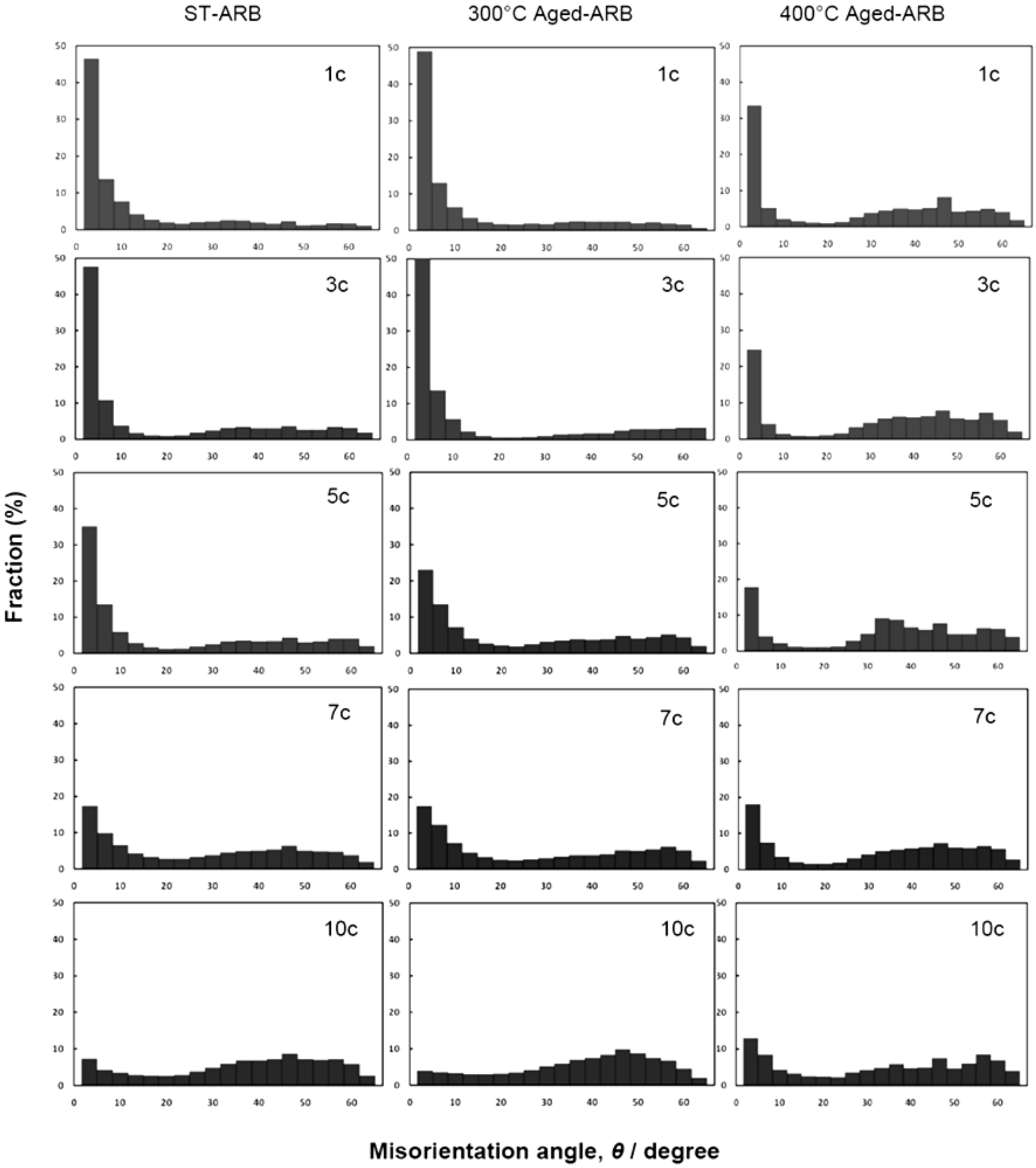

Fig. 2.5. Misorientation distribution in the ST- and Aged-specimens ARB processed by various cycles.

The d_t of the 300°C Aged-ARB specimen is much smaller than that of the other specimens below 5-cycle, indicating that the fine precipitates in the 300°C Aged-ARB specimen enhances the rate of grain-refinement during the ARB process. After 10 cycles of ARB processing, the d_t

reduces down to 0.24μm, 0.27μm and 0.37μm for the 300°C Aged-ARB, 400°C Aged-ARB and ST-ARB specimens, respectively.

The above results indicate that the fine Al_3Sc precipitates in the 300°C Aged-ARB specimen affect the grain refinement up to 5-cycle, but the influence of the precipitates at 10-cycle is not as obvious as that in the specimens ARB processed below 5 cycles. This indicates that the fine pre-existing precipitates have a significant effect on microstructure refinement at relatively low strains.

The fraction of HAGBs, f_{HAGBs}, in the specimens is plotted as a function of the number of ARB cycles in **Fig. 2.6 (b)**. The f_{HAGBs} increases monotonically with increasing the number of ARB cycles. After 10 cycles, the f_{HAGBs} of the 300°C Aged-ARB, 400°C Aged-ARB and ST-ARB specimens is 72.4%, 61.6% and 53.3%, respectively. It is found that the f_{HAGBs} of the ST-ARB specimen is always lower than those of the 300°C Aged-ARB and 400°C Aged-ARB specimens at the same ARB cycle. In addition, the f_{HAGBs} of the 300°C Aged-ARB specimen is larger than that of the 400°C Aged-ARB specimen. These results show that the rate of HAGBs formation is also affected by the pre-existing precipitates, and that the finer precipitates are more effective for the formation of HAGBs during the ARB process.

Figure 2.6 (c) shows the average misorientation angle, θ, as a function of ARB cycles. It can be seen that the average misorientation angle increases with increasing the number of ARB cycles in all specimens. The average misorientation angles in the two kinds of Aged-ARB specimens are higher than that in the ST-ARB specimen. In the 300°C Aged-ARB and ST-ARB specimens, the average misorientation angle increases monotonically with increasing the number of ARB cycles up to 10 cycles. In case of the 400°C Aged-ARB specimen, the average misorientation increases up to 5-cycle of ARB, and then keeps nearly a constant value.

Furthermore, the 400°C Aged-ARB specimen has higher misorientation angle than the 300°C Aged-ARB specimen, although they have almost the same value of mean misorientation after the 10-cycle of ARB.

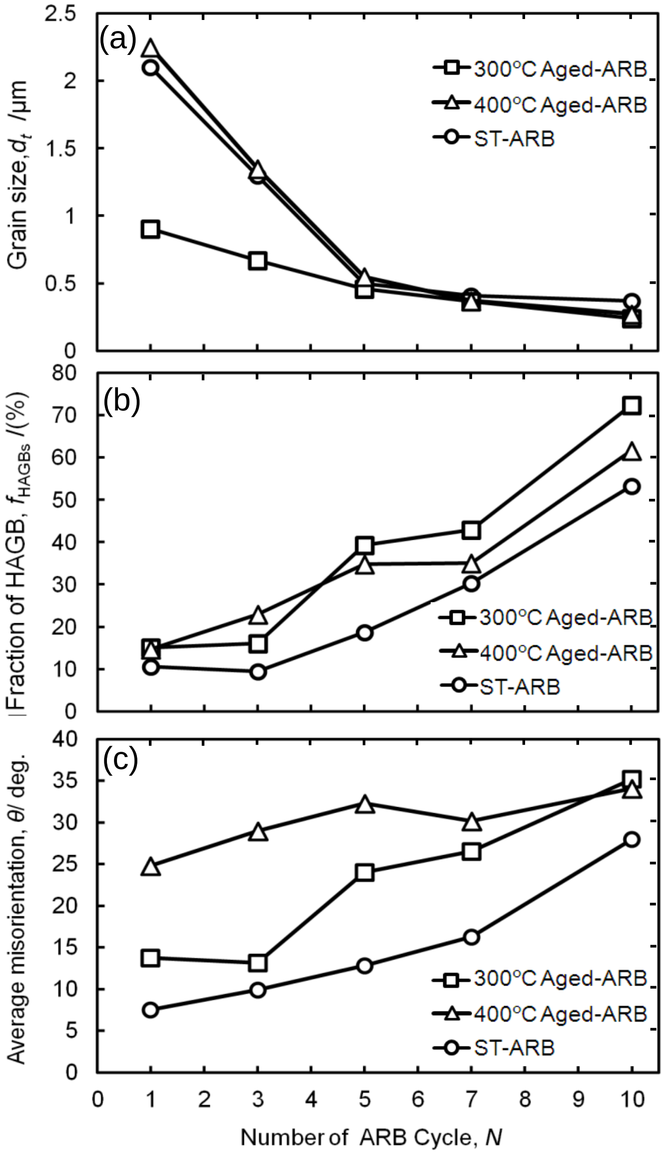

Fig. 2.6. Change in the average grain size, d_t, (a), fraction of high angle boundary, f_{HAGBs}, (b) and average misorientation, θ, (c) in the ARB processed specimens as a function of the number of ARB cycles.

2.3.4. TEM observation of ARB processed specimens

Figure 2.7 shows the TEM micrographs of the 300°C Aged-ARB and 400°C Aged-ARB specimens ARB processed by 1 cycle. The typical pictures were chosen from several TEM micrographs observed from TD in each kind of specimen. Some shear bands indicated by arrows are observed in the Aged-ARB specimens, though shear bands have not been observed in the ST-ARB specimen [17] and pure aluminum in previous ARB studies [18-20]. These results indicate that the shear bands introduced during the present ARB process are caused by the presence of pre-existing precipitates. The shear bands correspond to the aligned LAGBs observed in the EBSD maps (Fig. 2.4) which had a slope of approximately 45° against RD. Fine lamellar boundary structures are found within the shear bands in TEM (Fig. 2.7 (b)). From the figures, width of the shear bands in the 300°C Aged-ARB specimen is narrower and the number of the shear bands in the 300°C Aged-ARB specimen is somehow larger than those in the 400°C Aged-ARB specimen. This fact was also confirmed in large scale EBSD maps with area size of 500μm × 100μm. It is considered that the finer precipitates enhance to introduce shear bands much more effectively. Introduction of shear bands during SPD processes have been also reported elsewhere [10, 11, 21-23].

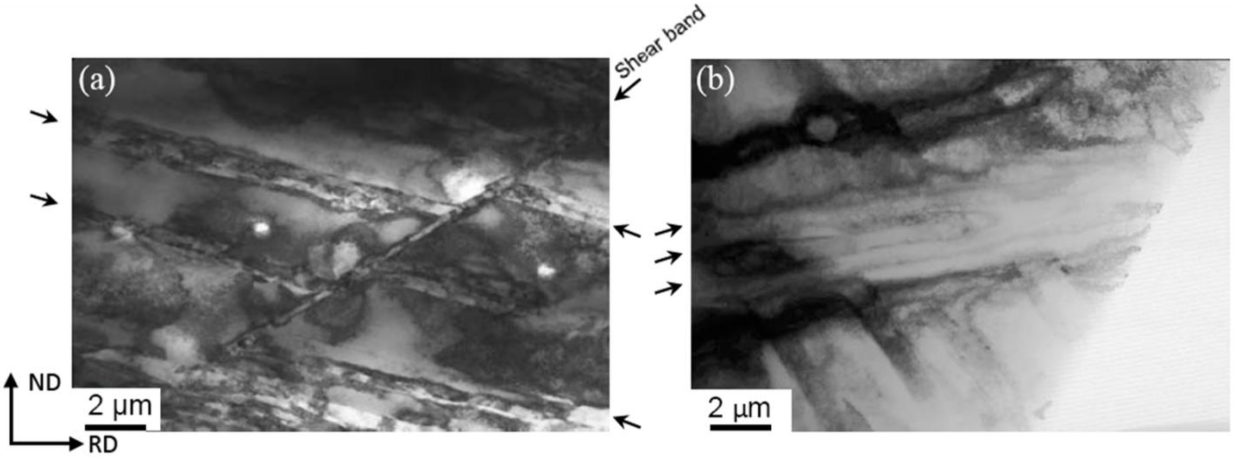

Fig. 2.7. TEM micrographs of the (a) 300°C Aged-ARB 1-cycle specimen and (b) 400°C Aged-ARB 1-cycle specimen.

Typical TEM microstructures of the Aged-ARB specimens after 1-cycle are shown in **Fig. 2.8** (a) and (b). The TEM micrographs were observed from TD. The microstructures indicate that the Al_3Sc precipitates are distributed randomly in the matrix. It is also observed that a high-density of dislocations interact with Al_3Sc precipitates especially in the 400°C Aged-ARB specimen. It is expected that the accumulation of dislocations was accelerated because the dislocation motion is inhibited by the precipitates during the ARB process.

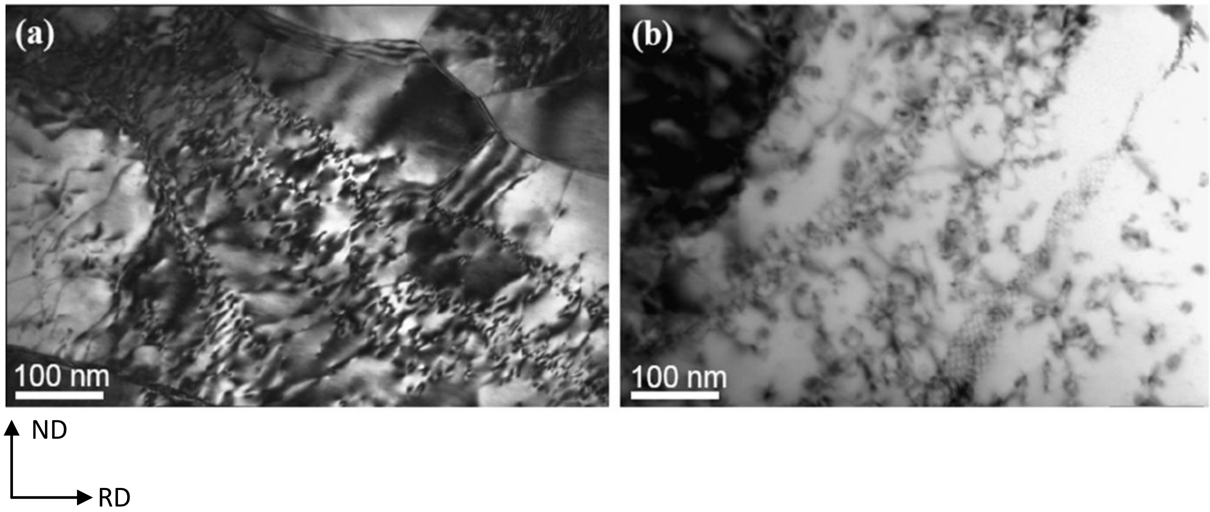

Fig. 2.8. TEM micrographs of the (a) 300°C Aged-ARB 1cycle and (b) 400°C Aged-ARB 1-cycle specimens.

Figures 2.9 shows TEM micrographs of the ST-ARB, 300°C Aged-ARB and 400°C Aged-ARB specimens processed by 9 cycles. The TEM micrographs were observed from TD. From the figures (Fig. 2.9 (a)-(c)), the specimens ARB processed by 9 cycles show the lamellar boundary structure elongated to RD which is a typical ultra-fine microstructure formed by the ARB process [24, 25]. The mean boundary spacing along ND is approximately 400 nm, 330 nm and 350 nm in the ST-ARB, 300°C Aged-ARB and 400°C Aged-ARB specimens, respectively. Shear bands were not observed in the 9-cycle ARB processed specimen.

In case of the ST-ARB and 300°C Aged-ARB 10c specimens (Fig. 2.9 (a) and (b)), it seems that dislocation density is fairly low within the lamellar grains. On the other hand, large numbers of dislocations exist within the elongated grains in the 400°C Aged-ARB specimen (Fig. 2.9 (c)). Figure 2.9 (d) shows a dark field TEM micrograph for the 400°C Aged-ARB specimen processed by 10-cycle. Tangled dislocations are clearly observed within the lamellar grains.

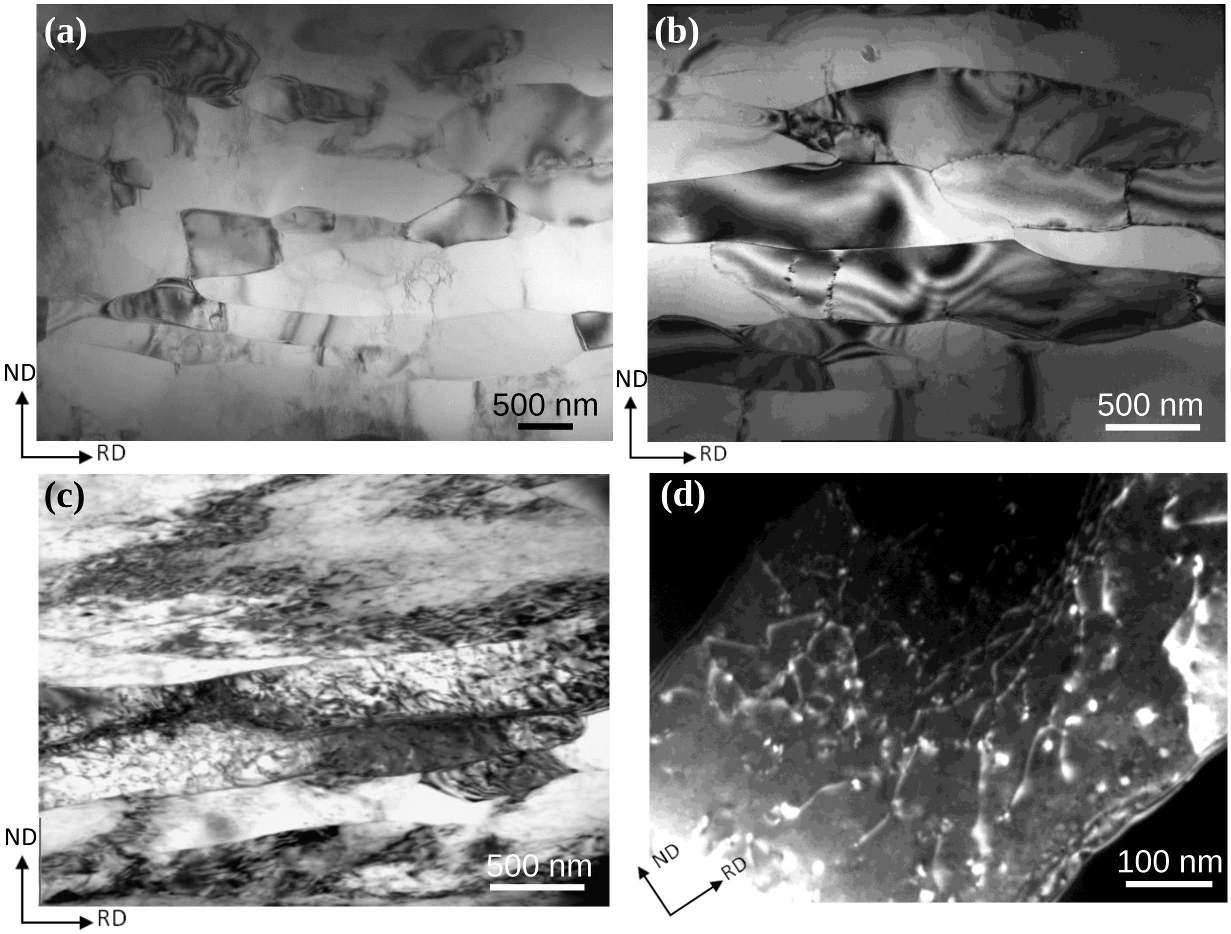

Fig. 2.9. TEM micrographs of the (a) ST-ARB 9-cycle, (b) 300°C Aged-ARB 9-cycle, (c) 400°C Aged-ARB 9-cycle and (d) 400°C Aged-ARB 10-cycle specimens.

2.3.5. Change in precipitates in aged- specimens during ARB process

In this section, the change in Al_3Sc precipitates in the aged specimens during the ARB process is focused and discussed. **Figure 2.10** shows (a) a TEM micrograph of the 300°C Aged-ARB specimen after 1-cycle ARB, (b) a corresponding selected area diffraction (SAD) pattern and (c) a key diagram corresponding to the SAD pattern. Although it is difficult to observe very fine precipitates in Fig. 2.10 (a), the diffraction pattern of Fig. 2.10 (b) includes the diffraction spots corresponding to Al_3Sc precipitate, which are indicated by arrows. From the SAD pattern, it is found that the crystal planes (100) and (110) of the Al_3Sc precipitates are parallel to the crystal planes (200) and (220) of the Al matrix, respectively. The results indicate that the precipitates keep the identical orientation to the Al matrix after 1-cycle of ARB process. Thus, it is expected that the precipitates keeps coherency to the matrix.

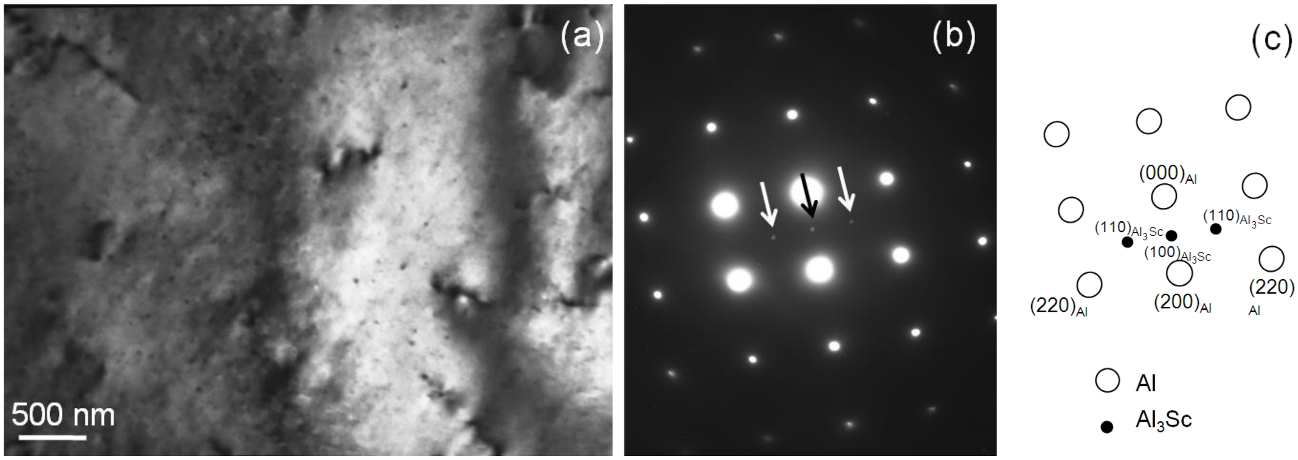

Fig. 2.10. TEM micrographs of the 300°C Aged-ARB specimen after 1-cycle ARB process. (a) TEM microstructure, (b) SAD pattern and (c) key diagram.

High resolution TEM (HRTEM) micrographs of the 300°C Aged-ARB specimen after 9 cycles are shown in **Fig. 2.11** (a) and (b). Several straight lines due to stacking faults, indicated by arrows, are observed in these figures. Tetragonal regions surrounded by white broken lines in the images were analyzed by fast Fourier transformation (FFT). The results of the FFT analysis corresponding to diffraction patterns are given in Fig. 2.11 (c) and (d) with related key diagrams. From Fig. 2.11 (c), it is found that the precipitate in Fig. 2.11 (a) keeps the identical orientation with the matrix, which has been found in the aged specimen before the ARB process. On the other hand, the orientation of the precipitates in Fig. 2.11 (b) is different from that confirmed in the starting microstructure of the aged specimens. Accordingly, it is supposed that the orientation relationship between some precipitates and matrix is changed during ARB process.

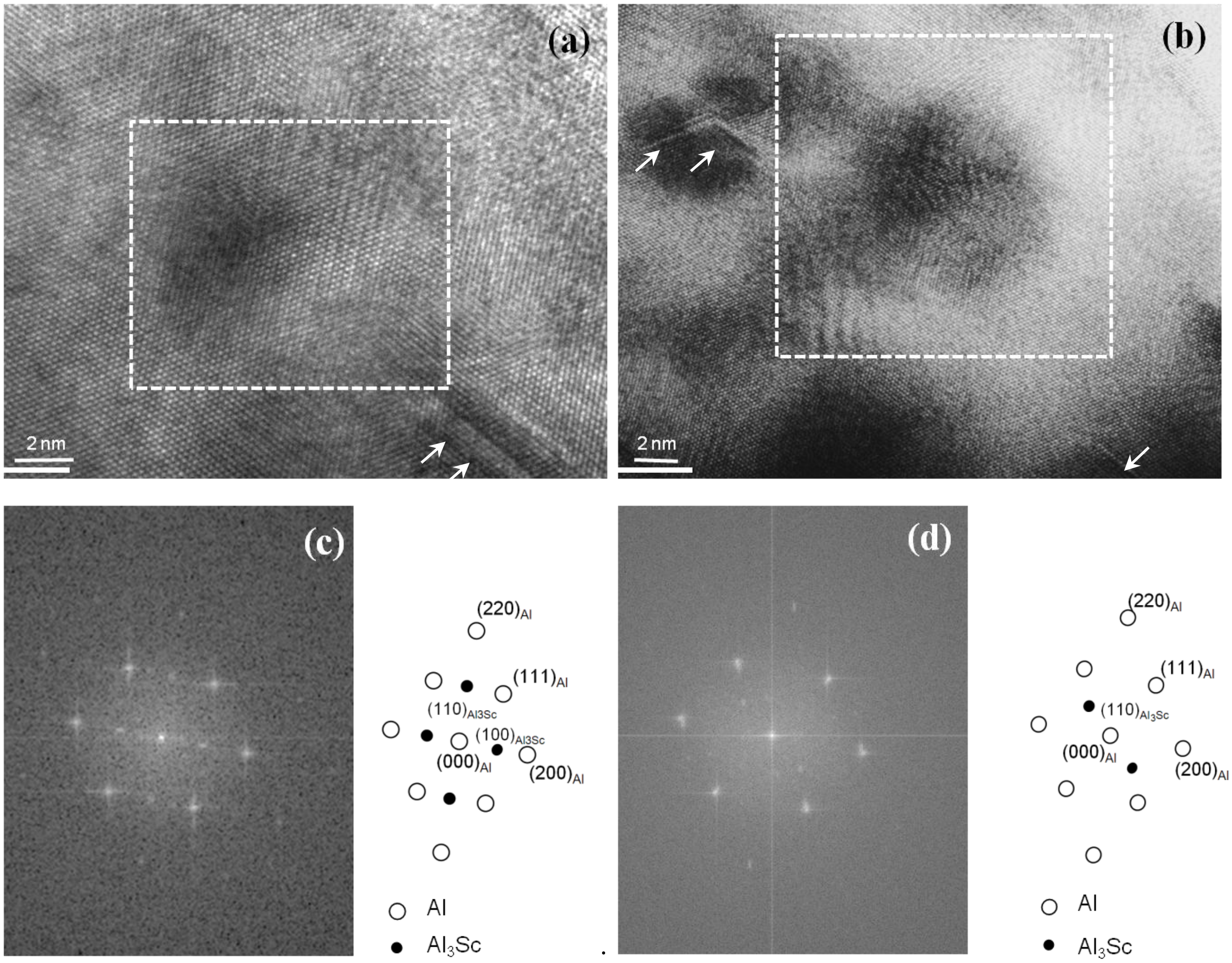

Fig. 2.11. High resolution TEM micrograph of Al_3Sc precipitates in the 300°C Aged-ARB specimen after 9-cycle of ARB. (a) A precipitate having the identical orientation relationship with matrix, and (b) a precipitate with different orientation relationship with matrix. (c) and (d) are corresponding diffraction patterns obtained by FFT analysis for the areas surrounded by broken lines in (a) and (b), respectively.

TEM microstructures of the 400°C Aged-ARB specimen after 1-cycle of ARB are shown in **Fig. 2.12**; (a) is a bright field image, (b) is a dark field image corresponding to a diffraction spot of Al_3Sc precipitates, and (c) is a corresponding diffraction pattern and key diagrams. From these figures, it is obvious that the precipitates keep the identical orientation to the Al matrix. A high-resolution TEM micrograph of the 400°C Aged-ARB specimen after 9-cycle of ARB is shown in **Fig. 2.13** with the FFT image and the key diagram. Similar orientation between the precipitates and matrix is confirmed as shown in the related diffraction pattern. It should be noted that significant reduction in particle size after 1 cycle is observed in the 400°C Aged-ARB specimen, indicating that the precipitates are fragmented and might be dissolved during ARB processing.

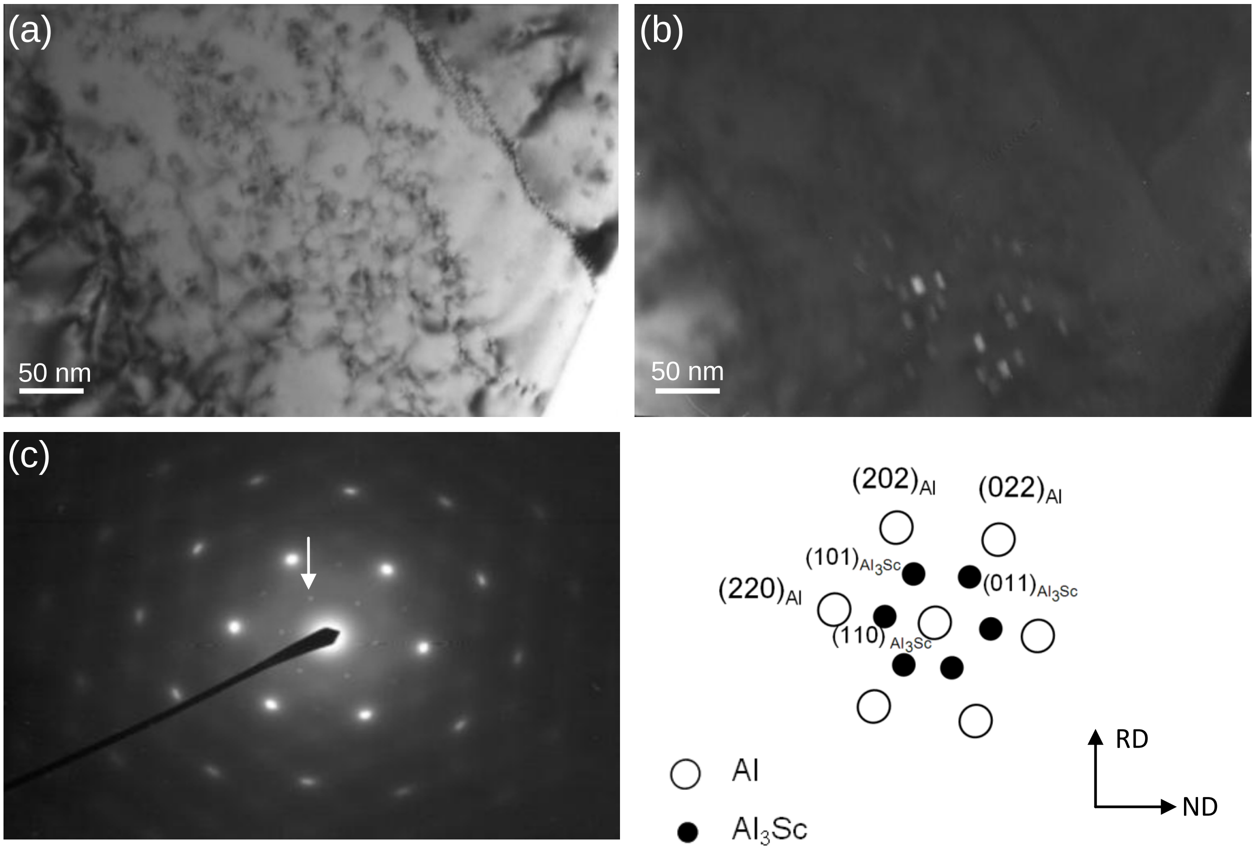

Fig. 2.12. TEM micrographs of the 400°C Aged-ARB specimen deformed by 1-cycle ARB: (a) Bright field image, (b) dark field image and (c) SAD pattern with key diagram.

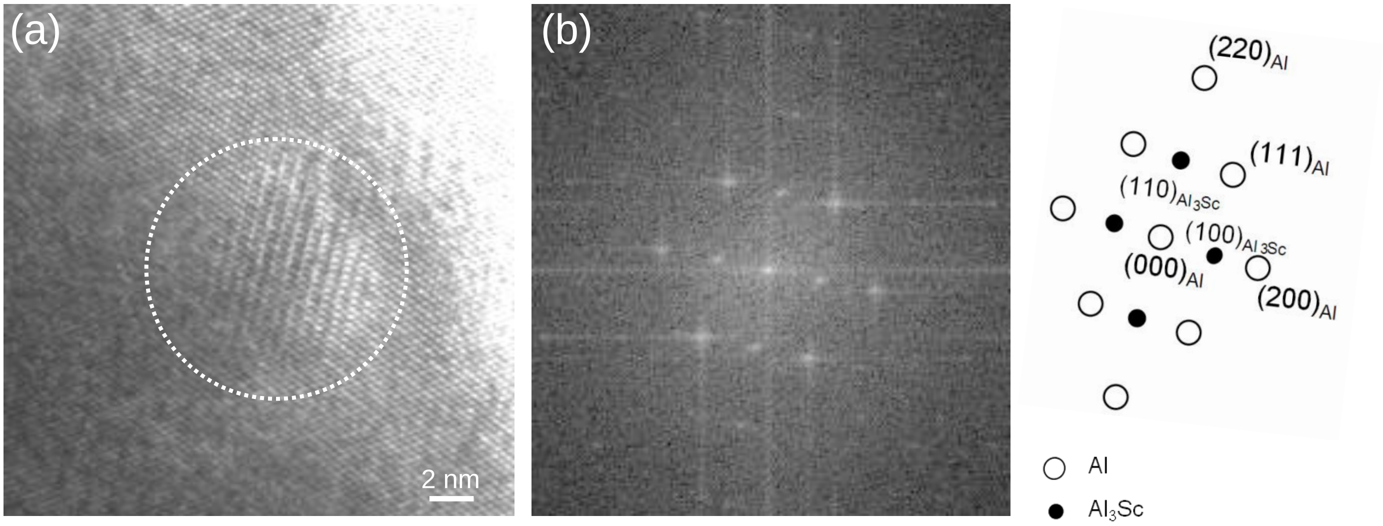

Fig. 2.13. A high-resolution TEM image of a Al_3Sc precipitate in the 400°C Aged-ARB specimen deformed by ARB up to 9-cycle. (a) A precipitate having the same orientation relationship with matrix, and (b) corresponding FFT pattern for the area surrounded by broken circular lines in (a).

TEM micrographs of the 400 °C Aged-ARB specimen processed by 10 cycles are shown in **Fig. 2.14**. The diffraction pattern obtained from the region surrounded by a circle of broken line in Fig. 2.14 (a) is shown in (b). In Fig. 2.14 (b), two kinds of diffraction spots indicated by arrows 1 and 2 are observed. Both of the spots indicated by arrows correspond to Al_3Sc precipitates. Figure 2.14 (c) and (d) show the dark field images obtained from the spots corresponding to the arrow 1 and arrow 2, respectively. It appears that the diffraction spot indicated by the arrow 1 keeps the specific orientation relationship between the precipitates and the matrix. On the other hand, the diffraction spot indicated by the arrow 2 is deviated from the position for a diffraction spot shown by arrow 1. It is found that the brightness of precipitates are different between Fig. 2.14 (c) and (d). The result indicates that the orientation relationship between some Al_3Sc precipitates and matrix is changed in the 400°C Aged-ARB specimen even within the identical matrix grain, probably due to plastic deformation during 9-cycle ARB.

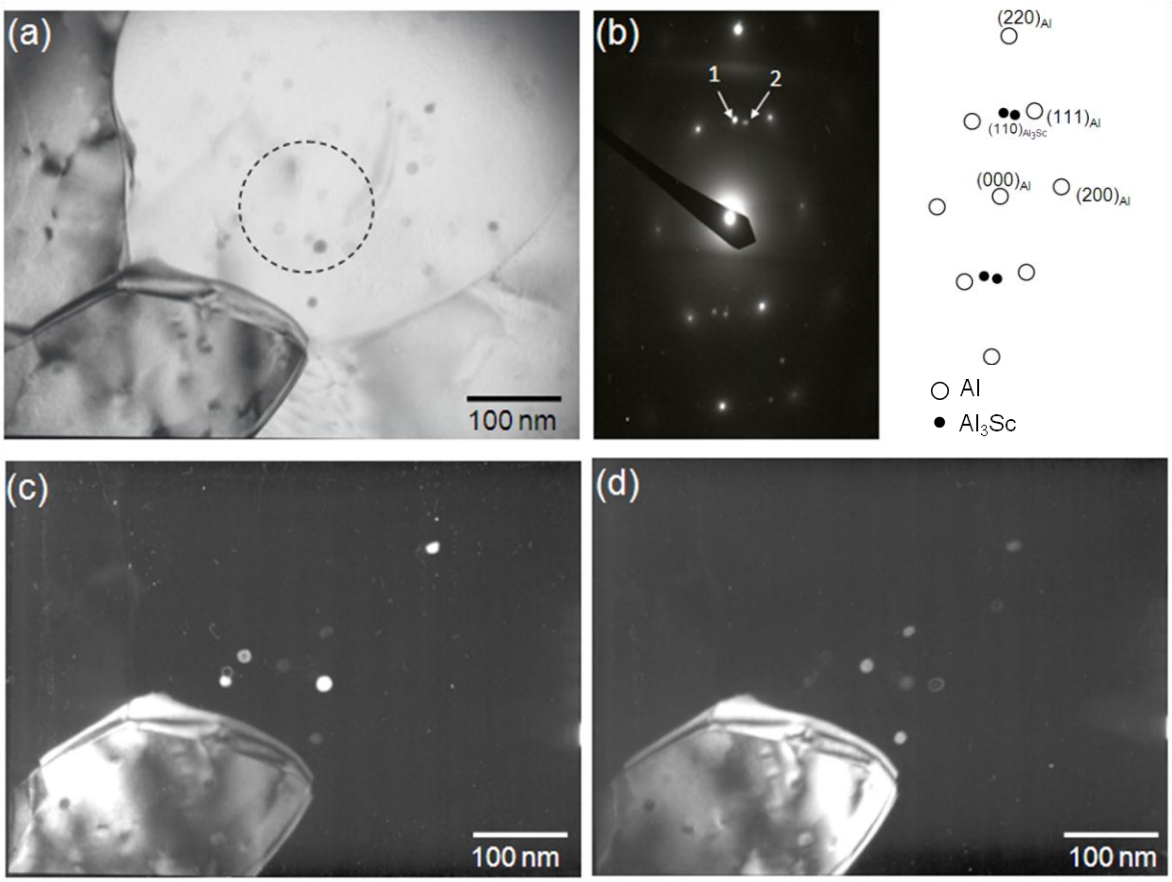

Fig. 2.14. TEM micrographs of the 400°C Aged-ARB specimen after 10 cycles showing (a) a bright field image, (b) corresponding diffraction pattern for the area surrounded by broken circular line in (a) and key diagram. (c) and (d) are dark field images corresponding to the arrow 1 and arrow 2 in (b), respectively, showing different orientation of Al_3Sc particles with respect to the matrix.

Additionally, it is noteworthy that the precipitates with spherical morphology in the 400 °C Aged-ARB specimen after 9-cycle of ARB have an average diameter of approximately 10 nm, though the cauliflower shaped precipitates in the starting sheet have mean particle size of 50 nm prior to the ARB process. It is expected that the coarse Al_3Sc precipitates are dissolved and re-precipitated, or fragmented into small ones during the ARB process.

2.4. Discussion: Effect of pre-existing precipitates on microstructural evolution

From the microstructural observations, it is found that the grain refinement during the ARB process is accelerated by the pre-existing precipitatfores. For example, the fraction of HAGBs and the average misorientation in the aged-specimens including the pre-existing precipitates are higher than those in the ST-specimen at the same ARB cycle (Fig. 2.6). At low ARB cycles, the matrix grain size of the 300 °C Aged-ARB specimen is much smaller than that of other specimens (Fig. 2.6). In this section, reasons for the acceleration in the grain refinement due to the pre-existing precipitates are discussed.

One of the possible reasons for the grain-refinement acceleration is an influence of the pre-existing precipitates on dislocation motion during plastic deformation. It has been reported that precipitates can increase the rate of dislocation generation by encouraging the formation of Orowan and prismatic loops [10, 18, 26-29]. In addition, precipitates inhibit the long-range migration of dislocations, so that uniform slip of dislocations become difficult and development of local deformation zones containing large local misorientation gradients is promoted. Barlow *et al*. [30] have actually reported an accelerated grain refinement in precipitate bearing aluminum as well as enhanced dislocation generation and reduction in the slip distances during conventional deformation. The relationship between dislocation density in a specimen with precipitates, ρ_D, and in a precipitate free alloy, ρ_s, can be described by following equation [27, 31].

$$\frac{\rho_D}{\rho_S} = \frac{3 f_V L}{r} \tag{2.1}$$

where f_v, r and L are the volume fraction of precipitates, mean radius of precipitates and slip length in the single-phase alloy, respectively. Equation (2.1) gives approximately an order of magnitude increase in dislocation density in the specimen with precipitates relative to that in the precipitate free specimen [31]. The increase in dislocation density leads to the increase of the formation rate of HAGBs in grain subdivision process. In the TEM micrographs of Fig. 2.8, high-density of dislocations are observed in the aged-specimens at early stages of ARB. The fraction of HAGBs in the aged-specimens is higher than that in the ST-specimen during the ARB process. Moreover, the fraction of HAGBs in the 300 °C Aged-ARB specimen is higher than that of the 400 °C Aged-ARB specimen. The result can be explained by the expected increase in the dislocation multiplication rate in the 300 °C Aged-ARB specimen having finer precipitates than those in the 400 °C Aged-ARB specimen. It is summarized that the pre-existing precipitates increase the rate of dislocation multiplication and accumulation, resulting in the acceleration of the HAGBs formation during the ARB process.

As is mentioned above, large number of precipitates inhibit uniform dislocation slips and result in inhomogeneous deformation and also instability like shear banding. Introduction of shear bands during SPD processes have been also reported in previous literatures [10, 11, 21-23]. Introduction of shear bands also results in subdivision of original crystals, especially subdivision of elongated or lamellar grains. Thus, another possible reason for the acceleration in grain refinement in the present study is shear banding during the ARB process. Actually, the shear bands were observed in the Aged-ARB specimens (Fig. 2.7), while they were hardly observed in the ST-ARB specimen. It seems from the EBSD boundary maps (Fig. 2.4) that the shear bands were mainly introduced at low ARB cycles. Furthermore, the number of the shear bands introduced by the ARB process in the 300 °C Aged-ARB specimen was larger than that in the 400 °C Aged-ARB specimen (Fig. 2.7), probably because finer and denser precipitates made uniform slips more difficult. It corresponds to the experimental result that the grain size of the

300 °C Aged-ARB specimen was smaller than that of the 400 °C Aged-ARB specimen at low ARB cycles (Fig. 2.6). Therefore, it is concluded here that the pre-existing precipitates inhibit uniform dislocation slips in the matrix to result in strain localization like shear banding, which leads to acceleration of grain refinement during the ARB process, especially at low ARB cycles. In addition, the effect of finer precipitate is more effective on such acceleration.

By the way, it was also found from the microstructural observation that the grain size (the thickness of grains) saturated above 7 cycles of ARB (Fig. 2.6 (a)). The result suggests that a kind of microstructure coarsening including boundary migration occurs during the ARB process. Such a microstructure coarsening during the ARB process is probably affected by the pre-existing precipitates. Thus, the interaction between the precipitates and grain boundaries is also considered as another effect of the pre-existing precipitates on microstructural evolution during the ARB process. **Figure 2.15 (a)** shows TEM micrographs of the 400°C Aged-ARB specimen after 9-cycle of ARB process. Figure 2.15 (b) is a higher magnification TEM micrograph around the grain boundary of Fig. 2.15 (a). In the figures, a wavy boundary is found to be pinned by the precipitates. This indicates that the grain boundary migration happens during the ARB process. It is well known that fine precipitate can inhibit grain boundary migration by so-called Zener drag effect. The Zener dragging force, *F*, is shown as follows:

$$F = \frac{3}{8}\left(\frac{f}{r^2}\right) \gamma D_g \qquad \text{for a low-angle boundary} \tag{2.2}$$

$$F = \frac{3}{2}\left(\frac{f}{r^2}\right) \gamma D_g \qquad \text{for a high-angle boundary} \tag{2.3}$$

where f is the volume fraction of second phase particles, r *is* the mean particle radius, D_g is the size of the grains and γ *is* the interface energy. It is found that F becomes larger when the Al_3Sc precipitates have finer size (r) and keep identical orientation to the matrix, which results in lower interface energy (γ) [32, 33]. In the experimental results, the thicknesses of the elongated grains after 10 cycles were 0.24 μm, 0.27 μm and 0.37 μm for the 300°C Aged-ARB, 400°C Aged-ARB and ST-ARB specimens, respectively. The grain size of the Aged-ARB specimens is smaller than that in the ST-ARB specimen. In addition, the specimen with the finer pre-existing precipitates consists of smaller grain size. The results also agree qualitatively with the magnitude of Zener dragging force expected from the equations (2.2) and (2.3). Hence, it can be said that the Aged-ARB specimens having the pre-existing precipitates showed smaller matrix grain size than the ST-ARB specimen because the pre-existing precipitates inhibited grain boundary migration during the ARB process. However, we should note that the ultrafine grained structures in the ARB processed specimens are not controlled only by the grain growth but are mainly controlled by grain subdivision during heavy plastic deformation. Therefore, the Zener drag would give a minor effect on microstructure evolution at high ARB cycles.

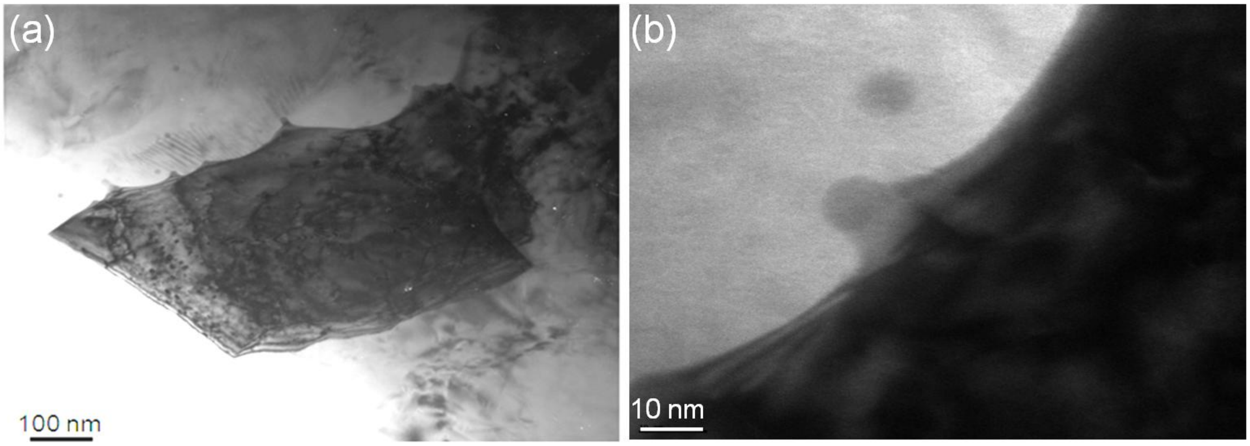

Fig. 2.15. TEM micrographs of (a) 400°C Aged-ARB specimen after 9 cycles showing interaction between Al_3Sc and the boundaries, and (b) higher magnification TEM micrograph around the grain boundary of (a).

It can be concluded that the important roles of the pre-existing precipitate in the microstructural evolution during the ARB process are firstly to increase the generation and accumulation rate of dislocation and secondarily to introduce shear bands at low ARB cycles, as well as to inhibit the grain boundary migration at high ARB cycles as a minor effect. The roles of the pre-existing precipitation lead to acceleration of grain refinement and decrease in grain size obtained by ARB process.

2.5. Conclusions

Microstructural evolution during severe plastic deformation by ARB process up to 10 cycles (equivalent strain of 8.0) was investigated in a solution treated specimen and pre-aged specimens of an Al-0.2% Sc alloy. The main results are summarized as follows:

(1) Coherent precipitates of Al_3Sc with mean particle size of 50 nm which showed a cauliflower-like shape were observed after aging at 400°C for 10 ks. On the other hand, fine, spherical, and coherent precipitates with mean particle size of 3.6nm were found after aging at 300°C.

(2) After 10 cycles of ARB, ultrafine lamellar boundary structures were observed in all specimens. The mean grain thickness of the elongated ultrafine grains in the Aged-ARB specimens containing precipitates was smaller than that in the ST-ARB specimen. The fraction of high angle grain boundaries (HAGBs) and the average misorientation in the Aged-ARB specimens were larger than those in the ST-ARB specimen. The results showed that pre-existing Al_3Sc precipitates accelerated the grain refinement during the ARB process.

(3) The acceleration of the grain refinement was considered to be caused by the increase in the generation and accumulation rate of dislocations due to the pre-existing precipitates as well as by the introduction of shear bands. After many cycles of the ARB process, the saturated grain sizes in the Aged-specimens were smaller than that in the ST-specimen. The

precipitates also played an additional role to inhibit short range grain boundary migration at later stage of ARB through Zener drag effect. It was also found that the effects of the finer pre-existing precipitates in the 300°C Aged-ARB specimens on grain refinement were more effective than that of the coarse precipitate in the 400°C Aged-ARB specimens.

(4) From the TEM observations, it was found that the state of the precipitates changed during the ultrahigh strain deformation by ARB process. The identical orientation between the precipitates and Al matrix was kept during 1 cycle of ARB process. However, some precipitates have different orientation with matrix after 9 cycles. Additionally, the cauliflower shaped precipitates observed in the 400°C Aged-ARB specimens were changed to the fine and spherical-shaped ones after many ARB cycles. From the result, it was expected that the coarse Al_3Sc precipitates in the 400°C Aged-ARB specimen were dissolved and re-precipitated, or fragmented by plastic deformation during the ARB process.

References

[1] R.Z. Valiev, R.K. Islamgaliev, I.V. Alexandrov, Progress in Materials Science 45 (2000) 103.

[2] R.Z. Valiev, Y. Estrin, Z. Horita, T.G. Langdon, M.J. Zehetbauer, Y.T. Zhu, Journal of Metal 58 (4) (2006) 33.

[3] N. Tsuji, Y. Saito, Y. Minamino, Advanced Engineering Materials 5 (2003) 5.

[4] V. Jindal, P.K. De, K. Venkateswarlu, Materials Letters 60 (2006) 3373.

[5] J. Gubicza, I. Schiller, N.Q. Chinh, J. Illy, Z. Horita, T.G. Langdon, Materials Science and Engineering A 460-461 (2007) 77.

[6] E. A. Marquis and D. N. Seidman, Acta Materialia 49 (2001) 1909.

[7] G.M. Novotny, A.J. Ardell, Materials Science and Engineering A 318 (2001) 144.

[8] B.K. Min, H.W. Kim, S.B. Kang, Materials Processing Technology 162-163 (2005) 355.

[9] F.J. Humphreys, P.B. Hirsch, Philosophical Magazine 34 (1976) 373.

[10] F.J. Humphrey, Acta Metallurgica 27 (1979) 1801.

[11] H. Jazeri, F.J. Humphreys, In: G. Gottstein, D.A. Molodov, Editors. 5th Int. Conference on Recrystallization and Related Annealing Phenomena, Belgium (2001) 549.

[12] P. J. Apps, J. R. Bowen, P. B. Prangnell, In: M. Zehetbauer, R.Z. Valiev, Editors. Nanomaterials by Severe Plastic Deformation-NANSPD2, Austria (2002) 138.

[13] P. J. Apps, J.R. Bowen, P. B. Prangnell, Acta Materialia 51 (2003) 2811.

[14] F. J. Humphreys, In: M. H. Lorett, Editor. Dislocations and Properties of Real Materials. London (1984) 175.

[15] P. J. Apps, M. Berta, P. B. Prangnell, Acta Materialia 53 (2005) 499.

[16] H. Jazaeri, F.J. Humphreys, Acta Materialia 52 (2004) 3251.

[17] M. Z. Quadir, M. Ferry, O. Al-Buhamad, P.R. Munroe, Acta Materialia 57 (2009) 29.

[18] S. H. Lee, Y. Saito, N. Tsuji, H. Utsunomiya, T. Sakai, Scripta Materialia 46 (2002) 281.

[19] H. Pirgazi, A. Akbarzadeh, R. Petrov, L. Kestens, Amaterils Science and Engineering A 497 (2008) 132.

[20] S. Li, F.Sun, H.Li, Acta Materialia 58 (2010) 1317.

[21] A. Goloborodko, O. Sitdikov, T. Sakai, R. Kaibyshev, H. Miura, Materials Transaction 44 (2003) 766.

[22] O. Sitdikov, T. Sakai, E. Avtokratova, R. Kaibyshev, K. Tsuzaki, F. J. Humphrey, Acta Metallurgica 27 (1979) 1801.

[23] O. Sitdikov, T.Sakai, A.Goloborodko, H. Miura, R. Kaibyshev, Philosophical Magazine 85 (2005) 1159.

[24] N. Tsuji, Y. Saito, S.H. Lee, Y. Minamino, Advanced Engineering Materials 5 (2003) 5.

[25] R. Song, D. Ponge, D. Raabe, D. K. Matlock, Materials Science and Engineering A 441 (2006) 1.

[26] F.J. Humphreys, M.G. Ardakani, Acta Metallurgica 42 (1994) 749.

[27] P.B. Hirsch, F.J. Humphreys, In: A. Argon, Editor. Physics of strength and plasticity MIT Press (1969) 189.

[28] P. J. Apps, M. Berta, P.B. Prangnell, Acta Materiallia 53 (2005) 499.

[29] M. F. Ashby, Philosophical Magazine 21 (1970) 399.

[30] C. Y. Barlow, N. Hansen, Y.L. Liu, Acta Materiallia 50 (2002) 171.

[31] D. Hull, D. J. Bacon, Introduction to Dislocations. 3rd ed. Oxford: Pergamon Press (1984).

[32] L. S. Toropova, D. G. Eskin, M. L. Kharakterova, T. V. Dobatkina, Advanced Aluminum Alloys Containing Scandium, Gordon (1998).
[33] F. J. Humphreys, M. Hatherly, Recrystallization and Related Annealing Phenomena, Pergamon Press (1995).

Chapter 3

Change in Mechanical Properties during ARB Process of Al-0.2wt%Sc Alloy Having Different Starting Microstructures

Abstract

The mechanical properties of the Al-0.2Sc alloy processed by ARB are investigated in this chapter. The result showed that the hardness monotonously increased in the ST-ARB specimen. On the other hand, the hardness firstly increased by 1-cycle ARB in the Aged-ARB specimens and then decreased in the 300°C Aged-ARB specimen while did not change in the 400°C Aged-ARB specimen. The Aged-ARB specimens showed higher hardness value than that of the ST-ARB specimen. The same tendency was observed in the 0.2% proof stress obtained from tensile test. The mechanical properties obtained experimentally were correlated to the microstructural parameters, such as grain size and dislocation density, based on strengthening mechanisms, i.e., dislocation strengthening, grain boundary strengthening and precipitation strengthening. There was a good agreement between the total strength calculated and the experimentally measured 0.2% proof stress obtained from tensile test.

Keywords: ARB, precipitates, hardness, tensile properties, strengthening mechanisms.

3.1. Introduction

Chapter 2 revealed that the microstructural development during ARB process of the Al-0.2%wt. Sc alloy was greatly affected by the pre-existing of precipitates. Microstructural parameters that have been characterized in Chapter 2, i.e., grain size, fraction of HAGBs, dislocation density and morphology of precipitates, would affect mechanical properties of the materials significantly [1-2]. However, the effect of precipitates on the mechanical properties of materials severely deformed by ARB has not yet been clarified. In this chapter, the mechanical properties (hardness and tensile results) of the ARB processed Al-0.2%wt.Sc alloy having different starting microstructures are examined and correlated to the microstructural parameters obtained in Chapter 2. The strengthening mechanisms to be considered are grain refinement strengthening, dislocation strengthening and precipitation strengthening [3-14].

3.2. Experimental procedure

The material studied in this chapter is the same as that used in Chapter 2. Sheets of the Al-0.2%wt. Sc alloy were solution treated at 903 K (630°C) for 86.4 ks and then immediately water-quenched. The solution treated sheets were aged at 573 K (300°C) or 673 K (400°C) for 10 ks, to obtain different sizes of Al_3Sc precipitates. Three kinds of the specimens, that were solution treated, aged at 300°C or 400°C were severely deformed by the ARB process up to 10 cycles, which corresponds to an equivalent strain of 8.0, at RT with lubrication.

Tensile tests were performed on the Al-0.2 wt.% Sc specimens ARB processed by various cycles to measure their mechanical properties. Tensile tests were carried out using Shimadzu 100 KN tensile machine at an initial strain rate of 8.3×10^{-3} s^{-1} at room temperature. The specimens have a gage length of 10 mm and gage width of 5 mm and thickness of 1 mm.

Shimadzu HMW micro hardness tester was also used for Vickers hardness measurements on the rolling planes of the sheets using a load of 0.098 kgf and a loading period of 10 s at room temperature. X-ray diffraction (XRD) measurements were performed using a Philips X'pert diffractometer in order to measure the volume fraction of Al_3Sc precipitates in the specimens. Microstructural parameters of the ARB processed specimens, which have been obtained in Chapter 2, were used for discussing the strengthening mechanisms of the materials.

3.3. Results

3.3.1. Change in mechanical properties during ARB process

Figure 3.1 shows Vickers hardness of the ST-ARB and Aged-ARB specimens as a function of the number of ARB cycle. The Vickers hardness of the ST-, 300°C Aged- and 400°C Aged-specimens before ARB process (0-cycle of ARB) is 23HV, 70HV and 40HV, respectively. The difference of hardness between the ST- and Aged- specimens is due to the existence of Al_3Sc precipitates which inhibit dislocation motion and harden the materials. In addition, the stress fields around coherent precipitates can increase the hardness. The finer precipitates in the 300°C Aged-specimen causes higher hardness value than in the 400°C Aged-specimen at 0-cycle of ARB. Vickers hardness of the ST-ARB specimen monotonously increases with increasing the number of ARB cycles and reaches to 52 HV after 10-cycle ARB process. It is a typical behavior of the most ARB processed materials previously studied [15-18]. The hardness of the 400°C Aged-ARB specimen drastically increases to approximately 60 HV by 1-cycle ARB, but it does not change with further increase of ARB cycle. On the other hand, Vickers hardness of the 300°C Aged-ARB specimen increases to 78HV by 1-cycle ARB, however, it monotonously decreases with further increase of ARB cycle and reaches to 52 HV after 10-cycle ARB process. The hardness decrease during the ARB process is a quite unique behavior, which has not yet been reported previously. It is noteworthy that the hardness of the Aged-ARB specimens is always higher than that of the ST-ARB specimen. These results indicate that the changes in mechanical behavior of the Aged-ARB specimens are completely different from that in the ST-ARB specimen, due to the presence of pre-existing precipitates. It should be noted, however, that after 10-cycle ARB the hardness of three kinds of specimens is not so much different to each other.

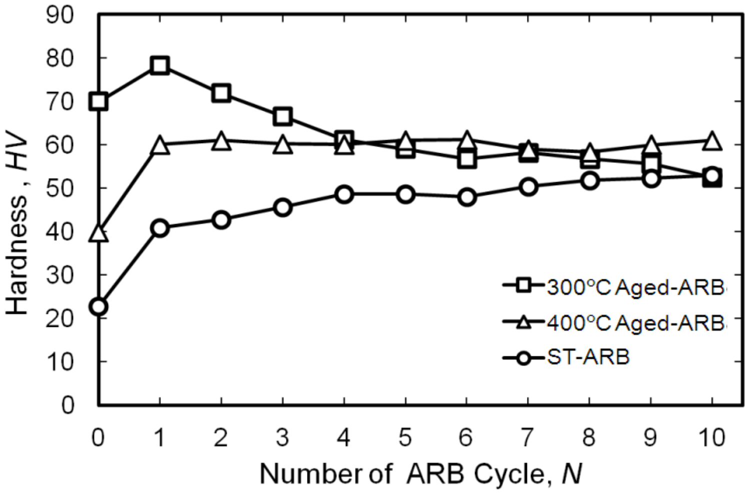

Fig. 3.1. Vickers hardness of the ST-ARB, 300°C Aged-ARB and 400°C Aged-ARB specimens processed by various cycles of ARB.

Stress-strain curves of the ARB processed specimens obtained from the tensile test are given in **Fig. 3.2**. It is shown that ST-ARB and Aged-ARB specimens have different tendency in the change of mechanical properties during ARB process. In the ST-ARB specimen (Fig. 3.2(a)), the flow stress increases with increasing the number of ARB cycles. The tensile elongation of the ST-ARB specimen obviously decreases, though the total elongation of the ST-ARB specimens increases with increasing the ARB cycles after 3-cycle ARB. The change in stress-strain behaviors of the ST-ARB specimens is similar to that of the ARB processed pure aluminum previously reported [19-21]. However, the flow stress of the 300°C Aged-ARB specimen increases by 1-cycle ARB and then decreases with further increase of the ARB cycles (Fig. 3.2 (b)). On the other hand, it seems in Fig. 3.2 (c) that the flow stress of the 400°C Aged-ARB specimen does not significantly change between 1-cycle and 10-cycle ARB. It should be noted that tensile elongation obviously decreases by ARB in the Aged-ARB specimens.

The 0.2% proof stress, tensile strength, uniform elongation and total elongation of the specimens are summarized as a function of the number of ARB cycles in **Fig. 3.3**. As shown in Fig. 3.3 (a), the proof stress of the Aged-ARB specimens is higher than that of the ST-ARB specimen at 0 cycle of ARB, which corresponds with the difference in hardness (Fig. 3.1). It is found that the proof stress of the ST-ARB specimen monotonously increases with increasing the number of ARB cycle. On the other hand, the proof stress of the 300°C Aged-ARB specimen increases by 1-cycle of ARB and then decreases gradually with increasing the ARB cycle. The proof stress of the 400°C Aged-ARB specimen increases slightly by 1-cycle of ARB and then keeps a constant value up to 10-cycle of ARB. The change in the tensile strength with increase of ARB cycle in the ST-ARB specimen and Aged-ARB specimens is almost the same as that in the proof stress (Fig. 3.3 (b)). These results correspond well with the change in hardness during the ARB process (Fig. 3.1).

Uniform and total elongation is shown as a function of the number of ARB cycle in Fig. 3.3 (c) and (d), respectively. At 0-cycle of ARB, the uniform elongation and total elongation of the ST-specimen are much larger than those of the Aged-specimens. This indicates pre-existing precipitates inhibit tensile elongation. By 1-cycle of ARB, the elongation of the ST-ARB specimen significantly decreases, i.e., the uniform elongation of the ST-ARB specimen decreases from 50% to less than 1%, and the total elongation decreases from 80% to 13%. The elongation of the Aged-ARB specimens also decreases by 1-cycle of ARB. However, the change in elongation of the Aged-ARB specimens is smaller than that in the ST-ARB specimen. Above 3-cycle, the uniform elongation of the ST-ARB specimen increases gradually with increasing number of the ARB cycles, and the total elongation of the ST-ARB specimen shows nearly a constant value. On the other hand, the uniform elongation of the Aged-ARB specimens keeps nearly a constant value. Total elongation of the Aged-ARB specimens exhibits similar value to the ST-ARB specimen.

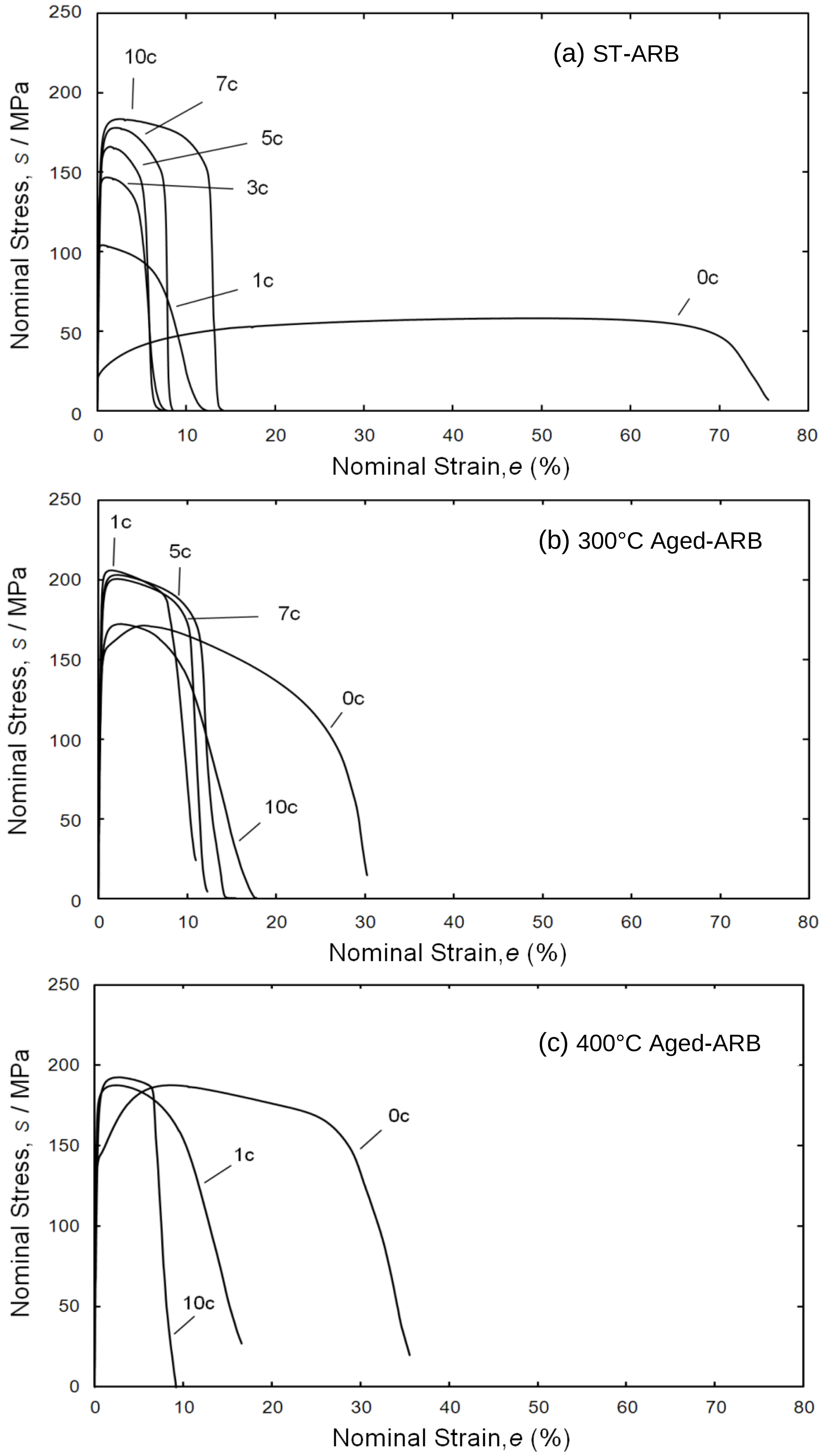

Fig. 3.2. Tensile stress-strain curves of the (a) ST-ARB specimen, (b) 300°C Aged-ARB specimen and (c) 400°C Aged-ARB specimen.

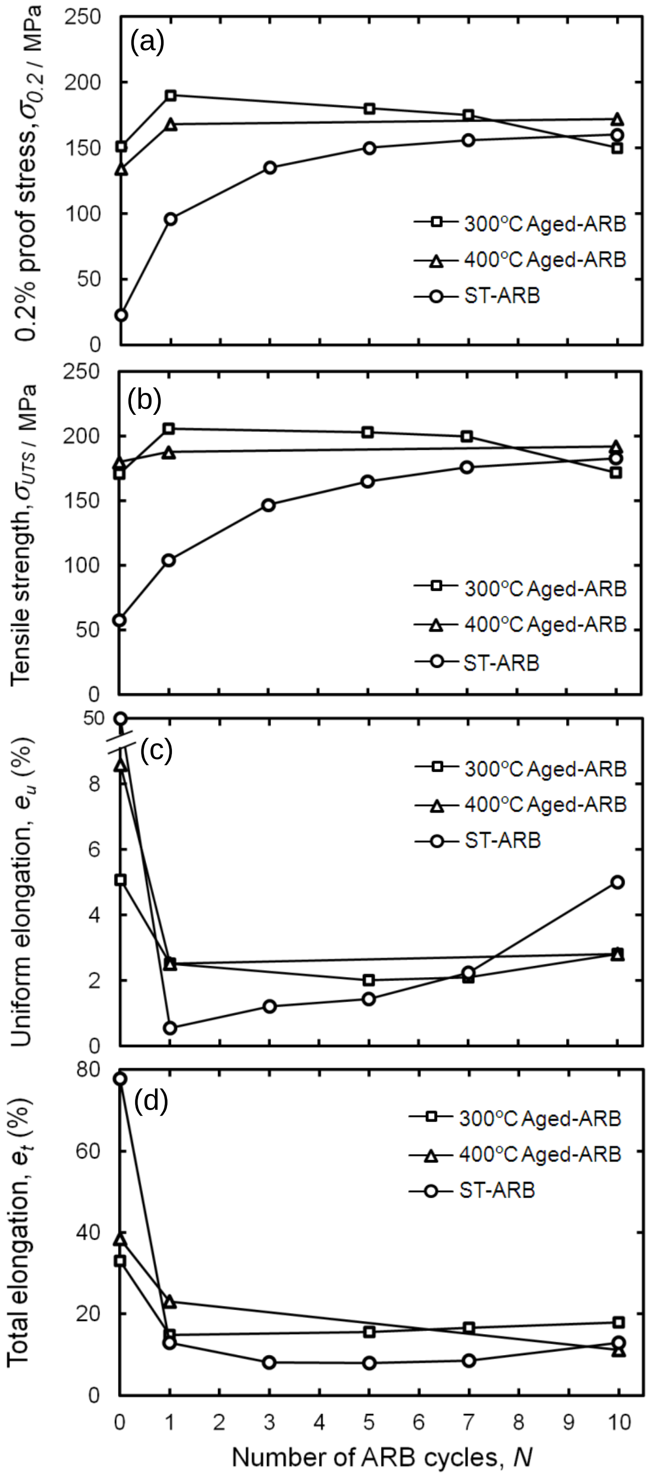

Fig. 3.3. (a) 0.2% proof stress, (b) tensile strength, (c) uniform elongation and (d) total elongation of the ST-ARB specimen, 300°C Aged-ARB specimen and 400°C Aged-ARB specimen.

3.4. Discussion: Correlation between mechanical properties and microstructural parameters

The increase in strength and decrease in elongation are typical changes in mechanical properties of metals during SPD, which seems to occur regardless of the kinds of SPD processes and metals. This characteristic change in the mechanical properties depends on the starting microstructures. The proof stress of the Aged-ARB specimens containing pre-existing precipitates increases by 1-cycle ARB, but it decreases in the 300°C Aged-ARB specimen or it does not change in the 400°C Aged-ARB specimen with further increase of ARB cycle. In addition, the elongation of the Aged-ARB specimens does not change with increasing the ARB cycle over 3 cycles. Accordingly, it is important to relate the mechanical properties of the Aged-ARB specimens containing pre-existing precipitates to the structural parameters, such as dislocation density, grain size of the matrix, volume fraction and size of the precipitates, and to compare the result with that of the ST-ARB specimen. Three kinds of strengthening mechanisms in the ST-ARB specimen and Aged-ARB specimens, i.e., grain boundary strengthening, dislocation strengthening and precipitation strengthening, are discussed in the following sections, based on the experimental results obtained in Chapter 2 and Chapter 3.

3.4.1. Effect of grain size on mechanical properties

Grain size is one of the important parameters that control mechanical properties of polycrystalline metals [22-24]. Hall-Petch relationship has been well known in polycrystalline metals, as is shown in the following equation [8].

$$\sigma_y = \sigma_0 + k \cdot d^{-1/2} \qquad (3.1)$$

where σ_y is the proof stress, σ_0 is a friction stress (constant), *d* is the mean grain size and *k* is a constant.

Figure 3.4 shows the average grain size (HAGBs interval along ND, d_t) of the ST-ARB and Aged-ARB specimens as a function of the number of ARB cycle. The value of grain size is also shown in **Table 3.1**. Figure 3.4 and Table 3.1 clearly indicate that the grain size decreases with increasing the number of the ARB cycle in all specimens. After 10-cycle ARB, the d_t of the ST-ARB, 300°C Aged-ARB and 400°C Aged-ARB specimens reaches to d_t=0.37μm, d_t=0.24μm and d_t=0.27 μm, respectively.

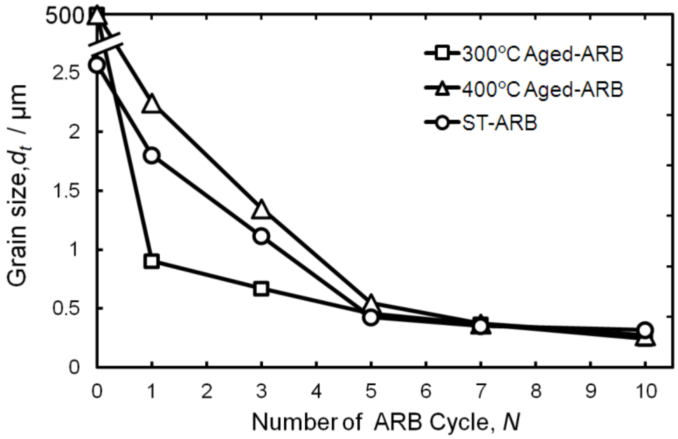

Fig. 3.4. Change in grain size as a function of the number of ARB cycle.

Table 3.1. Grain size after various ARB cycles.

	Grain size, d_t (μm)		
ARB cycles	ST-ARB	300°c Aged-ARB	400°c Aged- ARB
0	500	500	500
1	2.1	0.90	2.3
3	1.3	0.66	1.4
5	0.5	0.45	0.54
7	0.41	0.36	0.37
10	0.37	0.24	0.27

The increase in the proof stress due to grain refinement, $\Delta\sigma_{gb}$(=$kd_t^{-1/2}$), obtained from the Hall-Petch relationship is shown in **Fig. 3.5**. The constant value of *k*=44 (MPa·$m^{1/2}$) for pure aluminum reported by Hansen *et al.* [25] is used for the calculation. As shown in this figure, the grain refinement strengthening value gradually increases with increasing the number of the ARB cycles. Compared to the ST-ARB specimen, the grain refinement is accelerated especially in the 300°C Aged-ARB specimens due to fine precipitates, as discussed in Chapter 2. Therefore, the grain refinement strengthening value in the 300°C Aged-ARB specimens is larger than that in other specimens, as shown in Fig. 3.5. On the other hand, the grain refinement strengthening value in the 400°C Aged-ARB specimens is nearly the same as that in the ST-ARB specimen, although slight difference can be seen after 5-cycle of ARB.

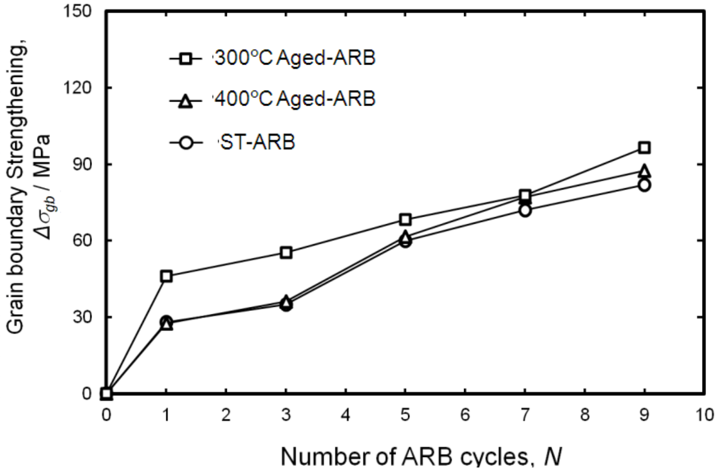

Fig. 3.5. The grain refinement strengthening value of the ST-ARB specimen, 300°C Aged-ARB specimen and 400°C Aged-ARB specimen as a function of the number of ARB cycles.

3.4.2. Effect of dislocation density on mechanical properties

The effect of precipitates on dislocation generation and accumulation was already discussed in the section 2.4 in Chapter 2. To measure the dislocation density, X-ray diffraction (XRD) measurements were performed and the obtained results were analyzed using Williamson-Hall method [26]. **Figure 3.6** shows XRD profiles of the (a) ST-ARB specimen, (b) 300°C Aged-ARB specimen and (c) 400°C Aged-ARB specimen. In the Williamson–Hall (WH) method, the width of the half maximum of peak, *β*, is related to the lattice strain, *ε*, through the following equation:

$$\beta\frac{\cos\theta}{\lambda} = \frac{0.9}{D} + \varepsilon\ \frac{2\sin\theta}{\lambda} \tag{3.2}$$

where *θ* , *λ* , and *D* are the diffraction angle, X-ray wavelength, and crystallite size, respectively. The *β* for each (hkl) peak are obtained from Fig. 3.6. By plotting the value of $\beta\ \frac{\cos\theta}{\lambda}$ as a function of $\frac{2\sin\theta}{\lambda}$, the value of the lattice strain, *ε*, and crystallite size, *D*, can be obtained from the slop and y-axis interception, respectively. The dislocation density, *ρ*, is derived from the equation:

$$\rho= 14.4\ \frac{\varepsilon^2}{b^2} \tag{3.3}$$

where *b* is the magnitude of the Burgers vector. The calculated value of the dislocation density in the ST-ARB specimen and Aged-ARB specimens with various ARB cycles are shown in **Table 3.2**. **Figurer 3.7** shows the change in dislocation density of the ST-ARB specimen and Aged-ARB specimens as a function of the ARB cycle. It is assumed that the starting specimens (0-cycle specimen) have very low dislocation density probably in the order of 10^{10} m^{-2}, since they have coarse and fully-recrystallized grain structures.

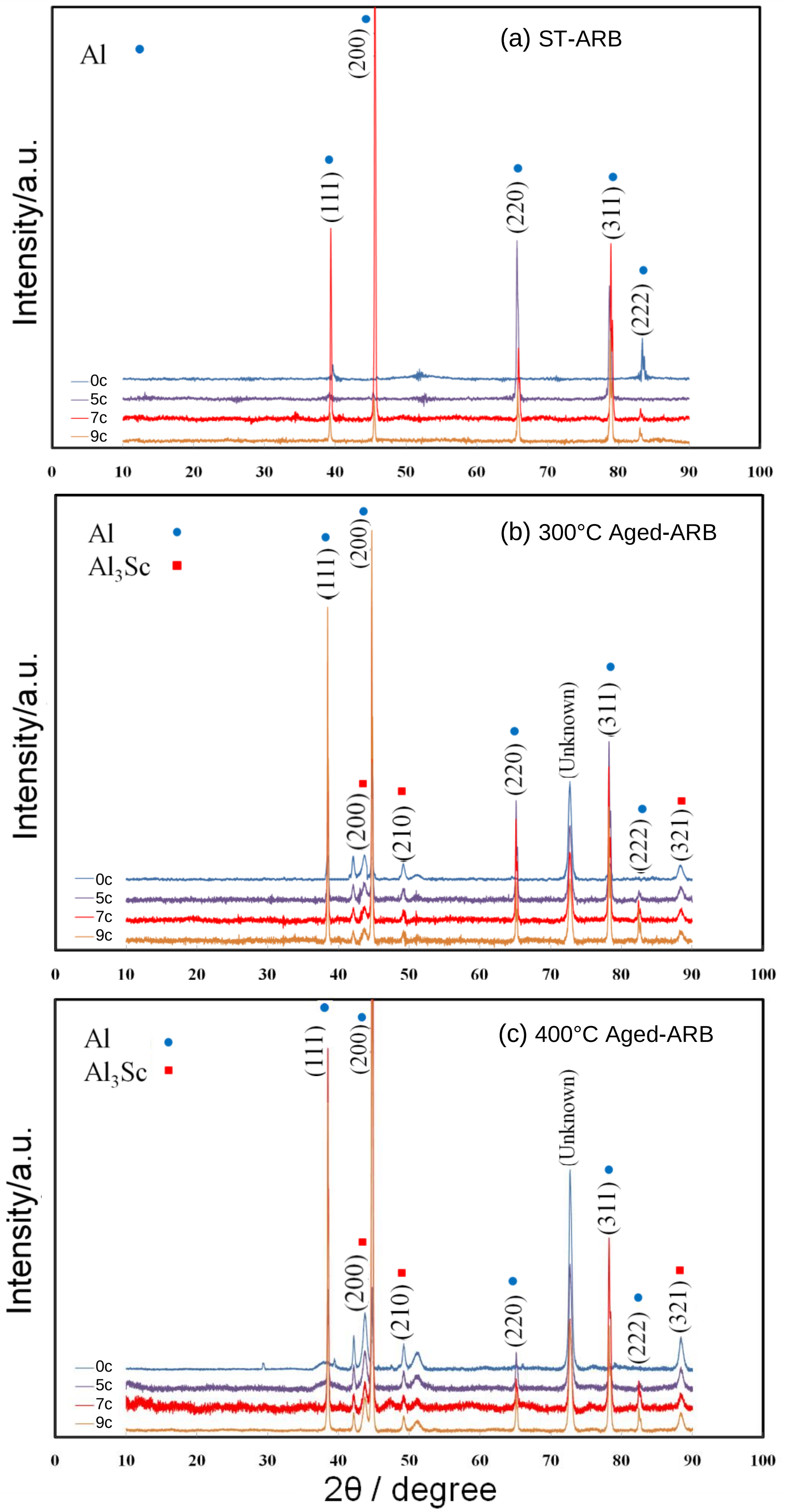

Fig. 3.6. XRD patterns of the (a) ST-ARB, (b) 300°C Aged-ARB and (c) 400°C Aged-ARB specimens.

Table 3.2. Values of dislocation density in the ST-ARB specimen, 300°C Aged-ARB specimen and 400°C Aged-ARB specimen after various cycles of ARB.

	Dislocation density, ρ / m^{-2}		
ARB cycles	ST-ARB	300°C Aged-ARB	400°C Aged- ARB
0	$\sim 10^{10}$	$\sim 10^{10}$	$\sim 10^{10}$
1	3.8×10^{14}	1.85×10^{15}	8.91×10^{14}
3	3.49×10^{14}	6.35×10^{14}	1.42×10^{15}
5	8.1×10^{13}	2.32×10^{14}	1.14×10^{15}
7	2.0×10^{13}	1.58×10^{14}	4.50×10^{14}
9	4.75×10^{12}	1.15×10^{13}	5.32×10^{13}

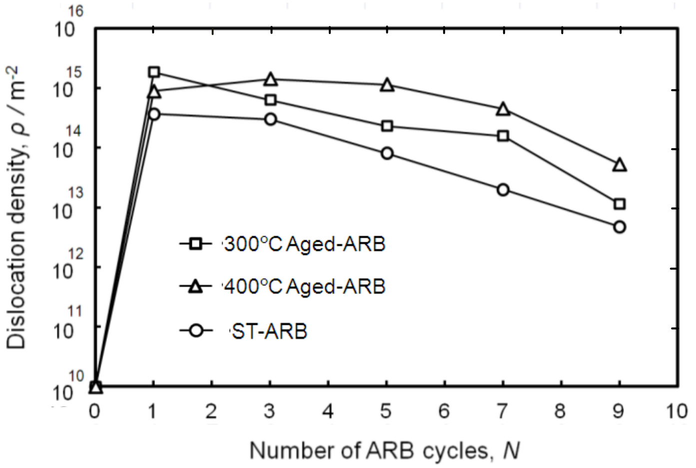

Fig. 3.7. Dislocation density of the ST-ARB specimen, 300°C Aged-ARB specimen and 400°C Aged-ARB specimen as a function of ARB cycles.

Figure 3.7 indicates that dislocation density of the ST-ARB specimen and 300°C Aged-ARB specimen greatly increases from 10^{10} m^{-2} at 0-cycle ARB to 3.8×10^{14} m^{-2} and 1.9×10^{15} m^{-2} by 1-cycle ARB, respectively, and then decreases with further increase of the ARB cycle. On the other hand, dislocation density of the 400°C Aged-ARB specimen increases to 1.42×10^{15} m^{-2} by 3-cycle ARB and then decreases. The decrease in dislocation density during ARB in pure Al has been also reported by Huang *et al.* [27] and Miyajima *et al.*[28]. It should be noted that the dislocation density of the Aged-ARB specimens is always higher than that of the ST-ARB specimen.

The increase in the shear strength due to dislocation strengthening (strain hardening) can be expressed by the following Bairly-Hirsch equation:

$$\Delta\sigma_\rho = \alpha G b \rho^{1/2} \tag{3.4}$$

where α is a constant, b is the magnitude of Burgers vector, G is the shear modulus, and ρ is the dislocation density. The $\alpha = 0.3$, $b = 0.286$ nm and $G = 25.4$ GPa in Al [29] are considered in this chapter. The change in dislocation strengthening calculated from the equation (3.4) is plotted as a function of ARB cycle in **Fig. 3.8**. The dislocation strengthening value of the ST-ARB and 300°C Aged-ARB specimen increases by 1-cycle of ARB, but they monotonously decrease with increasing the ARB cycles. On the other hand, the value in the 400°C Aged-ARB specimen increases up to 3-cycle ARB and then decreases. After 3-cycle ARB, the dislocation strengthening value of the 400°C Aged-ARB specimen is higher than those of the 300°C Aged-ARB and ST-ARB specimens. It can be said that the dislocation strengthening in the Aged-ARB specimens is higher than that in the ST-ARB specimen.

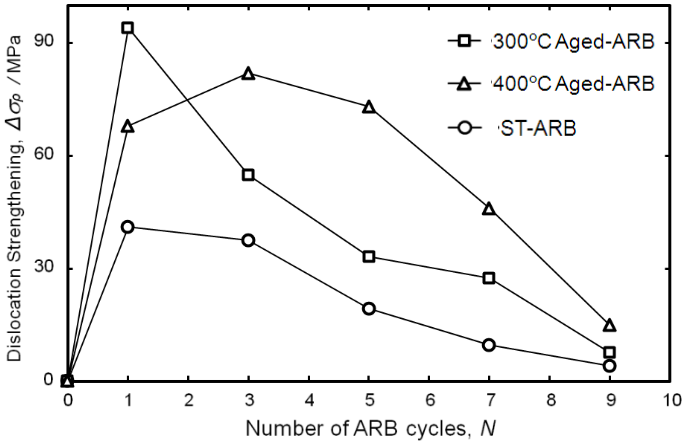

Fig. 3.8. The dislocation strengthening value of the ST-ARB specimen, 300°C Aged-ARB specimen and 400°C Aged-ARB specimen as a function of ARB cycles.

3.4.3. Effect of precipitates on mechanical properties

The Aged-ARB specimens have pre-existing precipitates before the ARB. As shown in Figs. 3.1 and 3.3 (b), the hardness and proof stress of the Aged-ARB specimens at 0-cycle of ARB are much higher than that of the ST-ARB specimen, which indicates that the pre-existing precipitates strengthen the materials.

Two kinds of deformation mechanism in materials containing particles have been proposed: (I) Cut-through mechanism for small and relatively weak precipitates and (II) Orowan mechanism for large and hard particles. In case of small precipitates, dislocations cut through the precipitates. However, dislocation can not cut large or hard particles. In this case, dislocation passes through the precipitates by leaving a loop around the precipitates. This interaction is known as the Orowan mechanism. **Figure 3.9** schematically shows the change in dominant mechanism with changing particle size. Precipitation strengthening, $\Delta\sigma_{ppt}$, depends on the radius of the precipitates (R). As shown in Fig. 3.9, there is a critical radius of Al_3Sc in Al-0.2Sc alloy, above which the dominant process changes from cut-through mechanism to Orowan mechanism. Seidman *et al.* [1] reported that the critical radius in case of Al_3Sc is 2.1 nm. Accordingly, the cut-through mechanism should work in the 300°C Aged-ARB specimen while Orowan mechanism should work in the 400°C Aged-ARB specimen at least at the early stage of deformation, because the precipitates size of the 300°C Aged-ARB specimen and 400°C Aged-ARB specimen is 1.81 nm and 25 nm, respectively, as shown in Fig. 2.1 (b) and (c).

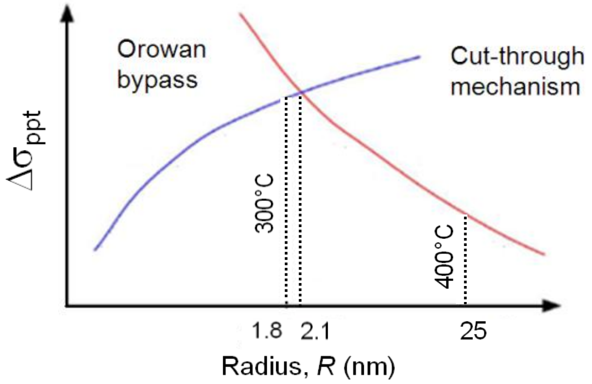

Fig. 3.9. Schematic illustration of precipitation strengthening ($\Delta\sigma_{ppt}$) as a function of particle radius.

Concerning the cut-through mechanism, elastic-field interactions between coherent precipitate and dislocation affects the strengthening [28, 29]. The increase in strength by cut-through mechanism,$\Delta\sigma_{cs}$, is given by the equation shown below:

$$\Delta\sigma_{cs} = A\cdot(G\varepsilon)^{3/2}\left(\frac{rf}{0.18Gb^2}\right)^{1/2} \tag{3.5}$$

where *A* is a constant, ε is the misfit strain ($\varepsilon \approx (2/3)\delta$; $\delta = \Delta a/a$ where *a* is the lattice parameter of precipitate and Δa is difference in lattice parameter between matrix and precipitate), *G* is the shear modulus, *r* is the mean radius of precipitates, *f* is the volume fraction of precipitates, and *b* is the magnitude of Burgers vector of the matrix.

The strengthening by Orowan mechanism, $\Delta\sigma_{or}$, is expressed as [29, 30]:

$$\Delta\sigma_{or} = \frac{0.4Gb}{\pi\sqrt{1-\nu}}\frac{\ln\left(\frac{2r}{b}\right)}{\lambda} \tag{3.6}$$

$$\lambda = \left[\left(\frac{3\pi}{4f}\right)^{1/2} - 1.64\right]r \tag{3.7}$$

where v is Poisson's ratio and λ is the inter-particle spacing expressed as a function of volume fraction of particles [31-32].

As can be seen in equations (3.5) and (3.7), the size and volume fraction of precipitates are necessary for calculating the precipitation strengthening. The sizes of precipitates obtained from TEM micrographs are described in Chapter 2. The size of Al_3Sc in the 300°C Aged-ARB specimen and 400°C Aged-ARB specimen is shown in **Table 3.3**. It should be noted that the size of precipitates in 3 cycles, 5 cycles and 7 cycles is assumed to be the same as that in the 9 cycles observed. In order to obtain the volume fraction of the Al_3Sc particles, XRD results were used. XRD results (Fig. 3.6) clearly show that there are certain fractions of Al_3Sc precipitates in the Aged-ARB specimens. The volume fraction of precipitates, $f_{\mathrm{Al_3Sc}}$, can be estimated from the ratio of the integrated intensities of the diffraction peaks corresponding to precipitates to the sum of the whole integrated intensities of the diffraction peaks corresponding to the matrix and precipitates [33-35]. The volume fraction of Al_3Sc particles in the 300°C Aged-ARB specimen and 400°C Aged-ARB specimen was calculated by equation (3.8) and the results is shown in **Table 3.4**.

$$f_{\mathrm{Al_3Sc}} = \left[\left(\frac{\Sigma I_{\mathrm{Al_3Sc}}}{\Sigma I_{\mathrm{Al}} + \Sigma I_{\mathrm{Al_3Sc}}} \right) \right] \tag{3.8}$$

where $I_{\mathrm{Al_3Sc}}$ and I_{Al} correspond to integrated intensity of Al_3Sc precipitates and Al matrix, respectively. It should be noted that the volume fraction at 0-cycle ARB obtained from XRD (0.53%) agrees well with the volume fraction obtained from the phase diagram (0.48%), although the slight difference is observed. The change in volume fraction of the Al_3Sc in the

300°C Aged-ARB specimen and 400°C Aged-ARB specimen is shown in **Fig. 3.10**. Figure 3.10 indicates that the volume fraction of Al_3Sc monotonously decreases with increasing the number of the ARB cycles, indicating that in both 300°C Aged-ARB specimen and 400°C Aged-ARB specimen pre-existing precipitates are dissolved during ARB process. The strengthening by precipitates in the Aged-ARB specimens calculated using Eqs. (3.5), (3.6) and (3.7) are plotted in **Fig. 3.11**. As can be seen, the strength due to precipitation decreases with increasing the number of ARB cycles. It is noteworthy that precipitation strengthening in the 300°C Aged-ARB specimens containing small precipitates is higher than that in the 400°C Aged-ARB specimen containing large precipitates, but the difference becomes smaller at higher ARB cycles.

Table 3.3. Size of Al_3Sc precipitates in the 300°C Aged-ARB specimen and 400°C Aged-ARB specimen as a function of ARB cycles.

	Size of Precipitates (radius), r (nm)	
ARB cycles	300°C Aged-ARB	400°C Aged-ARB
0	1.8 (observed)	25 (observed)
1	2 (observed)	5 (observed)
3	~2	~ 5
5	~2	~ 5
7	~2	~ 5
9	2 (observed)	5 (observed)

Table 3.4. Volume fraction of Al_3Sc precipitates in the 300°C Aged-ARB specimen and 400°C Aged-ARB specimen as a function of ARB cycles.

	Volume fraction of Precipitates, f_{Al_3Sc} (%)	
ARB cycles	300°C Aged-ARB	400°C Aged-ARB
0	0.53	0.75
1	0.49	0.69
3	0.35	0.41
5	0.28	0.33
7	0.22	0.29
9	0.16	0.20

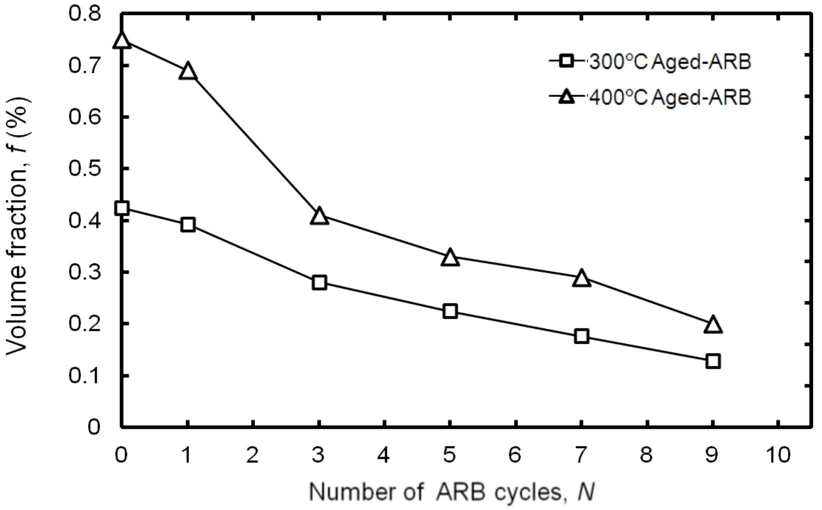

Fig. 3.10. Change in volume fraction of Al_3Sc precipitates in the 300°C Aged-ARB specimen and 400°C Aged-ARB specimen as a function of ARB cycle.

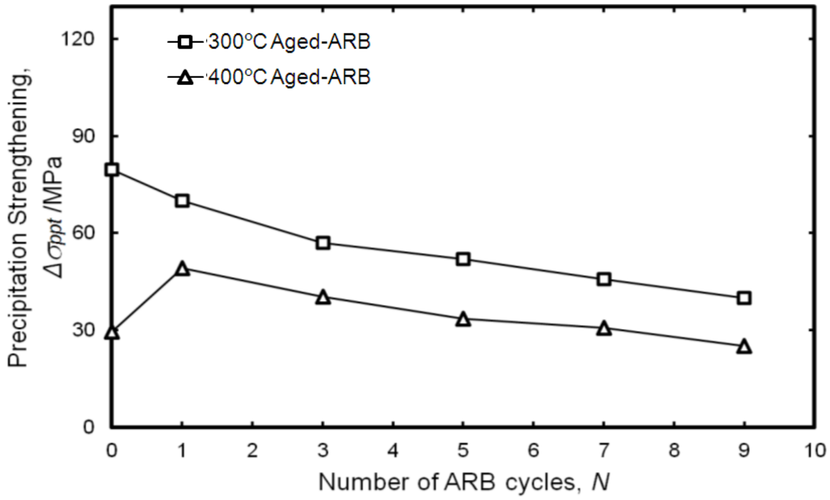

Fig. 3.11. Precipitation strengthening value of the 300°C Aged-ARB specimen and 400°C Aged-ARB specimen as a function of ARB cycles.

It is also interesting that in the 300°C Aged-ARB specimens, precipitation strengthening decreases monotonously with increasing the ARB cycle, whereas precipitation strengthening in the 400°C Aged-ARB specimens increases after 1-cycle ARB and then decreases with further ARB cycles. This phenomenon corresponds to the significant decrease in the size of precipitates after 1-cycle ARB in the 400°C Aged-ARB specimen (Table 3.3).

3.4.4. Overall strength through correlating the strengthening mechanisms

The strengthening through three kinds of mechanisms, i.e., grain boundary strengthening, dislocation strengthening and precipitation strengthening, were already calculated in sections 3.4.1 and 3.4.2. When the total strength is assumed to be expressed as the summation of the strengthening mechanisms, it can be expressed in a following form [36, 27-41].

$$\sigma_{0.2}= \sigma_0+ \sigma_{ss}+\Delta\sigma_{gb}+ \Delta \sigma_\rho+ \Delta \sigma_{ppt} \tag{3.9}$$

where σ_0 is the friction stress and σ_{ss} is solid solution strengthening. The σ_0 = 9.7 MPa is used in this chapter which was taken from the data in pure Al reported by Kamikawa *et al.* [42]. The σ_{ss} = 20 MPa which is obtained from 0.2 proof stress (Fig. 3.3 (a)) at 0-cycle in the solution treated specimen. The values of $\Delta\sigma_{gb}$, $\Delta\sigma_\rho$ and $\Delta\sigma_{ppt}$ are obtained from Figs. 3.5, 3.8 and 3.11, respectively. The calculated results are plotted in **Fig. 3.12**. The 0.2% proof stress of the materials obtained experimentally (Fig. 3.3 (a)) is also shown in this figure.

The total strength and experimental strength in the ST-ARB specimen are shown in Fig. 3.12 (a). As shown in this figure, the total strength calculated from the microstructural parameters gradually increases with increasing the ARB cycle. The same tendency is also observed in the experimental strength, though the value is somewhat different from the total strength calculated. It should be noted that there are two strengthening mechanisms in the ST-ARB specimen, i.e., grain refinement strengthening and dislocation strengthening, which affect on the mechanical properties. It was shown that dislocation strengthening decreases (Fig. 3.8) while grain refinement strengthening increases (Fig. 3.5) with increasing the ARB cycle. However, the increase in the total strength indicates that the grain refinement is more effective on strengthening of the ST-ARB specimen than that of dislocation strengthening [18, 43].

Figure 3.12 (b) and (c) show the total strength and experimental strength in the 300°C Aged-ARB specimen and 400°C Aged-ARB specimen, respectively. The totally different tendency from the ST-ARB specimen is observed in the Aged-ARB specimens. As can be seen, the total strength calculated in the 300°C Aged-ARB specimen firstly increases by 1-cycle ARB and then decreases with further increasing the ARB cycle. On the other hand, in the 400°C Aged-ARB specimen the total strength calculated firstly increases by 1-cycle ARB and then keeps approximately the same value up to 10-cycle ARB. The tendency of the experimental strength is almost the same as that of the total strength calculated in these specimens.

It has been already shown that the precipitation strengthening (Fig. 3.11) and dislocation strengthening (Fig. 3.8) decreases with increasing the number of ARB cycles in the Aged-ARB specimens. It is also shown that grain refinement strengthening increases during ARB process in the Aged-ARB specimens (Fig. 3.5). However, in the 300°C Aged ARB specimens all strengthening mechanisms are shown to produce an overall decrease in the total strength between 1-cycle and 10-cycle. The decrease in the total strength in the 300°C Aged-ARB specimen during ARB process implies a dominant contribution of precipitation strengthening and dislocation strengthening, relative to grain refinement strengthening.

On the other hand, in the 400°C Aged-ARB specimen, the greater amount of dislocation strengthening is observed compared with the 300°C Aged-ARB specimen (Fig. 3.8). Furthermore, precipitation strengthening is lower in the 400°C Aged-ARB specimen than that in the 300°C Aged-ARB specimen (Fig. 3.11), indicating smaller effect of precipitation hardening on the total strength in the 400°C Aged-ARB specimen compared with the 300°C Aged-ARB specimen. It is also shown that a decrease in particle size in the 400°C Aged-ARB specimen is appeared by 1-cycle ARB, as was shown in Table 3.3. This reduction in particle size has a positive effect to increase precipitation strengthening in the 400°C Aged-ARB specimen, whereas in the 300°C Aged-ARB specimen precipitation strengthening decreases monotonously during ARB processing, as shown in Fig. 3.11. These behaviors result in different contribution of each strengthening mechanisms to total strength in the 400°C Aged-ARB specimen compared with the 300°C Aged-ARB specimens. Eventually, in the 400°C Aged-ARB specimen, all strengthening phenomena mentioned above balance during ARB process, exhibiting no significant decrease or increase in the total strength after 1-cycle ARB to 10-cycle ARB.

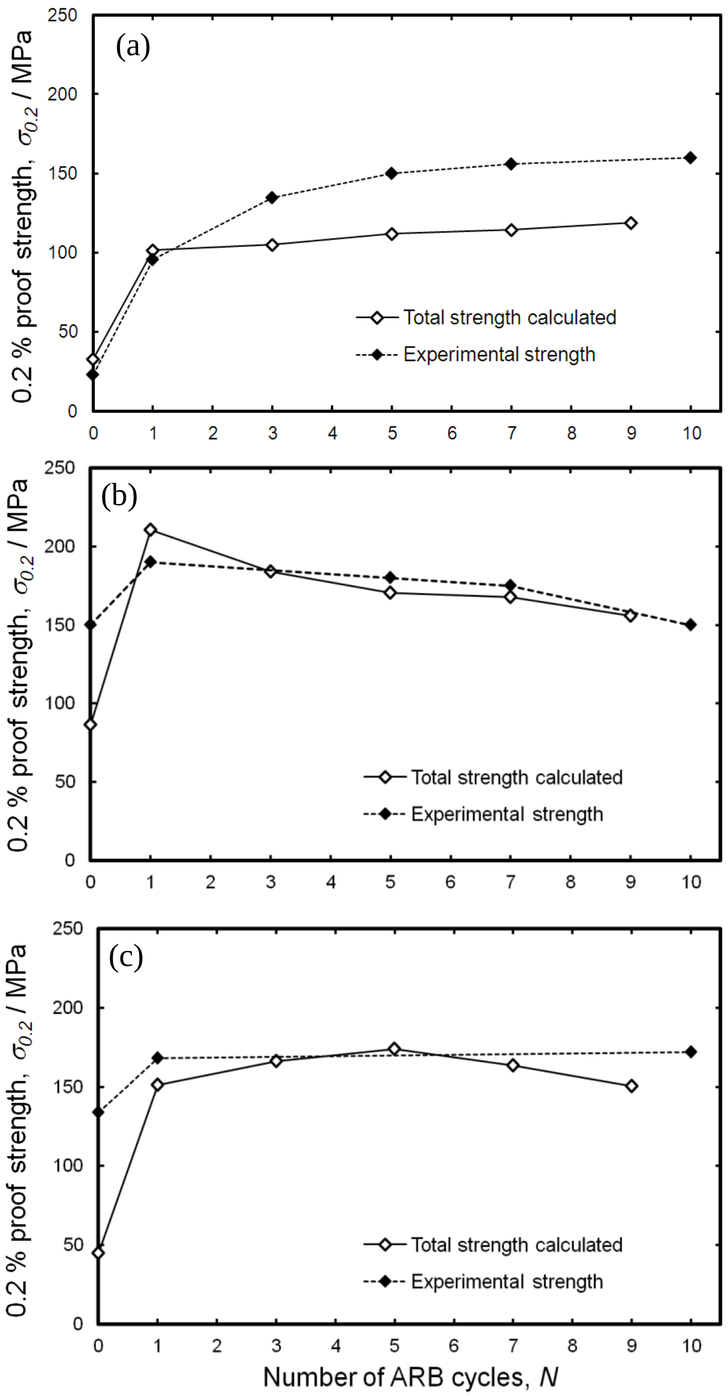

Fig. 3.12. The total strength calculated and experimental strength in the (a) ST-ARB, (b) 300°C Aged-ARB and (c) 400°C Aged-ARB specimens

The calculated total strength in the SeT-ARB specimen, 300°C Aged-ARB specimen and 400°C Aged-ARB specimen are summarized in **Fig. 3.13**. As can be seen, the tendency of the total strength corresponds well to the proof stress and hardness values experimentally obtained in Fig. 3.3 (a) and Fig. 3.1, respectively.

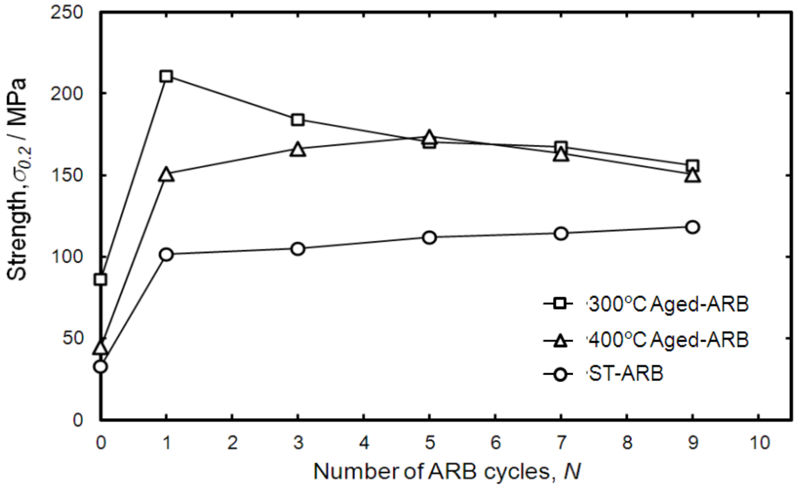

Fig. 3.13. The total strength calculated from the microstructural parameters in the ST-ARB, 300°C Aged-ARB specimen and 400°C Aged-ARB specimen.

3.5. Conclusions

The mechanical properties of three kinds of specimens, i.e., ST-ARB, 300°C Aged-ARB and 400°C Aged-ARB, were studied in this chapter and following conclusions can be made:

(1) Vickers hardness of the ST-ARB specimen monotonously increased with increasing the number of ARB cycles. On the other hand, Vickers hardness of the 300°C Aged-ARB specimen increased by 1-cycle ARB, and then monotonously decreased with further increase of ARB cycle. The hardness of the 400°C Aged-ARB specimen increased by 1-cycle ARB, but it did not change with further increase of ARB cycle. The same tendency was observed in the 0.2% proof stress obtained from tensile test.

(2) The mechanical properties of the ST-ARB and Aged-ARB specimens related to the structural parameters, such as dislocation density, grain size of the matrix, volume fraction and size of the precipitates, based on strengthening mechanisms, i.e., grain boundary strengthening, dislocation strengthening and precipitation strengthening. The grain refinement strengthening increased with increasing the number of ARB cycles in all specimens, although some differences were observed in the ST-ARB and Aged-ARB specimens. The dislocation strengthening value of the ST-ARB and 300°C Aged-ARB specimens increased by 1-cycle ARB, but they monotonously decreased with further increase of the ARB cycles. On the other hand, that value in the 400°C Aged-ARB specimen increased up to 3-cycle ARB and then decreased. The precipitation strengthening gradually decreased in the 300°C Aged-ARB specimen, whereas precipitation strengthening in the 400°C Aged-ARB specimen firstly increased by 1-cycle ARB and then decreased.

(3) There was a good agreement between the tendency of the total strength calculated from the microstructural parameters, and that of the experimentally measured values of 0.2% proof stress obtained from tensile test.

References

[1] D. N. Seidman, E. A. Marquis, D. C. Dunand, Acta Materialia 50 (2002) 4021.
[2] V. Jindal, P. K. De, K. Venkateswarlu, Materials Letters 60 (2006) 3373.
[3] A. K. Gupta, D. J. Lloyd, S. A. Court, Materials Science and Engineering A316 (2001) 11.
[4] F. Fazeli, W. J. Poole, C.W. Sinclair, Acta Materialia 56 (2008) 1909.
[5] P. J. Apps, M. Berta, P. B. Prangnell, Acta Materialia 53 (2005) 499.
[6] B. Q. Han, E. J. Lavernia, Advanced Engineering Materials 7 (2005) 457.
[7] B. K. Min, H.W. Kim, S. B. Kang, Journal of Materials Processing Technology 162 (2005) 355.
[8] X. Huang, N. Kamikawa, N. Hansen, Materials Science and Engineering A 483-484 (2008) 102.
[9] G. M. Novotny, A. J. Ardell, Materials Science and Engineering A318 (2001) 144.
[10] C. B. Fuller, D. N. Seidman, D.C. Dunand, Acta Materialia 51 (2003) 4803.
[11] R. A. Karnesky, L. Meng, D. C. Dunand, Acta Materialia 55 (2007) 1299.
[12] D. N. Seidman, E. A. Marquis, D. C. Dunand, Acta Materialia 50 (2002) 4021.
[13] B. K. Min, H.W. Kim, S. B. Kang, Materials Processing Technology 162-163 (2005) 355.
[14] E. A. Marquis and D. N. Seidman, Acta Materialia 49 (2001) 1909.
[15] N. A. Smirnova, V.I. Levit, V.I. Pilyugin, R.I. Kuznetsov, L.S. Davydova and V.A. Sazonova, Physical Metallurgy Metalls 61 (1986) 127.
[16] N. Tsuji, Y. Saito, S. H. Lee, and Y. Minamino, Advanced Engineering Materials 5 (2003) 338.
[17] Y. Saito, H. Utsunomiya, N. Tsuji, T. Sakai, Acta Materialia 47 (1999) 579.
[18] N. Tsuji, Y. Ito, Y. Saito, Y. Minamino, Scripta Materialia 47 (2002) 893.
[19] S. Ranjbar, S.A. Akbari Mousavi1, A.R. Shahab, Advanced Materials Research 264-265 (2011) 183.
[20] J. May, D. Amberger, M. Dinkel, H.W. Hoppel, M. Goken, Materials Science Engineering A 483-484 (2008) 481.
[21] C.Y. Yu, P.W. Kao, C. P. Chang, Acta Materialia 53 (2005) 4019.
[22] Y. Iwahashi, Z. Horita, M. Nemoto, T.G. Langdon, Acta Materialia 45 (1997) 4733.
[23] Z. Horita, T. Fujinami, M. Nemoto, T.G. Langdon, J. Materials Process Technology 117 (2001) 288.
[24] W. J. Kim, J. K. Kim, T. Y. Park, S. I. Hong, D. I. Kim, Y. S. Kim, J. D. Lee, Metallurgical and Materials Transaction A 33 (2002) 3155.
[25] N. Hansen, Acta Metallurgica 25 (1977) 863.
[26] S. Hossein Nedjad, M.R. Movaghar Gharabagh, International Journal of Materiasl Research (formerly Z. Metallkd.) 99 (2008) 11.
[27] X. Huang, N. Kamikawa, N. Hansen, Materiasl Science and Engineering A 483-484 (2008) 102.
[28] Y. Miyajima, M. Mitsuhara, S. Hata, H. Nakashima, N. Tsuji, Materials Science and Engineering A 528 (2010) 776.
[29] A. J. Ardell, Metallurgical Transactions A 16 (1985) 2131.
[30] P. B. Hirsch, F. J. Humphreys, In: Argon A, Editor. The physics and strength of plasticity. Cambridge, MA: MIT Press (1969) 189.
[31] M. A. Meyers, K.K. Chawla, Mechanical Metallurgy, Principles and Applications. Paramus, NJ: Englewood Cliffs (1984).

[32] C. J. Hsu, C. Y. Chang, P. W. Kao, N. J. Ho, C.P. Chang, Acta Materialia 54 (2006) 5241.
[33] Y.M. Park, S.C. Ryu, S.Y. Yoon, R. Stevens, H.C. Park, Materials Chemistry and Physics 109 (2008) 440.
[34] A. Deschamps, F. Danoix, F. De Geuser, T. Epicier, H. Leitner, M. Perez, Materials Letters 65 (2011) 2265.
[35] Paul S. Prevéy, Journal of Thermal Spray Technology, 9(3) (2000) 369.
[36] D. G. Morris, Revista de Metalurgia, 46 (2) (2010) 173.
[37] L. M. Cheng, W. J. Poole, J. D. Embury and D. J. Lloyd, Metallurgical and Materials Transactions A 34 (2003) 2473.
[38] N. Hansen, Scripta Materialia 51 (2004) 801.
[39] T. Shanmugasundaram, M. Heilmaier, B. S. Murty, V. Subramanya sarma, Metallurgical and Materials Transaction A, 40 (2009) 2798.
[40] X. Wang, W.J. Poole, S. Esmaeili, D.J. Lloyd, and J.D. Embury, Metallurgical and Material Transaction A 34 (2003) 2913.
[41] S. Sivasankarana, K. Sivaprasadb, R. Narayanasamya, V. Iyer, Journal of Alloys and Compounds 507 (2010) 236.
[42] N. Kamikawa, X. Huang, N. Tsuji, N. Hansen, Acta Materialia 57 (2009) 4198.
[43] N. Tsuji, International Conference on Advanced Structural and Functional Materials Design 2008; Journal of Physics: Conference Series 165 (2009) 012010.

Chapter 4

Annealing Behavior of ARB Processed Al-0.2wt%Sc Alloy Having Different Starting Microstructures

Abstract

The effect of precipitation on annealing behavior of the Al-0.2%wt.Sc alloy heavily deformed by accumulative roll bonding (ARB) up to 10 cycles was investigated. Three kinds of different microstructures, i.e., solution treated one, 300°C pre-aged one and 400°C pre-aged one after ARB process, were used as the starting structures. It was found that pinning effect by Al_3Sc suppressed recrystallization and grain growth of the matrix significantly, and especially the 400°C pre-aging was effective to stabilize the ultrafine grained structure of the matrix up to higher temperature. Dissolution of pre-existing Al_3Sc precipitates during the ARB was again suggested by re-precipitation during annealing of the ARB processed specimens at around 300°C.

Keywords: Annealing, Al-Sc, precipitation, ARB, Zener pinning.

4.1. Introduction

Microstructural restoration processes of deformed metallic materials, such as recovery, recrystallization and grain growth, have significant influence on the mechanical property of the materials. Therefore, these softening processes are of great scientific and technological interest [1]. In some alloys, the complicated situation may arise in which the processes of restoration and precipitation occur simultaneously. When a deformed supersaturated solid solution or a deformed particle-containing alloy is heat-treated, the material may exhibit complicated behaviors due to the mutual interaction between recovery/recrystallization and precipitation [2-5].

It has been shown in Chapter 2 that pre-existing precipitates give significant effects on microstructure evolution during ARB in the Al-Sc alloy, so that pre-existing particles would also affect the restoration behaviors of the alloy. The expected effects of second-phase particles on recovery and recrystallization, particularly the kinetics and resulting grain size, are summarized as follows:

- Stored energy and driving force for recovery and recrystallization increases.
- Large particles act as nucleation sites for recrystallization.
- Particles, particularly fine and closely spaced ones, exert a significant pinning effect on both dislocations and grain boundaries.

The first two effects tend to enhance recrystallization, whereas the last one tends to hinder recrystallization [4-12].

The purpose of this chapter is to investigate the annealing behavior of the Al-Sc alloy severely deformed by ARB. As has been done in the previous chapters, three kinds of different microstructures of the alloy were prepared and provided for the heavy deformation by ARB, and the ARB processed sheets were subsequently annealed under various conditions.

4.2. Experimental procedure

The material studied in this chapter is the same as that in the previous chapters. Sheets of the Al-0.2wt%Sc alloy were firstly solution treated (ST) at 903 K (630°C) for 86.4 ks and then immediately water-quenched. The solution treated sheets were aged at 573 K (300°C) or 673 K (400°C) for 10 ks, for having different size of Al_3Sc particles. The three kinds of the specimens that were solution treated, aged at 300°C and 400°C were severely deformed by ARB process up to 10 cycles at RT with lubrication, which corresponded to an equivalent strain of 8.0. The solution treated specimen, 300°C aged specimen and 400°C aged specimen are denoted as ST-ARB, 300°C Aged-ARB and 400°C Aged-ARB specimens, respectively.

After ARB processing, the specimens were annealed in a salt bath set at different temperatures ranging from 200°C to 600°C for 1.8 ks, and quenched in water after annealing. The microstructures on the sections perpendicular to the transverse direction (TD) of the sheets were characterized by electron backscattering diffraction analysis (EBSD) and transmission electron microscopy (TEM). EBSD analysis was carried out in a scanning electron microscope with a field emission type gun (FE-SEM; Philips XL30) operated at 15 KV. The specimens for the EBSD observation were mechanically polished and then electro-polished in a solution of 30% HNO_3 and 70% CH_3OH. The TEM observations were carried out using Hitachi H-800 and JEOL JEM2010 operated at 200 kV. Thin foil specimens for the TEM observation were prepared through mechanical polishing firstly down to approximately 70 μm in the thickness, and then electro-polishing in the same solution as that for the EBSD observation. Shimadzu HMW micro hardness tester was used for Vickers hardness measurement on the planes perpendicular to the normal direction (ND) of the sheets ARB processed and annealed using a load of 0.098 kgf and a time period of 10s at room temperature.

4.3. Results

4.3.1. Change in hardness during annealing process

To investigate the effect of annealing temperature on mechanical properties, Vickers micro-hardness of the ARB processed and annealed specimens was measured. The results are plotted in **Fig. 4.1**. Before ARB, the specimens have different hardness values, depending on different starting microstructures, as has been discussed in Chapter 3. After 10-cycle of the ARB process, the hardness of the ST-ARB and 400°C Aged-ARB specimens increases, whereas the hardness of the 300°C Aged-ARB specimen decreases from the initial value, as has been already shown in Chapter 3. Afterwards, three kinds of specimens show almost the similar trend in the change of hardness during annealing. That is, all specimens show a peak hardness at annealing temperature of 300°C. Above 300°C, the hardness of all specimens monotonously decreases with increasing the annealing temperature. During annealing process, the 400°C Aged-ARB specimens always show slightly higher hardness than other specimens.

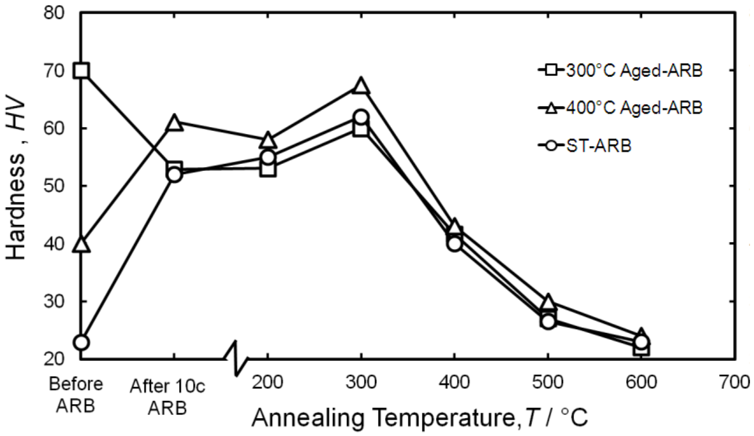

Fig. 4.1. Vickers hardness of the ST-ARB, 300°C Aged-ARB and 400°C Aged-ARB specimens as a function of annealing temperature.

4.3.2. Change in microstructure during annealing process

Figure 4.2 shows EBSD grain boundary maps of the (a, d, g, j, m, p) ST-ARB, (b, e, h, k, n, q) 300°C Aged-ARB and (c, f, i, l, o, r) 400°C Aged-ARB specimens annealed at various temperatures. The ST-ARB specimen annealed at 200°C (Fig. 4.2 (d)) has nearly the same microstructure as that in the as-ARB processed specimen (Fig. 4.2 (a)). As annealing temperature increases to 300°C, the grain size slightly increases, although specimen still contains elongated grains. The grain size increases more when the specimen is annealed at 400°C. The microstructural change of the ST-ARB specimen during subsequent annealing is continuous up to 400°C, which is like a normal grain growth of the ultrafine grained structure fabricated by ARB. The EBSD grain boundary map of the ST-ARB specimen after annealing at 450°C is shows in Fig. 4.2 (m). At 450°C, sudden growth of particular grains happens, which looks like recrystallization or abnormal grain growth. It is noteworthy that the fine grains are stable up to 400°C, which has never been achieved in pure Al ARB processed and annealed [13-14]. The result suggests the precipitation of fine Al_3Sc from the supersaturated solid solution during annealing below 400°C. As annealing temperature increases further, the grain size of the coarse grain structures increases, as shown in Fig. 4.2 (p) (annealed at 500°C).

The microstructural change during annealing of the 300°C Aged-ARB specimen is shown in Fig. 4.2 (b, e, h, k, n, q). As shown in the figures, the grain size of the 300°C Aged-ARB specimen gradually increases with increasing the annealing temperature up to 400°C. After annealing at 450°C, the 300°C Aged-ARB specimen consists of fine grains and coarse grains, indicating the occurrence of abnormal grain growth or recrystallization. The number of coarse grains appeared in the 300°C Aged-ARB specimen is smaller than that in the ST-ARB specimen after annealing at 450°C. The grain size of the coarse grain structures increases after annealing at 500°C (Fig. 4.2 (q)).

The same tendency is observed in the 400°C Aged-ARB specimen up to 400°C annealing (Fig. 4.2 (c, f, i, l)), although the size of the grains is slightly different from those in the ST-ARB specimen and 300°C Aged-ARB specimen. It is noteworthy that even after annealing at 500°C the 400°C Aged-ARB specimen still consists of fine grains with grain size of approximately 2 μm, as shown in Fig. 4.2 (r). That is, the fine grain structure was more stable in the 400°C Aged-ARB specimen than in other specimens. **Figure 4.3** shows EBSD grain boundary maps of the 400°C Aged-ARB specimens annealed at 550 °C. As shown in Fig. 4.3, annealing at 550 °C causes abnormal grain growth or recrystallization in the 400°C Aged-ARB specimen. It seems that at this temperature, the pinning effect of precipitates removed and sudden grain growth happens.

Figure 4.4 shows EBSD grain boundary maps of the ST-ARB, 300°C Aged-ARB, 400°C Aged-ARB specimens annealed at 600 °C. At higher annealing temperatures like 600°C, more equiaxed and uniform microstructures evolve as shown in Fig. 4.4. The more uniform and equiaxed grains are observed in the 400°C Aged-ARB specimen compared with other specimens. The smaller grain size is observed in the 300°C Aged-ARB specimen than those in the ST-ARB specimen and 400°C Aged-ARB specimen after annealing at 600°C.

The quantitative microstructural characterization mentioned above shows the more stabilized structure at high annealing temperatures in the Al-Sc alloy than that in the ARB processed and annealed pure Al previously reported [13-14]. The result indicates that the fine Al_3Sc precipitates in the Al-Sc alloy lead to more stable microstructure up to high annealing temperature compared with pure Al.

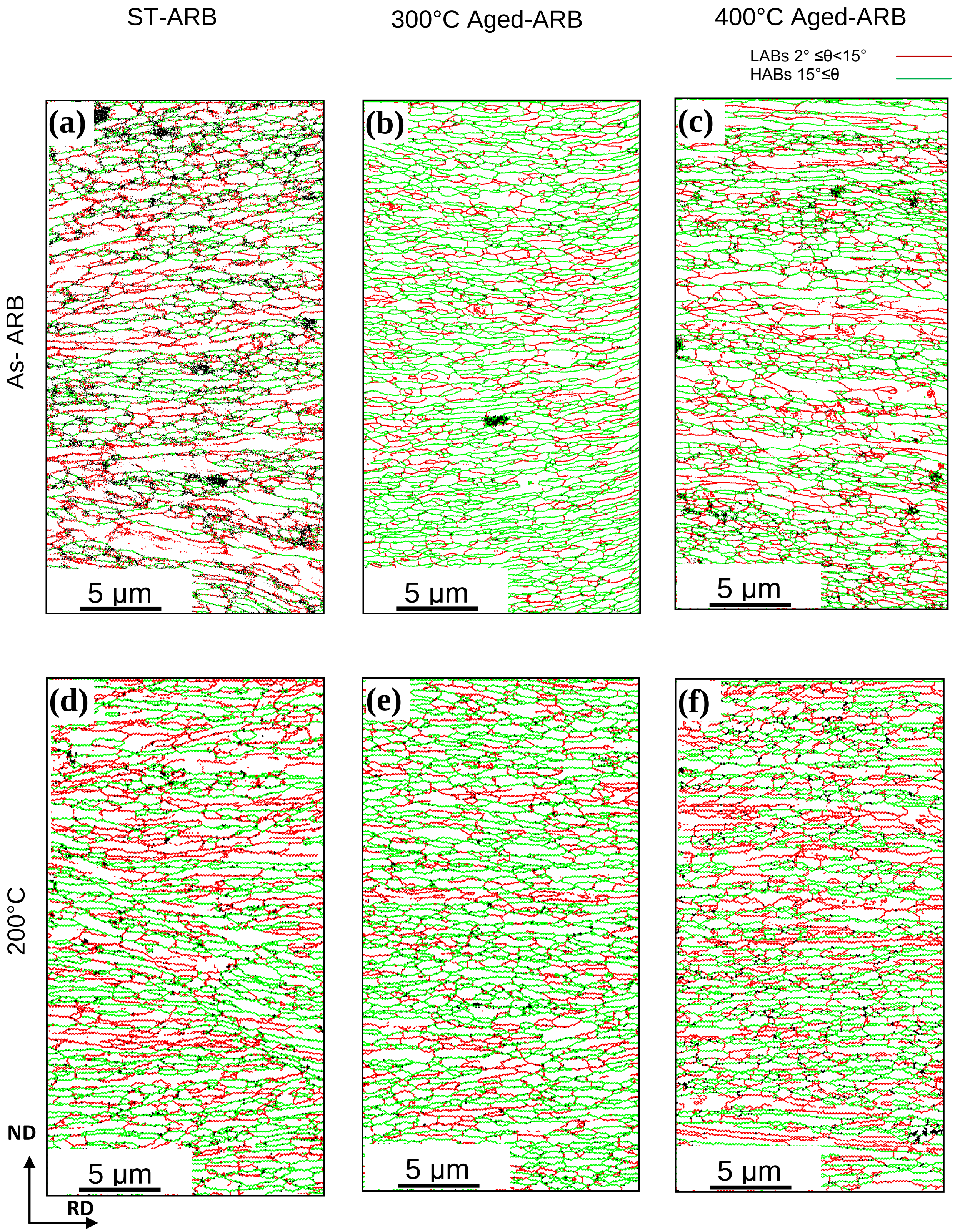

Fig. 4.2. EBSD grain boundary maps of the (a, d) ST-ARB, (b, e) 300°C Aged-ARB, and (c, f) 400°C Aged-ARB specimens (a, b, c) before annealing and (d, e, f) annealed at 200°C after 10-cycle of ARB.

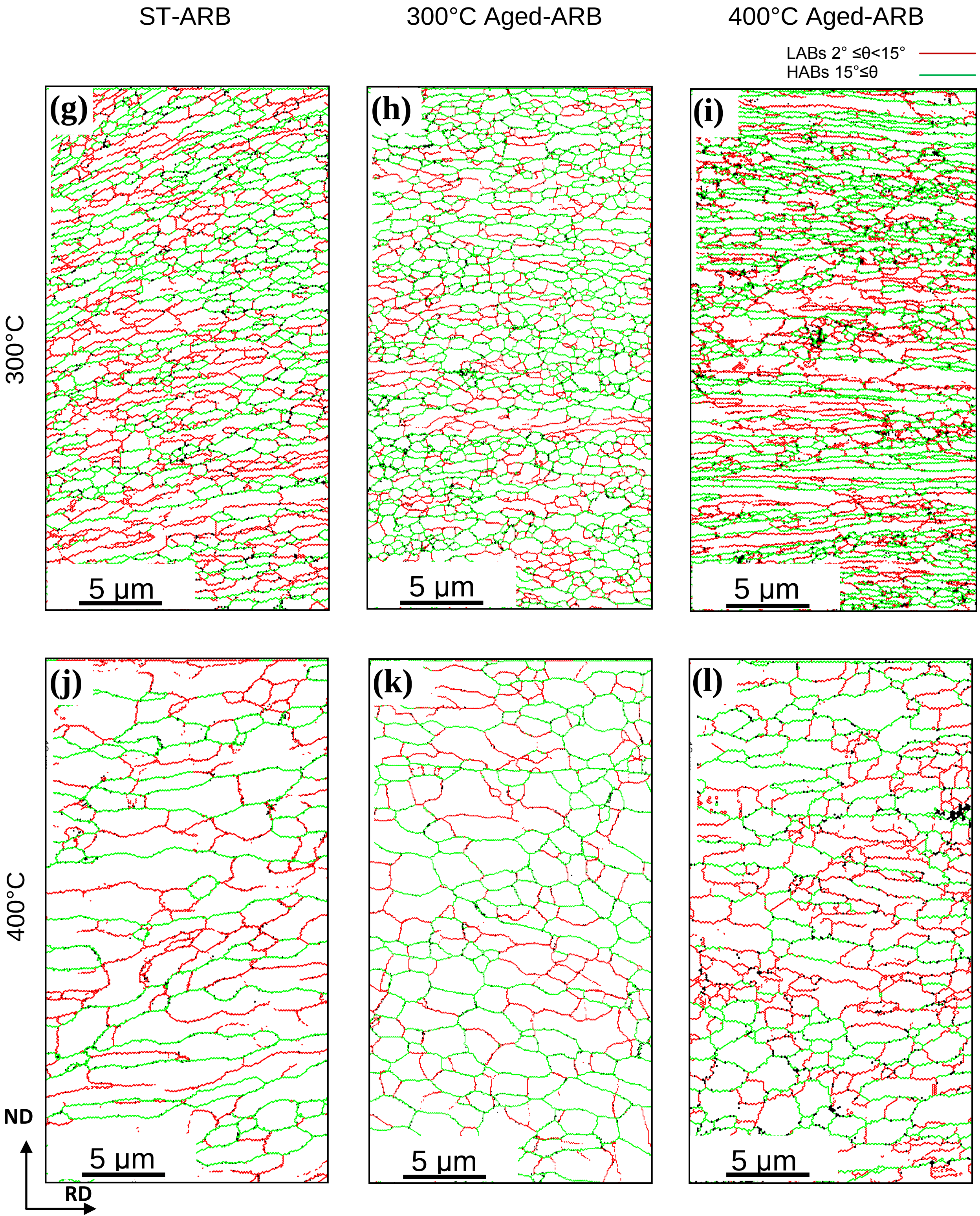

Fig. 4.2. (Continued) EBSD grain boundary maps of the (c, d) ST-ARB (j, k) 300°C Aged-ARB and (q, r) 400°C Aged-ARB specimens annealed at 300°C (g, h, i) and 400°C (j, k, l) after 10-cycle of ARB.

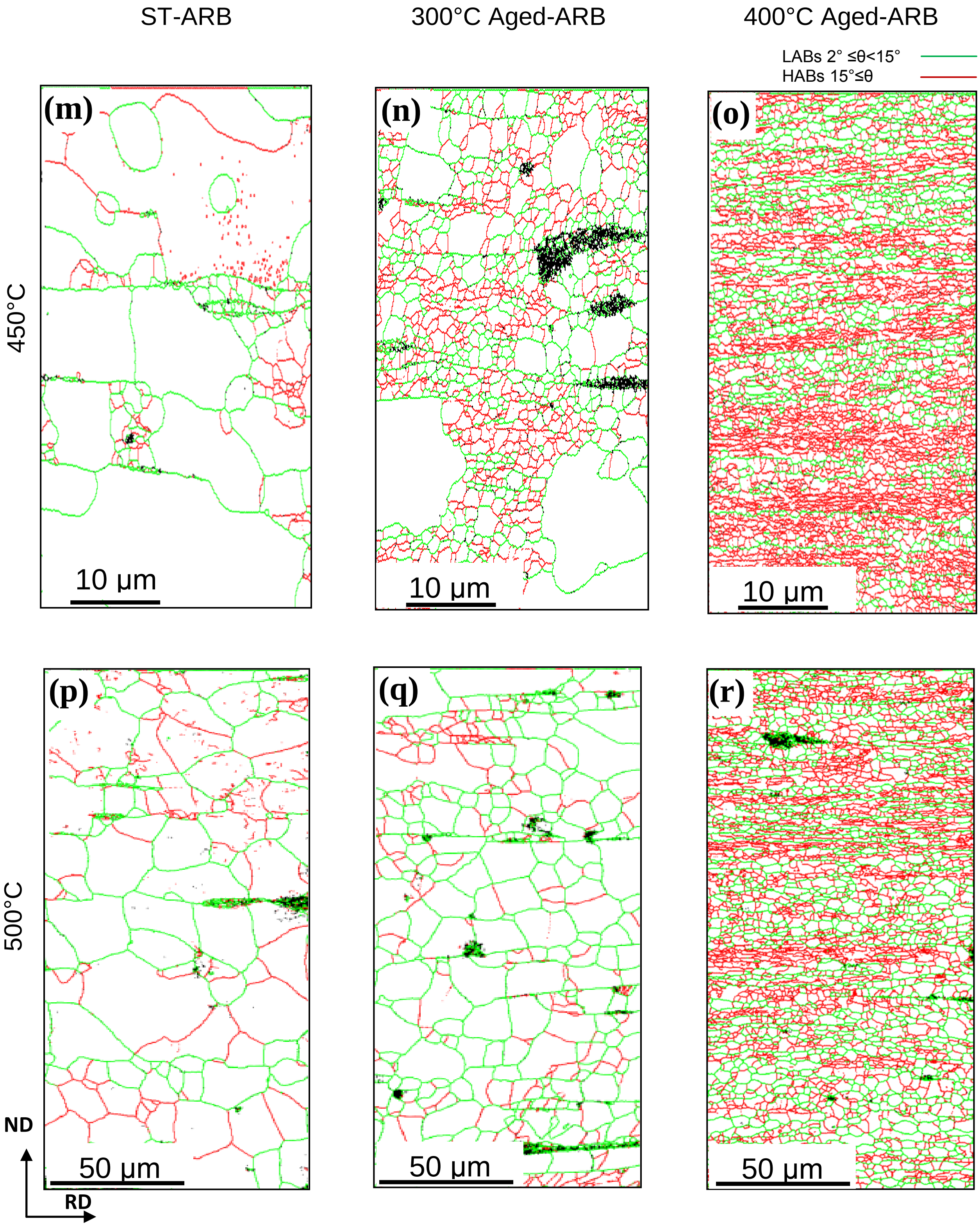

Fig. 4.2. (Continued) EBSD grain boundary maps of the (e, f) ST-ARB, (l, m) 300°C Aged-ARB, and (s, t) 400°C Aged-ARB specimens annealed at 450°C (m, n, o) and 500°C (p, q, r) after 10-cycle of ARB.

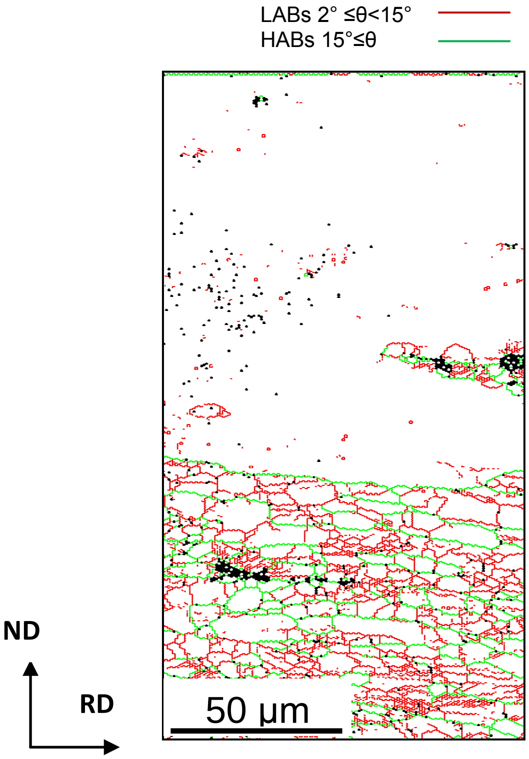

Fig. 4.3. EBSD grain boundary maps of the 400°C Aged-ARB specimen annealed at 550°C after 10-cycle of ARB.

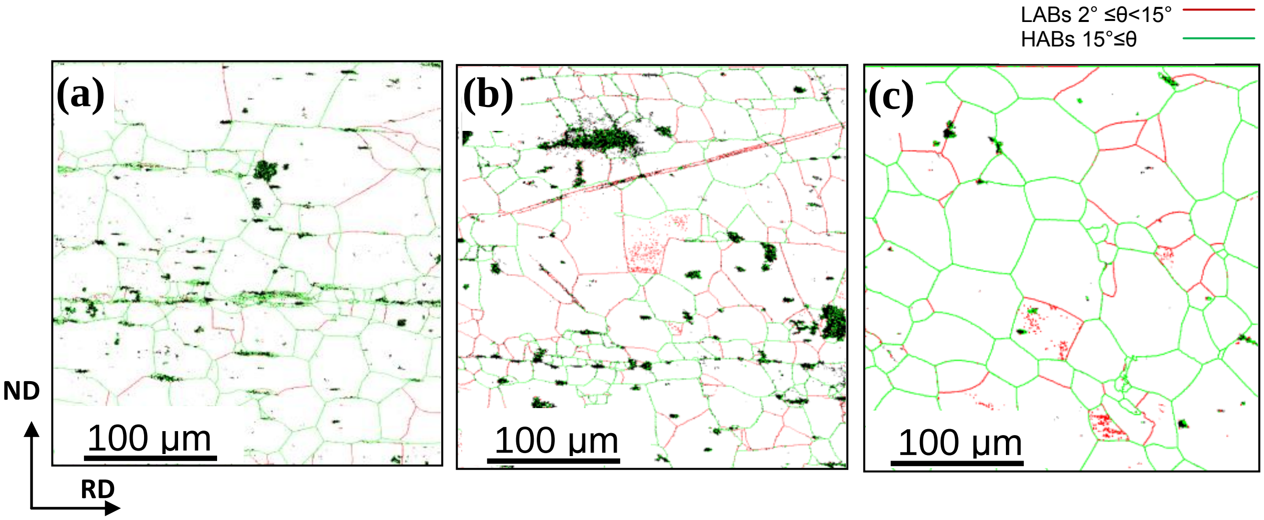

Fig. 4.4. EBSD grain boundary maps of the (a) ST-ARB, (b) 300°C Aged-ARB, and (c) 400°C Aged-ARB specimen annealed at 600°C after 10-cycle of ARB.

The change in mean grain sizes (d_t) of the ST-ARB specimen, 300°C Aged-ARB specimen and 400°C Aged-ARB specimen during annealing are plotted as a function of annealing temperature in **Fig. 4.5**. The mean interval of high-angle grain boundaries (HAGBs) along ND was evaluated by the line interseption method, and treated as the mean grain size (d_t). The grain sizes of all specimens are kept below 1 μm up to 400°C annealing. This is because fine particles pre-exist or precipitate in all specimens and they strongly inhibit the recrystallization and grain growth of the matrix significantly. On the other hand, the change in the grain size of the 2N-Al as a function of annealing temperature is shown in Fig. 4.5, which was reported by Tsuji *et al.* [13] and Kamikawa *et al.* [14]. The smaller grain size in the Al-Sc is due to the existence of the Al_3Sc precipitates which greatly inhibit grain boundary movement and retard the grain growth compared with pure Al.

The grain size of the most specimens greatly increases by annealing above 400°C. As annealing temperature increases to 500°C, the average grain size of the ST-ARB and 300°C Aged-ARB specimen is 11 μm and 5.5 μm, respectively. In contrast, not so much change of the grain size is observed in the 400°C Aged-ARB specimen and the grain size of the 400°C Aged-ARB specimen maintains approximately 2 μm after annealing at 500°C. The significant differences between the 400°C Aged-ARB specimen and other specimens could be attributed to the difference in precipitates in the 400°C Aged-ARB specimens. That is, probably in the 400°C Aged-ARB specimen, larger amount of pre-existing Al_3Sc was dissolved during ARB and re-precipitate as finer Al_3Sc particles during subsequent annealing.

The grain size becomes very coarse at annealing temperature of 600°C. It is expected that Al_3Sc is dissolved at 600°C, because the solubility limit temperature in Al-0.2%wt.Sc is 590°C. It can be concluded that the existence of Al_3Sc precipitates in the Al-Sc alloy greatly retards the recrystallization and grain growth compared with pure Al.

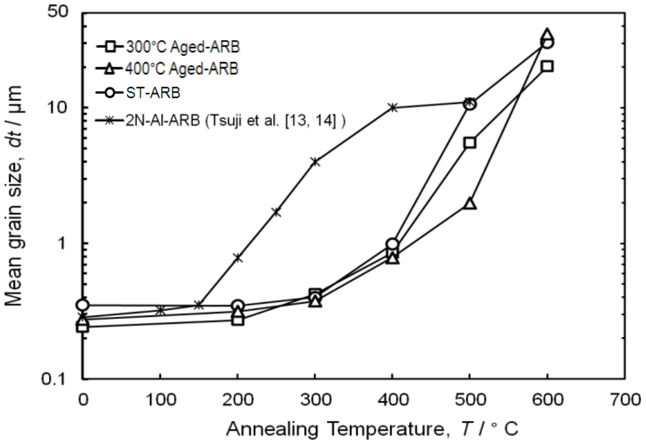

Fig. 4.5. The grain size of the ST-ARB, 300°C Aged-ARB and 400°C Aged-ARB specimens as a function of annealing temperature. The data of 2N-Al previously reported [13, 14] are also indicated.

4.3.3. Morphology of precipitates in annealed specimens

It was shown in the former section that the 400°C Aged-ARB specimens showed finer grain size compared with ST-ARB and 300°C Aged-ARB specimens. It was also indicated that Al-Sc alloy was more stable at high annealing temperatures compared with pure Al. In this section, the morphology of the Al_3Sc precipitates and their interaction with dislocations and boundaries are investigated through TEM observations.

4.3.3.1. TEM investigation of ST-ARB specimen after annealing at 300°C

TEM micrographs of the ST-ARB specimen after annealing at 300°C is shown in **Fig. 4.6**. Higher magnification of the rectangle area surrounded by white broken-lines in Fig.4.6 (a) is shown in Fig.4.6 (b). Although it is somewhat difficult to find precipitates in TEM observation in the ST-ARB specimen, some precipitates are observed in local areas. The precipitates are aligned along RD, indicating that the particles firstly precipitate on the grain boundaries and then the migration of grain boundary is occurred during further annealing. Those precipitates are responsible for stabilizing the structure at high annealing temperatures in the Al-Sc alloy. They are also the reason for the increase in the hardness value after annealing at 300°C, as was shown in Fig. 4.1.

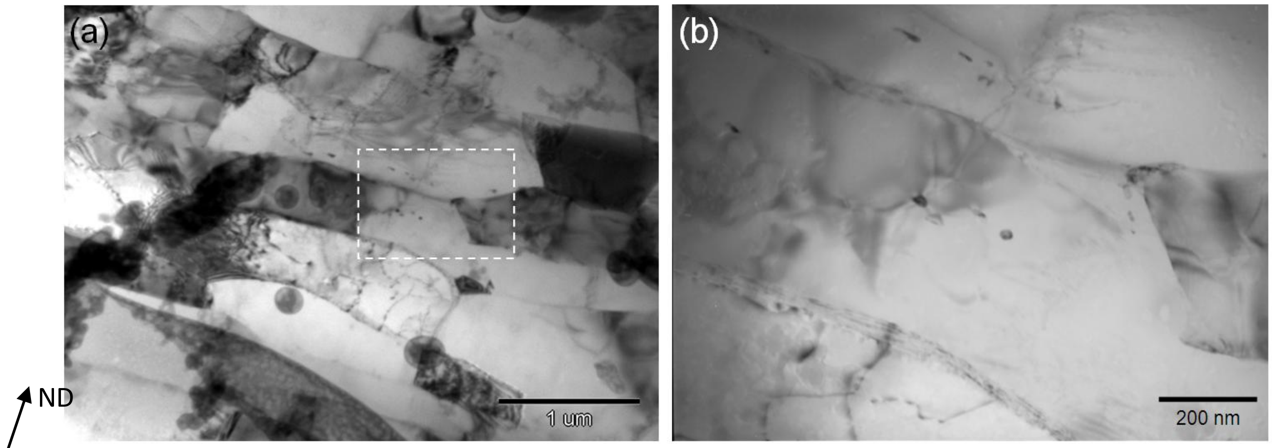

Fig. 4.6. TEM micrographs of the ST-ARB specimen after annealing at 300°C.

4.3.3.2. TEM investigation of Aged-ARB specimens at higher annealing temperature

The morphology of Al_3Sc precipitates and their interaction with dislocations or boundaries in the 300°C Aged-ARB specimen and 400°C Aged-ARB specimen were also studied by TEM. TEM micrographs of the 300°C Aged-ARB specimen after annealing at 500°C are shown in **Fig. 4.7**. As shown in this figure, there are two types of precipitates: fine precipitates having the average size of about 10 ~ 20 nm as indicated by a dotted circle in (a) and circle-1 in (c), and precipitates with size of 100 nm as indicated by a white dotted circle in (b). Because the diffraction spots of Al_3Sc precipitates is very weak, it is difficult to know the orientation of these Al_3Sc precipitates. Therefore, Ashby-Brown contrasts [12, 15-16] are used to understand the degree of coherency between a particle and the matrix. The Ashby and Brown contrast consists of spherical strain lines and irregular strain lines. The Ashby and Brown contrast appears around a spherical coherent precipitate in bright-field images. Loss of spherical strain caused by the introduction of interfacial dislocations is detected by the irregularity of the strain lines in the Ashby-Brown contrast. It is well known that the spherical strain lines appear around a spherical coherent particle, whereas irregular strain lines appear inside a semi-coherent particle. Both of spherical strain lines (circle-1 in (c)) and irregular strain lines (circle-2 in (c)) are observed around relatively large particles in the TEM micrograph, suggesting the presence of both coherent and semi-coherent ones even in large precipitates.

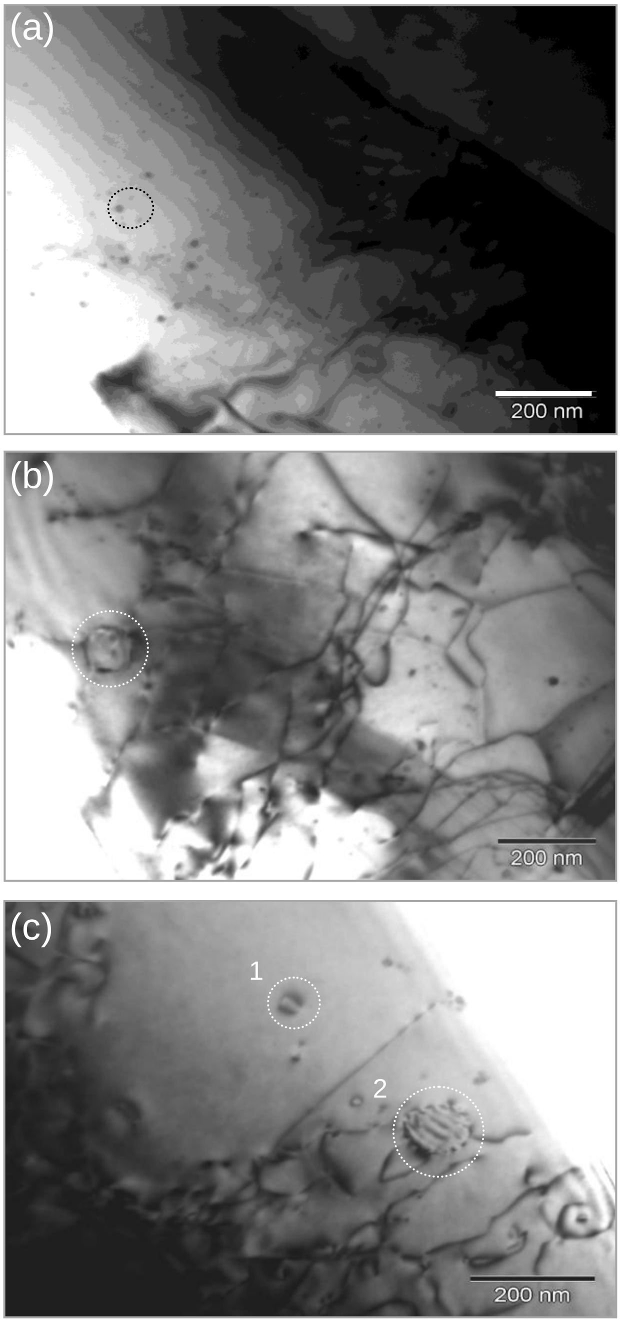

Fig. 4.7**.** TEM micrographs of the 300°C Aged-ARB specimen after annealing at 500 °C.

The TEM micrograph of **Fig. 4.8** illustrates the interaction between a grain boundary and a Al_3Sc particle in the 300°C Aged-ARB specimen annealed at 500°C. The Ashby-Brown irregular strain lines confirm that it is a semi-coherent precipitate [12, 15-16]. It can be seen that since the boundary is curved at the precipitate, the grain boundary migration is affected by the precipitates, as expected.

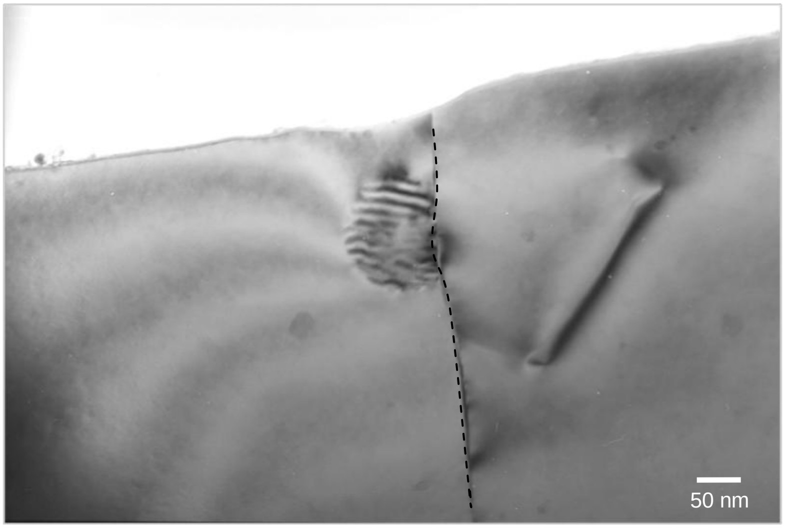

Fig. 4.8. TEM micrograph of the 300°C Aged-ARB specimen annealed at 500 °C showing interaction between a boundary and an Al_3Sc precipitate.

Figure 4.9 shows an interaction between dislocations and Al_3Sc precipitates in the 400°C Aged-ARB specimen after annealing at 500 °C. A large amount of precipitates with average size of ~ 40 nm in diameter, which have the identical orientation to the matrix, can be seen within the matrix, interacting with dislocations. These Al_3Sc precipitates are considered as the particles that re-precipitated during annealing after dissolution during ARB. The dislocations are pinned by these fine precipitates, which corresponds to the higher hardness (Fig. 4.1) and slower recrystallization (Fig. 4.2) in the 400°C pre-aged specimen than other specimens.

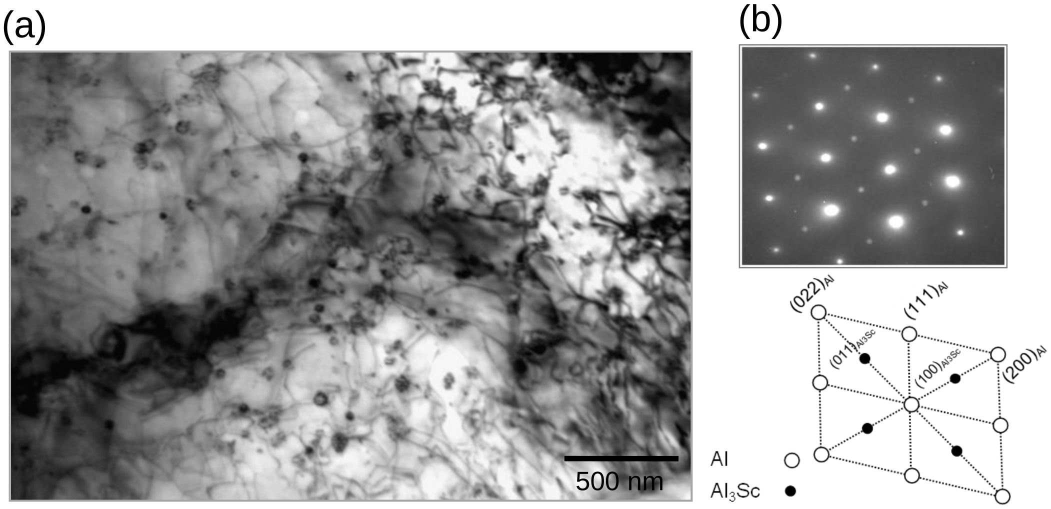

Fig. 4.9. (a) TEM micrograph of the 400°C Aged-ARB specimen after annealing at 500°C, and (b) corresponding diffraction pattern and key diagram.

Figure 4.10 is another TEM micrograph of the 400°C Aged-ARB specimen after annealing at 500°C. A recrystallized grain having lower dislocation density is observed at upper right position in the micrograph, and the grain boundary of the recrystallized grain is pinned by precipitates. This is an evidence of Zener pinning effect by precipitates to retard recrystallization and grain boundary migration.

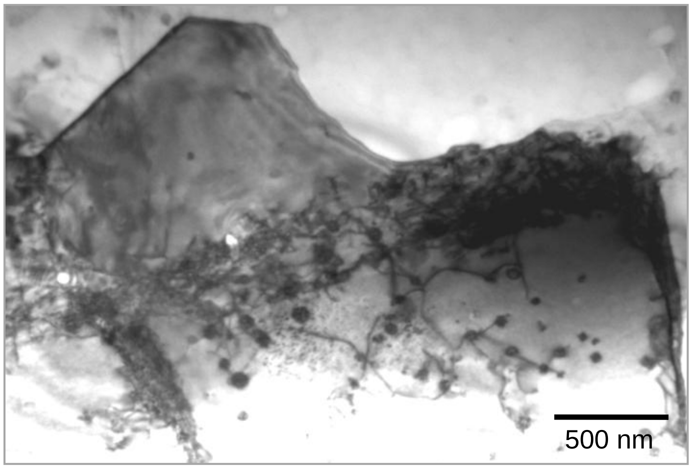

Fig. 4.10. TEM micrograph of the 400°C Aged-ARB specimen after annealing at 500°C.

4.4. Discussion: Effect of precipitates on recrystallization behaviors during annealing

It has been shown in the previous sections that the pre-existing precipitates in the Aged-ARB specimen effectively pin the growth of grain boundaries, resulting in the restriction of microstructure coarsening during annealing process. In addition, some interesting phenomena were observed;

(1) Increase of the hardness in all specimens by 300°C annealing (Fig. 4.1).

(2) The grain growth is retarded in the 400°C Aged-ARB specimen up to higher temperature, compared with the ST-ARB and 300°C Aged-ARB specimens (Fig. 4.7).

Generally, it is expected that the hardness decreases with increasing the annealing temperature due to recovery and recrystallization. However, it has been shown in Fig. 4.1 that all specimens show an increase in hardness by annealing at 300°C. This result suggests that the increase of hardness is probably due to re-precipitation of dissolved Sc in the ARB processed specimens during annealing at 300°C. The precipitation of Al_3Sc at 300°C has actually been shown in Fig. 4.6. The highest hardness of the 400°C Aged-ARB specimen after 300°C annealing (Fig. 4.1) indicates that initially coarse precipitates are dissolved during ARB process and fine and coherent Al_3Sc re-precipitate in the subsequent annealing. This is consistent with the experimental results that the volume fraction of precipitates and size of precipitates decreases significantly in the 400°C Aged-ARB specimen during ARB process, as has been shown in Chapter 3 (Fig. 3.10).

In another point of view, the Al_3Sc precipitates greatly inhibit grain boundary movement and keep the matrix grain size very fine even after high annealing temperatures. It is well known that the pinning force of the precipitates gives an important effect on grain boundary migration. The Zener pinning force, P_z, can be expressed as,

$$P_z = \frac{(3 \cdot \gamma` \cdot f_s)}{R} \tag{4.1}$$

where f_s is volume fraction of the precipitates, γ' is grain boundary energy and R is particle radius [17-18]. Since re-precipitation of fine and coherent Al_3Sc occurs more in the 400°C Aged-ARB specimen, due to dissolution of coarse pre-existing particles, finer precipitates pin the grain growth more effectively.

4.5. Conclusions

The annealing behaviors of the Al-0.2%wt.Sc alloy heavily deformed by ARB process were studied using three kinds of starting microstructures. Following conclusions can be made:

(1) The specimens annealed at 200°C had nearly the same microstructure as that in the as-ARB processed specimen. The grain size increased gradually when the specimen was annealed up to 400°C. The fine structure maintained up to 400°C due to fine Al_3Sc precipitates. At 450°C, sudden growth of particular grains occurred in the ST-ARB and 300°C Aged-ARB specimens. The grain size of the coarse grained structures increased by annealing at 500°C. The fine grain structure was more stable in the 400°C Aged-ARB specimen than those in other specimens and abnormal grain growth or recrystallization appeared at 550 °C in the 400°C Aged-ARB specimen.

(2) During annealing, the finer and more stabilized microstructure is observed in the Al-Sc alloy compared with pure Al previously reported, which was due to the fine Al_3Sc particles in the Al-Sc alloy.

(3) All specimens showed an increase in hardness by annealing at 300°C. The increase of hardness was probably due to re-precipitation of dissolved Sc in the ARB processed specimens during annealing. The highest hardness of the 400°C Aged-ARB specimen after 300°C annealing indicated large amount of precipitates were dissolved during ARB process and then the fine and coherent Al_3Sc re-precipitated in the subsequent annealing.

References

[1] J. Hirsch (Ed.), in: Virtual Fabrication of Aluminum Products, Wiley-VCH publication, Weinheim, Germany (2006).

[2] D. G. Morris, M.A. Munoz-Morris, Acta Materialia 50 (2002) 4047.

[3] M. Ferry, N. E. Hamilton, F. J. Humphreys, Acta Materialia 53 (2005) 1097.

[4] F. J. Humphreys, M. Hatherly, in: Recrystallization and related annealing phenomena, Elsevier publication, Oxford (2004).

[5] M. J. Jones, F. J. Humphrey, Acta Materialia 51 (2003) 2149.

[6] F. J. Humphrey, Acta metallurgica 25 (1977) 1323.

[7] O. Engler , X. W. Kong, P. Yang, Scripta Materialia 37 (1997) 1665.

[8] J. H. Ryu, Y.S. Lee, D. N. Lee, Metals and Materials int. 7 (2001) 251.

[9] W.Q. Cao, A. Godfrey, W. Liu, Q. Liu, Materials Science and Engineering A 360 (2003) 420.

[10] M. Somerday, FJ. Humphreys, Materials Science and Technology 19 (2003) 20.

[11] E. A. Marquis, D.N. Seidman, Acta Metallurgica 49 (2001) 1909.

[12] S. Iwamura, Y. Miura, Acta Materialia 52 (2004) 591.

[13] N. Tsuji, Y. Ito, Y. Saito, Y. Minamino, Scripta Materialia 47 (2002) 893.

[14] N. Kamikawa, N. Tsuji, X. Huang, N. Hansen, Acta Materialia 54 (2006) 3055.

[15] X. Huang, N. Tsuji, N. Hansen, Y. Minamino, Materials Science and Engineering A 340 (2003) 265.

[16] B. G. Clark, I.M. Robertson, L.M. Dougherty, Materials Research 20 (7) (2005) 1792.

[17] H. Adachi, Y. Yammoto, H. Nakanishi, T. Aida, M. Imaoka and J. Kusui, Transactions of the Indian Institute of Metals 62 (2) (2009) 159 .

[18] M. Cabibbo, E. Evangelista, M. Vedani, Materials Transaction A 36 (2005) 1353.

Chapter 5

Texture Evolution in Al-0.2 wt%Sc Alloy during ARB Process and Subsequent Annealing

Abstract

Evolution of textures in the solution treated and aged Al-0.2Sc alloy fabricated by ARB process and subsequent annealing was investigated using pole figure and orientation distribution functions (ODF) that were determined by electron backscatter diffraction (EBSD) technique. The results of deformation texture indicated that at early stage of ARB S {123} <634> orientation component developed and it changed to Copper {112} <111> and Taylor {4 4 11} <11 11 8> components at later ARB cycles in both ST-ARB and Aged-ARB specimens. However, in the Aged-ARB specimens after 5-cycle ARB process, Copper {112} <111> component decreased and Taylor {4 4 11} <11 11 8> component did not developed. Cube {100} <001> component strongly developed in the 400°C Aged-ARB specimen by annealing at high temperature, whereas this component did not develop in the ST-ARB and 300°C Aged-ARB specimen. Such a difference was understood as the effect of Al_3Sc precipitates.

Keywords: accumulative roll bonding (ARB), annealing, ODF, texture.

5.1. Introduction

Microstructural evolution of an Al-0.2Sc alloy during ARB process has been discussed in Chapter 2. It has been shown that the ARB process fabricates ultrafine grain (UFG) structures in this material. On the other hand, texture is another important feature that can control the properties of the UFG materials [1-7]. It has been shown that evolution of texture in the ARB processed materials is somehow different from that in conventionally rolled materials [8]. In addition, when supersaturated solid solution and particle-containing alloys are annealed, the interaction between precipitation and recrystallization may influence the texture evolution in this alloy. Therefore, the texture development in the annealed specimens is also interesting.

Some parameters, such as alloy composition, precipitates, shear bands, initial texture and grain sizes would greatly affect the texture evolution during rolling and also subsequent annealing, leading to different types of texture [2-4, 9-15]. The effect of Al_3Sc precipitates on microstructure evolution has been discussed in Chapter 2. It is of particular interest in this chapter to study the effect of those precipitates on texture evolution during ARB and also subsequent annealing. It should be noted that some researchers have studied texture formation in SPD materials including ARB processed ones [3-6], but texture of particle-containing materials deformed by ARB has not yet been studied. In the present chapter, the texture evolution in the solution treated and aged Al-0.2Sc alloy deformed by ARB process and also after annealing of deformed materials is investigated.

5.2. Experimental procedure

The material studied in this chapter was the same as that in the previous chapters. Sheets of the Al-0.2Sc alloy were firstly solution treated at 903 K (630°C) for 86.4 ks and then immediately water-quenched. The solution treated sheets were aged at 573 K (300°C) or 673 K (400°C) for 10 ks, for having different sizes of Al_3Sc precipitates. Three kinds of the starting specimens were severely deformed by ARB process up to 10 cycles at RT with lubrication, which corresponds to an equivalent strain of 8.0. The solution treated specimen, 300°C aged specimen and 400°C aged specimen after ARB process are denoted as ST-ARB, 300°C Aged-ARB and 400°C Aged-ARB specimens, respectively. After the ARB process, specimens were annealed in a salt bath set at different temperatures from 200°C to 600°C for 1.8 ks, followed by water quenching. To obtain the texture of the specimens, crystal orientation map of a large area of 500μm × 100μm were measured by electron backscatter diffraction (EBSD) in a scanning electron microscope with field emission gun type (FE-SEM; Philips XL30) using a step size of 0.2 μm. The EBSD data were analyzed by orientation imaging microscopy (OIM) software. The specimens for EBSD observation were mechanically polished and then electro-polished in a solution of 30% HNO_3 and 70% CH_3OH.

Pole figures and orientation distribution function (ODF) are used for texture analysis in this chapter. The ODF quantitatively describes the probability of particular orientations in the materials within Euler space. The orientations and Euler angles of typical orientations in rolling texture and recrystallization texture of fcc crystal are given in **Table 5.1** and their ideal positions in ODF are shown in **Fig. 5.1**. Copper, S, Brass, Goss and Cube are the nicknames used for each texture component (orientation) used in this chapter. The orientations are represented by the expression of {h k l} <u v w>, where {h k l} represents the Miller index of the crystallographic plane parallel to the rolling plane and <u v w> represents the Miller index of the crystallographic direction parallel to the rolling direction (RD).

Table 5.1. Orientations and Euler angles of typical orientation component in rolling texture and recrystallization texture of fcc crystal.

Name		**{h k l} <u v w>**	**Euler angle, °** **Φ, φ_1 ,φ_2**
Cube		{0 0 1} <1 0 0>	(0,0,0)
Copper		{1 2 1} <1 -1 1>	(39,66,27)
S1	S	{1 2 4} <2 1 -1>	(59,29,63)
S2		{1 2 3} <4 1 -2>	(47,37,63)
S3		{1 2 3} <6 3 -4>	(59,37,63)
Brass		{1 1 0} <-1 1 2>	(35,45,0)
Taylor		{4 4 11} <11 11 -8>	(90,27,45)
Goss		{1 1 0} <0 0 1>	(0,45,0)

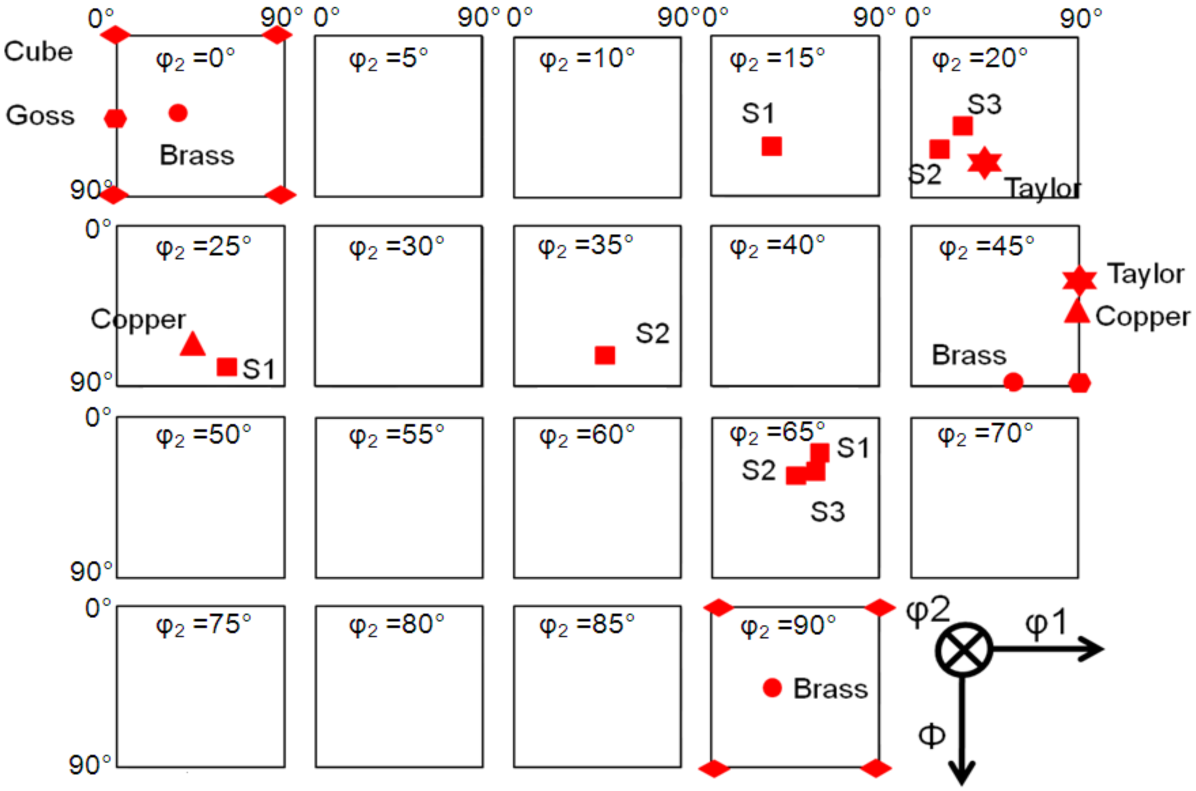

Fig. 5.1. ODF sections of constant φ_2 showing the ideal positions of typical orientation components in rolling texture and recrystallization texture of fcc crystal.

5.3. Results and Discussion

5.3.1. Texture evolution during ARB processing

The {111} pole figures of three kinds of specimens after 1 cycle, 3 cycles, 5 cycles, 7 cycles and 10 cycles of the ARB process are shown in **Fig. 5.2**. All those were obtained from the EBSD orientation mapping data for the areas of 500μm × 100μm. The positions of ideal orientation for typical rolling texture components of fcc crystal, i.e., Copper {112} <111>, S {123} <634> and Brass {011} <211>, are also indicated in the {111} pole figures of Fig. 5.2.

As shown in Fig. 5.2, S {123} <634> component is developed as a main texture by 1-cycle ARB in the ST-ARB specimen. The texture changes to Copper {112} <111> component with increasing the ARB cycle up to 10 cycles. S {123} <634> component is developed as a main texture by 3-cycle ARB in the 300°C Aged-ARB specimen containing fine Al_3Sc, and finally the texture changes to Copper {112} <111> component by 10-cycle ARB. The same tendency is observed in the 400°C Aged-ARB specimen, however, the intensity of those components is different between the 300°C Aged-ARB and 400°C Aged-ARB specimens. As a result, it can be concluded that texture transition occurs during ARB process in all specimens, however final texture after 10 cycles and the intensity distribution in the {111} pole figure are different depending on the starting microstructures.

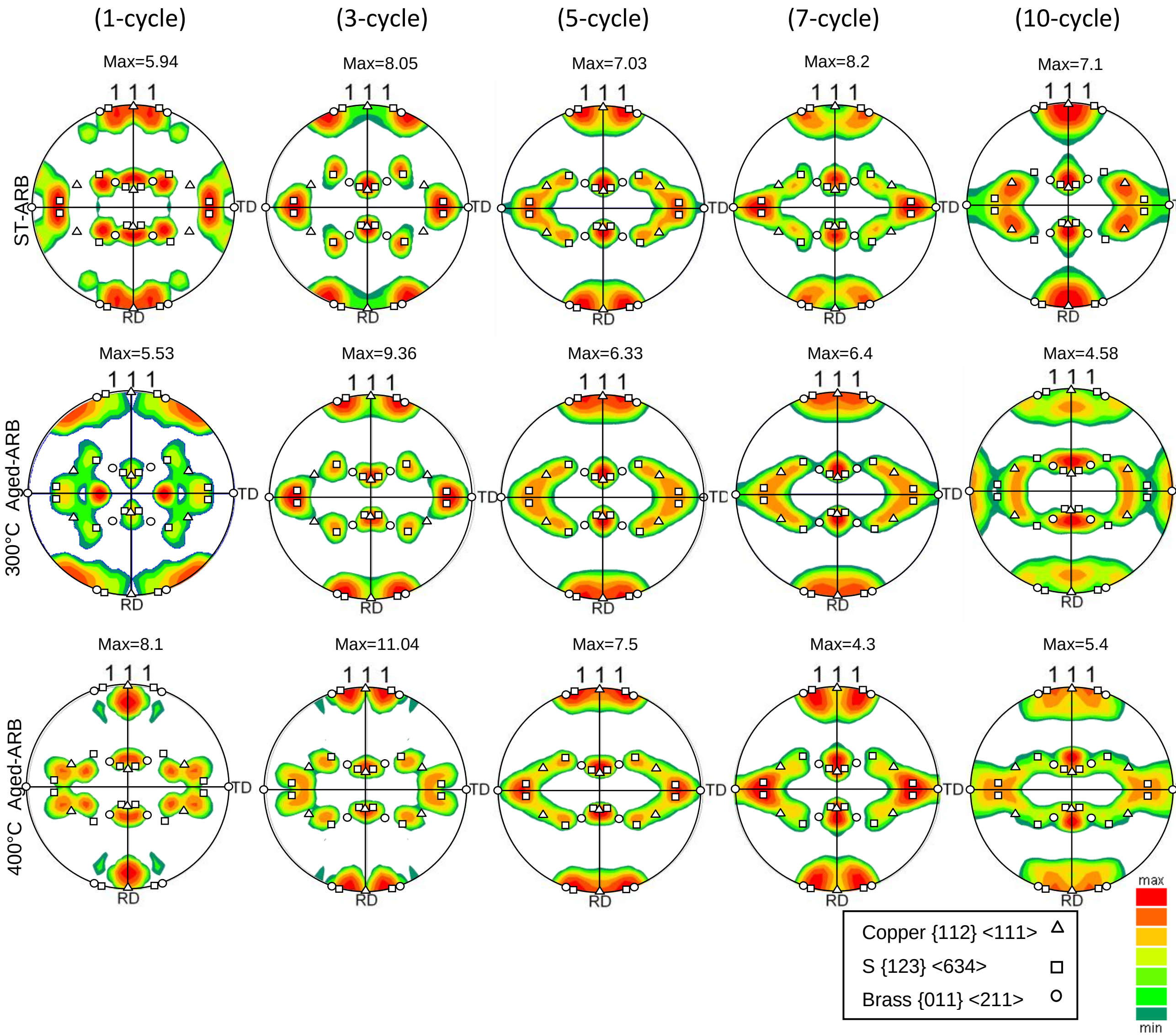

Fig. 5.2. {111} pole figures of the ST-, 300°C aged and 400°C aged specimens ARB processed by various cycles.

The information provided by pole figures refers only to the statistical distribution of each pole direction and there is no way to obtain the complete orientation intensity of individual grains from the pole figures. For quantitative understanding about the change in texture during the ARB process, ODF of the ST-ARB, 300°C Aged-ARB and 400°C Aged-ARB specimens after various number of ARB cycles was analyzed using EBSD data. The ODF is defined as a probability of the density of orientations. The intensity for each orientation was measured by ODF analysis with symmetric condition in Euler space using OIM software. Deviation angle of 5° from the exact ideal orientation was allowed for determining the intensity of each texture component. **Figure 5.3** shows the change in the intensity of (a) Copper {112} <111> component, (b) Taylor {4 4 11} <11 11 8> component, (c) S {123} <634> component, and (d) Brass {110} <112> component as a function of the number of ARB cycles. As can be seen in Fig. 5.3 (a), the intensity of Copper {112} <111> component gradually increases with increasing the ARB cycle in the ST-ARB specimen. The intensity of Copper {112} <111> component in the Aged-ARB specimens firstly increases up to 5-cycle ARB and then decreases. The intensity of Copper {112} <111> component in the Aged-ARB specimens is higher than that in the ST-ARB specimen up to 7-cycle ARB. This result indicates that the formation of shear bands due to the existence of Al_3Sc precipitates in the Aged-ARB specimen, which is reported in Chapter 2, strengthens the Copper texture. This agrees with the previous work by Quadir *et al.* [16] who reported that Copper {112} <111> component is stabilized by shear band formation in Al alloys during ARB process. The reduction in the intensity of Copper {112} <111> component above 5 cycles in the Aged-ARB specimens (Fig. 5.3 (a)) may be attributed to the change of pre-existing precipitates, i.e., reduction of volume fraction of precipitates due to dissolution (Table 3.4).

As shown in Fig. 5.3 (b), the intensity of Taylor {4 4 11} <11 11 8> component monotonously increases with increasing the number of ARB cycle in the ST-ARB specimen and Aged-ARB specimens. On the other hand, the intensity of this component in the 300°C Aged-ARB and 400°C Aged-ARB specimens increases up to 7 cycles and 5 cycles, respectively, and then does not change. It is also shown that the intensity of Taylor {4 4 11} <11 11 8> component in the Aged-ARB specimens is higher than in the ST-ARB Specimen up to 7 cycles. As reported by Hirsch *et al.* [17] Taylor {4 4 11} <11 11 8> component develops by deformation without shear strain. It is considered that in the UFG structure, the grain boundary strongly constrains the deformation of grain interior, leading to reduction of local shear deformation and consequently Taylor {4 4 11} <11 11 8> component develops during ARB processing. Furthermore, pre-existing Al_3Sc precipitates accelerate the grain refinement in the Aged-ARB specimens (Chapter 2), leading to stronger Taylor {4 4 11} <11 11 8> component in the Aged-ARB specimens than in the ST-ARB specimen up to 7 cycles. However, the intensity of Taylor {4 4 11} <11 11 8> component does not change above 7 cycles in the 300°C Aged-ARB and 5 cycles in the 400°C Aged-ARB specimens.

Change in the intensity of S {123} <634> component for three kinds of specimens is shown in Fig. 5.3 (c). As shown in this figure, the intensity of S {123} <634> component increases up to 5 cycles and 3 cycles in the ST-ARB specimen and Aged-ARB specimens, respectively, and then it significantly decreases by 10 cycles.

Change in the intensity of Brass {110} <112> component for three kinds of specimens is shown in Fig. 5.3 (d). The strongest intensity of this component appears after 1-cycle ARB in the ST-ARB specimen. Above 3 cycles, the intensity of Brass {110} <112> component stays at low level compared with other texture components.

Figure 5.4 shows ODF data of the ST-ARB, 300°C Aged-ARB and 400°C Aged-ARB specimens after 10-cycle ARB. When compared with Fig. 5.1, the development of Copper {112} <111> component and Taylor {4 4 11} <11 11 8> component after 10 cycles is clearly shown in this figure in all specimens, however the intensity of those components are different depending on starting microstructures.

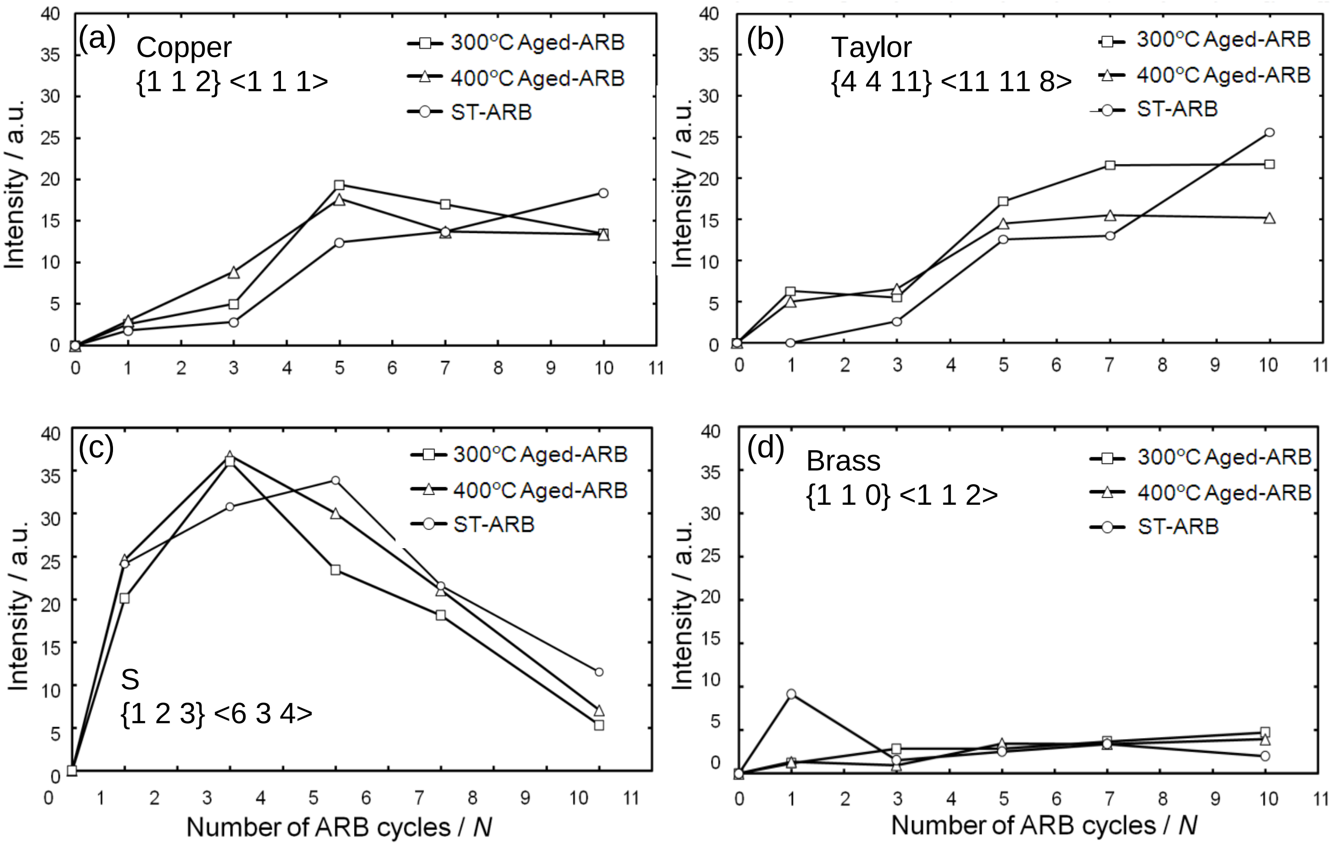

Fig. 5.3. Texture intensities of (a) Copper {112} <111>, (b) Taylor {4 4 11} <11 11 8>, (c) S {123} <634> and (d) Brass {110} <112> components in the ST-, 300°C aged and 400°C aged specimens as a function of the number of ARB cycle.

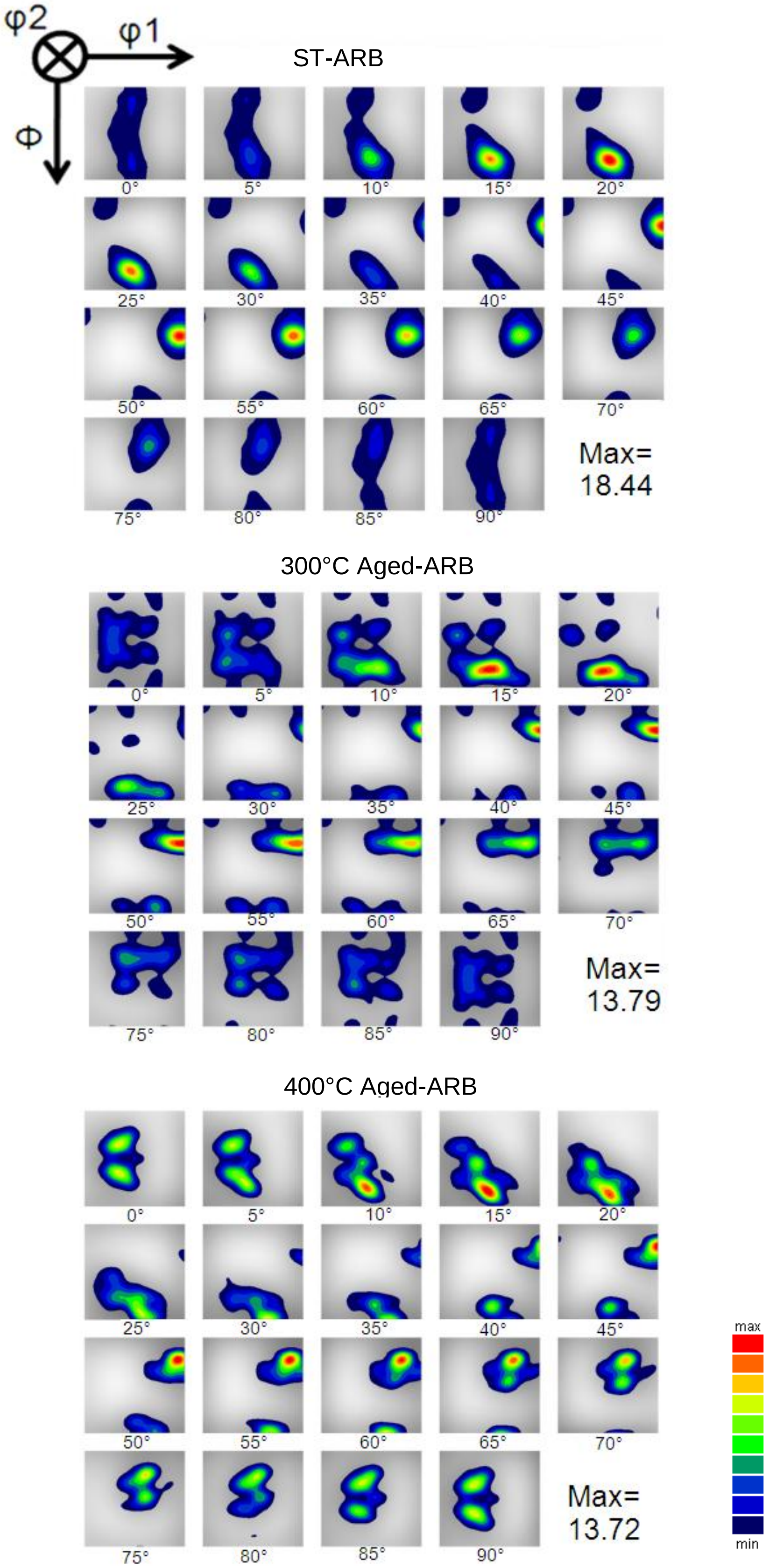

Fig. 5.4. ODF sections of constant φ_2 showing the texture components in the ST-ARB, 300°C Aged-ARB and 400°C Aged-ARB specimens after 10-cycle ARB.

5.3.2. Texture evolution of ARB processed specimens during annealing

{111} pole figures of the ST-ARB 10-cycle specimen, 300°C Aged-ARB 10-cycle specimen and 400°C Aged-ARB 10-cycle specimen after annealing at various temperatures are shown in **Fig. 5.5**. The positions of ideal orientation of typical texture components for fcc crystal, i.e., Goss {110} <001>, Copper {112} <111>, S {123} <634>, Brass {011} <211> and Cube {100} <001> components, are also indicated in the pole figures of Fig. 5.5.

As shown in Fig. 5.2, the ST-ARB specimen shows mainly Copper texture after 10-cyle ARB. The texture changes with increasing the annealing temperature, and a complicated and relatively weak texture develops after annealing at 600°C, as shown in Fig. 5.5. The same tendency is observed in the 300°C Aged-ARB specimen, although the intensity of components at each stage is different between the ST-SRB specimen and 300°C Aged-ARB specimen. In contrast, Cube {100} <001> component strongly develops in the 400°C Aged-ARB specimen after annealing at 600°C. In all specimens, the transition in texture occurs during annealing corresponding to recrystallization and grain growth.

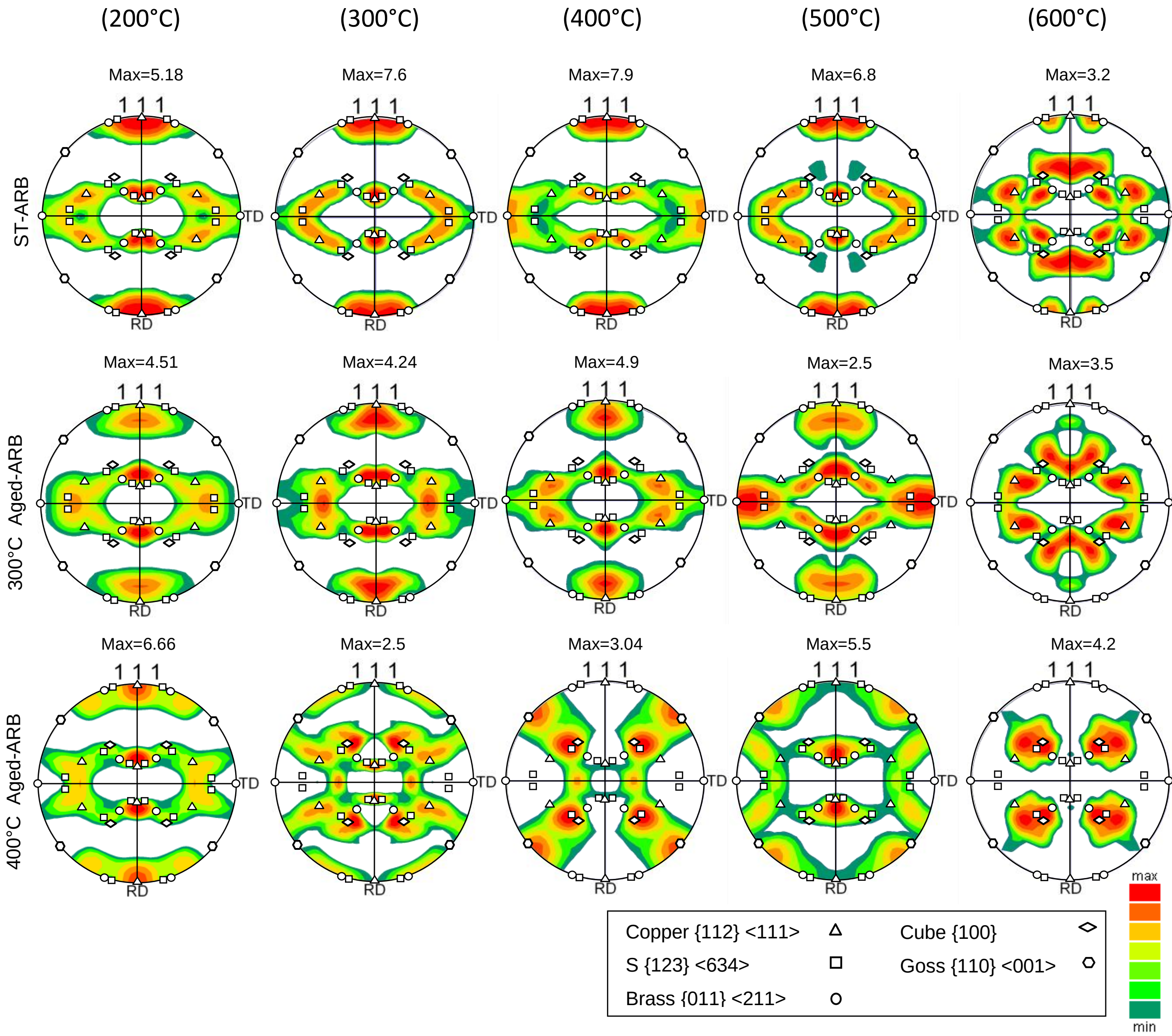

Fig. 5.5. {111} pole figures of the ST-ARB, 300°C Aged-ARB and 400°C Aged-ARB specimens during annealing process.

Figure 5.6 shows the ODF data in the ST-ARB specimen, 300°C Aged-ARB specimen and 400°C Aged-ARB specimen after annealing at 600°C. In general, Cube oriented grains (Cube {100} <001> orientation) grows preferably in annealing at high temperatures [18]. As shown in Fig. 5.6, Cube {100} <001> component strongly develops in the 400°C Aged-ARB specimen at 600°C. This development in Cube {100} <001> component is not observed in the ST-ARB specimen and 300°C Aged-ARB specimen at this temperature. The different development in

Cube {100} <001> component between the 400°C Aged-ARB specimen and other specimens can be attributed to the reservation of fine-grained structures (i.e., driving force for grain growth) at higher temperature in the 400°C Aged-ARB specimen, as shown in Chapter 4, which leads to a selective (abnormal) grain growth of Cube oriented grains (see Fig. 4.3).

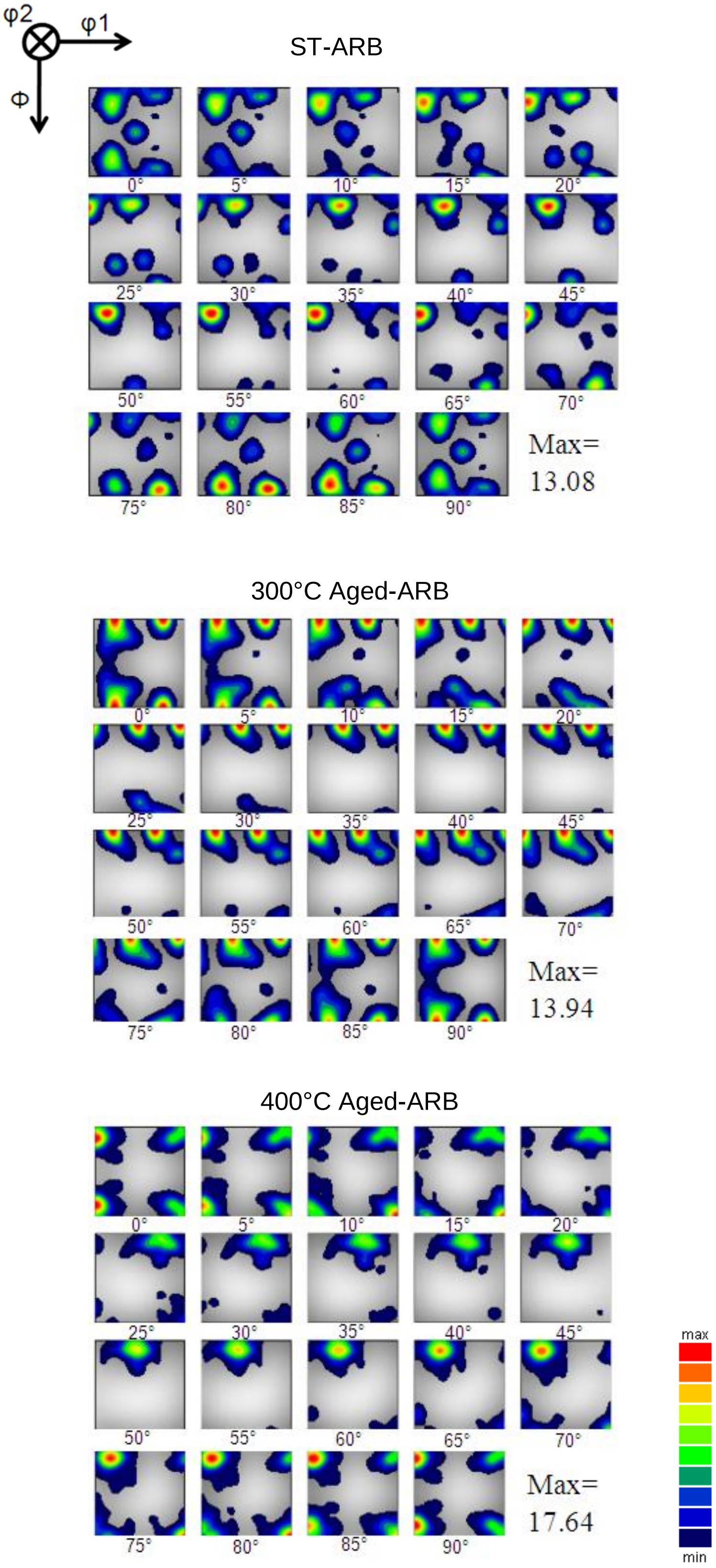

ST-ARB

300°C Aged-ARB

400°C Aged-ARB

Fig. 5.6. ODF sections of constant φ_2 showing the texture components in the ST-ARB, 300°C Aged-ARB and 400°C Aged-ARB specimens after annealing at 600°C.

5.4. Conclusions

Texture evolution in the Al-0.2Sc alloy during ARB and subsequent annealing has been characterized. The main results are summarized as follows:

(1) The intensity of Copper {112} <111> component continuously increased in the ST-ARB specimen during ARB processing. In the Aged-ARB specimens, the intensity of Copper {112} <111> components first increased up to 5 cycles and then decreased. The intensity of Taylor {4 4 11} <11 11 8> component increased with increasing the ARB cycles in the ST-ARB and Aged-ARB specimens. It is considered that in the UFG structure, the grain boundary strongly constrains the deformation of grain interior, leading to reduction of local shear deformation and consequently the development of Taylor {4 4 11} <11 11 8> component during ARB processing. The intensity of S {123} <634> component increased up to 5 cycles and 3 cycles in the ST-ARB specimen and Aged-ARB specimens, respectively, and then it significantly decreased by 10 cycles. The strongest intensity of Brass {110} <112> component appeared after 1-cycle ARB in the ST-ARB specimen, and above 3 cycles the intensity of Brass {110} <112> component stayed at low level compared with other texture components.

(2) The formation of shear bands due to the existence of Al_3Sc precipitates in the Aged-ARB specimen strengthened the Copper texture. The reduction in the intensity of Copper {112} <111> component above 5 cycles in the Aged-ARB specimens might be attributed to the change of the pre-existing precipitates, i.e., reduction of volume fraction of precipitates due to dissolution. The pre-existing Al_3Sc precipitates also accelerated the grain refinement in

the Aged-ARB specimens, leading to stronger Taylor {4 4 11} <11 11 8> component in the Aged-ARB specimens than in the ST-ARB specimen up to 7 cycles.

(3) Cube {100} <001> component strongly developed in the 400°C Aged-ARB specimen after annealing at 600°C, whereas this development was not observed in the in the ST-ARB and 300°C Aged-ARB specimens. The difference in Cube {100} <001> component between the 400°C Aged-ARB specimen and other specimens can be attributed to the reservation of fine-grained structures, i.e., as driving force for grain growth, at higher temperature in the 400°C Aged-ARB specimen, which leads to a selective (abnormal) grain growth of Cube oriented grains.

References

[1] R. Z. Valiev, Y. Estrin, Z. Horita, T. G. Langdon, M. J. Zechetbauer, Metals and Materials Society, 58 (2006) 33.

[2] K. T. Park, H. J. Kwon, W. J. Kim, Y.S. Kim, Materials Science and Engineering A 316 (2001) 145.

[3] N. Kamikawa, N. Tsuji, Y. Minamino, Science Technology Advanced Materials 5 (2004) 163.

[4] H. W. Kim, S.B. Kang, N. Tsuji, Y. Minamino, Metallurgical Materials Transaction A 36 (2005) 3151.

[5] S. G. Chowdhury, A. Dutta, B. Ravikumar, A. Kumar, Material Science and Engineering A 428 (2006) 351.

[6] S. G. Chowdhury, V. C. Srivastava, B. Ravikumar, S. Soren, Scripta Materialia 54 (2006) 1691.

[7] H. Pirgazi, A. Akbarzadeh, R. Petrov, J. Sidor, L. Kestens, Materielas Science and Engineering A 492 (2008) 110.

[8] P. L. Sun, P. W. Kao, C. P. Chang, Materials Science and Engineering A 283 (2002) 82.

[9] S. G. Chowdhury, A. Mondal, J. Gubicza,G. Kra´llics, A´. Fodor, Materials Science and Engineering A 490 (2008) 335.

[10] R. D. Angelis, T. Snyder, J. House, W. Hosford, Advances in X-ray Analysis, 42 (2000) 510.

[11] W. C. Liu, J. Morris, Metallurgical Transaction A 35 (2004) 265.

[12] S. G. Chowdhury, A. Dutta and A. Kumar, Materials Science and Engineering A, 428 (2006) 351.

[13] F. J. Humphreys, M. Hatherly, in: Recrystallization and related annealing phenomena Elsevier publication, Oxford (2004).

[14] W. C. Liu, J. Morris, Scripta Materialia 47 (2002) 743.

[15] S. Ringeval, D. Piot, C. Desrayaud, J. H. Driver, Acta Materialia 54 (2006) 3095.

[16] M. Z. Quadir, M. Ferry, O. Al-Buhamad, P. R. Munroe, Acta Materialia 57 (2009) 29.

[17] J. Hirsch, K. Lucke, Acta Metalurgica 36 (1988) 2863.

[18] G. H. Zahid, Y. Huang, P. B. Prangnell, Acta Materialia 57 (2009) 3509.

Chapter 6

General Conclusions

Al-0.2%wt.Sc alloy sheets were deformed to an equivalent strain of 8.0 (10-cycle) by accumulative roll bonding (ARB) process at room temperature. Three kinds of microstructures, i.e., ST-ARB, 300 °C Aged-ARB, and 400 °C Aged-ARB specimens were prepared as the starting materials, in order to investigate the effect of pre-existing precipitates on microstructure evolution, texture evolution and change in mechanical properties during severe plastic deformation. The specimens heavily deformed by the accumulative roll bonding (ARB) process were also provided to subsequent annealing, for understanding the restoration (recovery, recrystallization, and grain growth) behaviors of the materials. The general introduction about ultrafine grained (UFG) materials, ARB process, effect of pre-existing precipitates on microsturucture and mechanical properties during ARB and subsequent annealing, and the purpose of this thesis have been explained in **Chapter 1**.

In **Chapter 2**, microstructural evolution during ARB in the Al-0.2%wt.Sc alloy having different starting microstructures, were studied. Fine, spherical and coherent Al_3Sc precipitates with mean particle size of 3.6nm were found after aging at 300°C. On the other hand, cauliflower-like shape and coherent Al_3Sc precipitates with mean particle size of 50 nm were observed after aging at 400°C for 10 ks. Three kinds of specimens, i.e., ST-, 300°C aged and 400°C aged specimens, were severely deformed by ARB process up to 10 cycles. After 10 cycles of ARB, ultrafine lamellar boundary structures were observed in all the specimens. The mean size of the ultrafine grains in the Aged-ARB specimens was smaller than that in the ST-

ARB specimen and the fraction of high angle grain boundaries (HAGBs) in the Aged-ARB specimens were larger than those in the ST-ARB specimen.

The grain refinement was accelerated by pre-existing Al_3Sc precipitates during the ARB process. The increase in the generation and accumulation rate of dislocations due to the pre-existing precipitates as well as by the introduction of shear bands and inhabitation of short range grain boundary migration at later stage of ARB through Zener drag effect were considered as possible reasons for acceleration of grain refinement in the Aged-ARB specimens. It was also found that the effects of the finer pre-existing precipitates in the 300°C Aged-ARB specimens on grain refinement were more effective than that of the coarse precipitate in the 400°C Aged-ARB specimens.

In this chapter, the change in the state of the precipitates was also studied during the ARB process. That is, the identical orientation between the precipitates and Al matrix was kept during 1 cycle of ARB process, whereas, some precipitates had different orientation with the matrix after 9 cycles. Additionally, the cauliflower shaped precipitates with mean radius of 50 nm in the 400°C Aged-ARB specimens were changed to the fine and spherical-shaped ones with radius of 10 nm after ARB 1 cycle. It was expected that the coarse Al_3Sc precipitates were dissolved and re-precipitated, or fragmented by plastic deformation during the ARB process.

In **Chapter 3**, mechanical properties of three kinds of specimens, i.e., ST-ARB, 300°C Aged-ARB and 400°C Aged-ARB, were studied. The Vickers hardness of the ST-ARB specimen monotonously increased with increasing the number of ARB cycles. On the other hand, Vickers hardness of the 300°C Aged-ARB specimen increased by 1-cycle ARB, and then monotonously decreased with further increase of ARB cycle. The hardness of the 400°C Aged-

ARB specimen increased by 1-cycle ARB, but it did not change with further increase of ARB cycle. The same tendency was observed in the 0.2% proof stress obtained from tensile test.

In this chapter, the mechanical properties of ST-ARB and Aged-ARB specimens were correlated with the structural parameters, such as dislocation density, grain size, volume fraction and size of the precipitates, based on different strengthening mechanisms, i.e., grain boundary strengthening, dislocation strengthening and precipitation strengthening. The grain refinement strengthening increased with increasing the number of ARB cycles in all specimens, although different values were estimated between the ST-ARB and Aged-ARB specimens. The dislocation strengthening value of the ST-ARB and 300°C Aged-ARB specimens increased by 1-cycle ARB, but they monotonously decreased with further increase of the ARB cycles. On the other hand, the value in the 400°C Aged-ARB specimen increased up to 3-cycle ARB and then decreased. The precipitation strengthening gradually decreased in the 300°C Aged-ARB specimen, whereas precipitation strengthening in the 400°C Aged-ARB specimen firstly increased by 1-cycle ARB and then decreased. There was a good agreement between the tendency of the total strength calculated from the microstructural parameters and experimentally measured values of 0.2% proof stress obtained from tensile test.

In **Chapter 4**, annealing behaviors of the Al-0.2%wt.Sc alloy heavily deformed by ARB process, were investigated. The specimens annealed at 200°C had nearly the same microstructure as that in the as-ARB processed specimen. The grain size increased gradually when the specimen was annealed up to 400°C. The fine-grained structures were maintained up to 400°C due to pinning by fine Al_3Sc precipitates. At 450°C, a sudden growth of particular grains occurred in the ST-ARB and 300°C Aged-ARB specimens. The fine-grained structure was more stable in the 400°C Aged-ARB specimen than that in other specimens and abnormal grain growth or recrystallization appeared at 550 °C in the 400°C Aged-ARB specimen. It was found that pinning effect by Al_3Sc suppressed recrystallization and grain growth of the matrix significantly, and was effective to stabilize the ultrafine grained structure of the matrix in the Al-Sc alloy compared with the pure Al previously reported.

The Vickers hardness of the specimens was measured after annealing. All specimens had similar trend during annealing and showed an increase in hardness by annealing at 300°C. This result suggested the re-precipitation of dissolved Sc in the ARB processed specimens during subsequent annealing. The highest hardness of the 400°C Aged-ARB specimen during annealing indicated large amount of precipitates were dissolved during ARB process and fine and coherent Al_3Sc re-precipitated in the subsequent annealing.

In **Chapter 5**, texture evolution in the Al-0.2Sc alloy during ARB and subsequent annealing, was studied. It was shown that the intensity of Copper {112} <111> component continuously increased in the ST-ARB specimen during ARB processing. In the Aged-ARB specimens, the intensity of Copper {112} <111> components first increased up to 5 cycles and then decreased. It was shown in this chapter that the formation of shear bands due to the existence of Al_3Sc precipitates in the Aged-ARB specimen strengthened Copper texture. The reduction in the intensity of Copper {112} <111> component above 5 cycles in the Aged-ARB specimens might be attributed to the reduction of volume fraction of precipitates due to dissolution.

The intensity of Taylor {4 4 11} <11 11 8> component increased with increasing the ARB cycles in the ST-ARB and Aged-ARB specimens. It was considered that in the UFG structure, the grain boundary strongly constrained the deformation of grain interior, leading to reduction of local shear deformation and consequently the development of Taylor {4 4 11} <11 11 8>

component during ARB processing. However, the pre-existing Al_3Sc precipitates accelerated the grain refinement in the Aged-ARB specimens, leading to stronger Taylor {4 4 11} <11 11 8> component in the Aged-ARB specimens than in the ST-ARB specimen up to 7 cycles.

It was found that after annealing at 600°C, Cube {100} <001> texture strongly developed in the 400°C Aged-ARB specimen, whereas this Cube {100} <001> was not observed in the ST-ARB and 300°C Aged-ARB specimens. The difference in Cube {100} <001> texture between the 400°C Aged-ARB specimen and other specimens was probably due to the reservation of fine-grained structures, i.e., driving force for grain growth, at higher temperature in the 400°C Aged-ARB specimen.

Acknowledgments

The work presented in this thesis has been carried out Department of Materials Science and Engineering, Kyoto University, Japan. I would like to express my deepest respect and gratitude to my supervisor **Prof. N. Tsuji** for providing me the expert guidance, insight, vision, patience and tremendous help with the presented research. I would like to thank and acknowledge **Prof. S. Ochiai** and **Prof. I. Tanaka**, for accepting to evaluate my thesis. I would like to thank deeply **Dr. A. Shibata** for the most inspiring discussions throughout the revising the manuscript. Many thanks are for his valuable suggestions and also for his patience and excellent advices. I would like to thank **Dr. D. Terada** for his help during my experimental work. I also thank my friends in Prof. Tsuji`s laboratory for their time and help.

My deepest gratitude is offered to the Ministry of Science of Iran for their support of my living and study costs during my stay in Japan.

Publications :

(1) E. Borhani, H. Jafarian, H. Adachi, D. Terada and N. Tsuji, ″**Annealing behaviour of Solution Treated and Aged Al-0.2wt% Sc Deformed by ARB**", *Materials Science Forum, 2011, Vol. 667-669, pp. 211-216. doi:10.4028/www.scientific.net/MSF.667-669.211*

(2) E. Borhani, H.R. Jafarian, D. Terada, H. Adachi and N. Tsuji, ″ **Microstructural Evolution during ARB process of Al-0.2mass%Sc alloy Containing Al_3Sc Precipitates in Starting Structures**", *Materials Transactions, Vol. 53, No. 1 (2012), in press.*

(3) E. Borhani, H. R. Jafarian, T. Sato, D. Terada, Y. Miyajima and N. Tsuji, ″ **Effect of pre-aging on microstructure and mechanical property of Al-0.2wt%Sc deformed by ARB** ″, *Proceeding of 12th International Conference on Aluminium Alloys (ICAA 12),September 2010, Yokohama, Japan, p.2168-2173.*

Presentation in Japanese meeting :

(1) E. Borhani, H. R. Jafarian, H. Adachi, D. Terada, and N. Tsuji, ″ **Change in microstructure and mechanical properties of Pre-Aged Al-0.2wt% Sc deformed by ARB**″, *Proceeding of meeting of the Japan Institute of Metals, 2010 autumn*, Hokkaido University, p.539.

(2) E. Borhani, H. R. Jafarian, D. Terada, Y. Miyajima and N. Tsuji, ″**Effect of Pre-aging on microstructure and mechanical properties of Al-0.2wt% Sc deformed by ARB**″, *Proceeding of meeting the Japan Institute of Metals, 2009 autumn*, Kyoto University, p. 525.